Solar Radiative Transfer into the Ocean:

A Study on Underwater Light Fluctuations due to Surface Waves

Dissertation

zur Erlangung des Doktorgrades

der Mathematisch-Naturwissenschaftlichen Fakultät

der Christian-Albrechts-Universität zu Kiel

vorgelegt von

Dipl.-Ing.

Martin Hieronymi

Kiel, 2011

Referent:	Prof. Dr. Andreas Macke
Korreferent:	Prof. Dr. Oliver Zielinski
Tag der mündlichen Prüfung:	13. Mai 2011
Zum Druck genehmigt:	13. Mai 2011
gez.	Prof. Dr. Lutz Kipp, Dekan

Für Janine

Abstract

The thesis is about the solar radiative transfer into the ocean. Particular emphasis is placed on underwater light fluctuations due to focusing surface waves. The study includes measurements at high sea and computational simulations of the light propagation in seawater and wave-induced radiative variability.

Surface waves of different sizes have an optical lensing effect; they cause focusing of light beams at various depths. The underwater propagation of light depends on the scattering and absorption properties of seawater. Strongest light fluctuations appear near the surface at water depths of 0.5 to 10 m. At 1 m depth, radiative enhancements with a factor of 40 compared to the mean light level can be achieved. These short-term extreme values refer to the downwelling irradiance. The reason for the most intense irradiance peaks are surface waves with lengths of 20 cm to 5 m. In theory, light flashes with a radiative intensification of the factor 1.5 can appear down to 80 m of water depth. The range of possible irradiance peaks is discussed with respect to all relevant ocean waves. Even 200 m long swell waves can originate small irradiance changes below the 90 m depth level.

In natural sea states waves of different sizes are superposed. Their respective lensing effect controls the subsurface light regime. The mechanisms of those interactions are analyzed. Local wind, which is primarily associated with ultra-gravity waves, strongly affects light fluctuations within the near-surface region down to 10 m depth. The most intense radiative peaks result from moderate wind conditions with velocities of 2 to 7 m s^{-1}. Below 10 m depth, the temporal and spatial light variability is driven by superposed fully developed gravity waves of the corresponding sea state. Comparable strong variations arise from 1.5 m high waves. Even in 100 m depth slight wave-induced light field variance was found.

Zusammenfassung

In dieser Arbeit geht es um die Sonneneinstrahlung in den Ozean und insbesondere um Schwankungen des Strahlungsangebots aufgrund von fokussierenden Wellen auf der Wasseroberfläche. Die Untersuchungen umfassen sowohl Messungen auf See, als auch Computer-Simulationen der Unterwasser-Lichtausbreitung und der wellenbedingten Strahlungsvariabilität.

Verschieden große Wellen wirken als optische Linsen und verursachen damit eine Bündelung von Sonnenstrahlen in unterschiedlichen Tiefen. Die Ausbreitung des Lichts hängt maßgeblich von den Streu- und Absorptionseigenschaften des Wassers ab. Die stärksten Lichtschwankungen treten in Wassertiefen von etwa 0,5 bis 10 m auf und können das Strahlungsniveau in der Tiefe um mehr als das 40-fache übersteigen. Solche kurzzeitigen Extremwerte, bezogen auf die abwärts-gerichtete Strahlungsflussdichte, werden durch Wellen von 20 cm bis 5 m Länge hervorgerufen. Theoretisch können Lichtblitze mit einer 1,5-fachen Strahlungserhöhung in bis zu 80 m Wassertiefe auftreten. Die Bandbreite der möglichen Strahlungserhöhungen ist für alle relevanten Wellen im Ozean erörtert; sogar 200 m lange Dünungswellen können das Lichtangebot in größeren Tiefen (> 90 m) beeinflussen.

In einem natürlichen Seegang sind Wellen verschiedener Größe überlagert, die durch ihre jeweilige Linsenwirkung das Unterwasserlichtregime beeinflussen. Die Mechanismen der gegenseitigen Verstärkungen und Abschwächungen von Strahlungswerten werden genau analysiert. Der momentane Wind über einem Seegebiet und die damit verbundenen kleineren Ultra-Schwerewellen haben bis etwa 10 m Tiefe starken Einfluss auf die Unterwasser-Lichtfluktuationen. Die größten Schwankungen treten bei mäßigen Windverhältnissen von 2 bis 7 m s^{-1} auf. Unterhalb von 10 m werden die Fluktuationen zeitlich und räumlich von überlagerten voll ausgereiften Schwerewellen des entsprechenden Seegangs bestimmt. Die stärksten Lichtschwankungen werden hier von etwa 1,5 m hohen Wellen hervorgerufen. Noch in 100 m Wassertiefe können leichte seegangsbedingte Strahlungsschwankungen nachgewiesen werden.

Contents

Preface

The thesis begins with an overview about light in the ocean. Chapter 2 deals with offshore measurements of underwater irradiance and spatial light fluctuations. Then, computational simulations of the solar radiative transfer into the ocean follow. The spatial underwater light propagation and attenuation is explained in Chapter 3. The most important findings of this work are discussed within Chapter 4. Therein the influence of different wave types onto the subsurface irradiance distribution is highlighted. Additionally, the inter-dependency of different waves that are superposed at a realistic sea surface is considered. The findings raise various new questions, e.g. about the significance of the development of the sea state on the near-surface light regime. Related hypotheses are posed in the outlook Chapter 5.

The present thesis contains sections that are already published. Chapter 2 essentially includes text passages from:

Hieronymi, M., and A. **Macke** (2010): Spatiotemporal underwater light field fluctuations in the open ocean*, JEOS:RP*, 5, 10019s, 1-8, doi: 10.2971/jeos.2010.10019s.

Additional data from later research cruises are included into the graphs. The complete data set underlines the key statements made in the article.

1 Introduction

1.1 Light in the ocean

The optical oceanography researches questions concerning solar radiation in the sea, because many marine processes are light-related. Classical questions center on the radiative transfer into the ocean, aspects of the ocean color, underwater visibility and photography, properties of sea water, polarization of radiant energy, and of cause its impact on marine processes. These various aspects are introduced in standard works of the ocean optics such as *Jerlov* [1968], *Preisendorfer* [1976], *Jerlov and Steemann Nielsen* [1974], *Dera* [1992], *Shifrin* [1988], and *Mobley* [1994].

The theory of radiative transfer is of central significance to the study of optical oceanography. Methods for measuring and predicting the behavior of parameters in the ocean are derived from this theory. The basic concept of radiative transfer into the ocean is well known [e.g. Mobley, 1994]. The underwater light field, which is generally meant to be the downwelling irradiance distribution, depends on external factors as the surface illumination, i.e. the sun angle, the ratio of skylight to direct sunlight, and cloud conditions, and it depends on so called "inherent optical properties" (IOPs) of the sea water [*Gordon*, 1994]. These IOPs comprise the medium's properties for absorption, scattering, and total beam attenuation [*Preisendorfer*, 1976], and they are still subject to ongoing research [e.g. *Morel*, 2009]. Models for oceanic radiative transfer calculations are quite sophisticated; one of them is the software *Hydrolight* [*Mobley*, 1994] which is used for comparative studies in this thesis.

The solar radiative transfer in the ocean depends also on the wind-roughened water surface. On the one hand, the reflectance of radiation at the surface is influenced by the wind. More precisely, the irradiance reflectance decreases at stronger wind, especially at low sun positions [*Preisendorfer and Mobley*, 1985]. On the other hand, choppy water affects the total irradiance within the water column; it strongly diffuses the insolation. These aspects of wind-considerations are covered by common radiative transfer models [e.g. *Mobley et al.*, 1993].

Wind generates surface waves, and those have a lensing effect that causes enormous variability within the subsurface light field. This wind-wave-induced light variability cannot be represented by common radiative transfer models.

As a start, it is useful to address the geographical extension and the significance of wind and waves. Wind is caused by differences in atmospheric pressure. The air is accelerated from higher to lower pressure. Figure 1 shows a global wind climatology to illustrate the spatial and temporal variance and the scales of wind over the ocean. In terms of the radiation budget of the ocean the tropics and subtropics are most important [*Trenberth et al.*, 2009]. Within the tropics easterly winds dominate the flow pattern. Extreme strong winds are more common beyond the subtropical ridge (30° N to 30° S). Trade winds are temporally quite stable with moderate average wind speeds of 8 m s^{-1}.

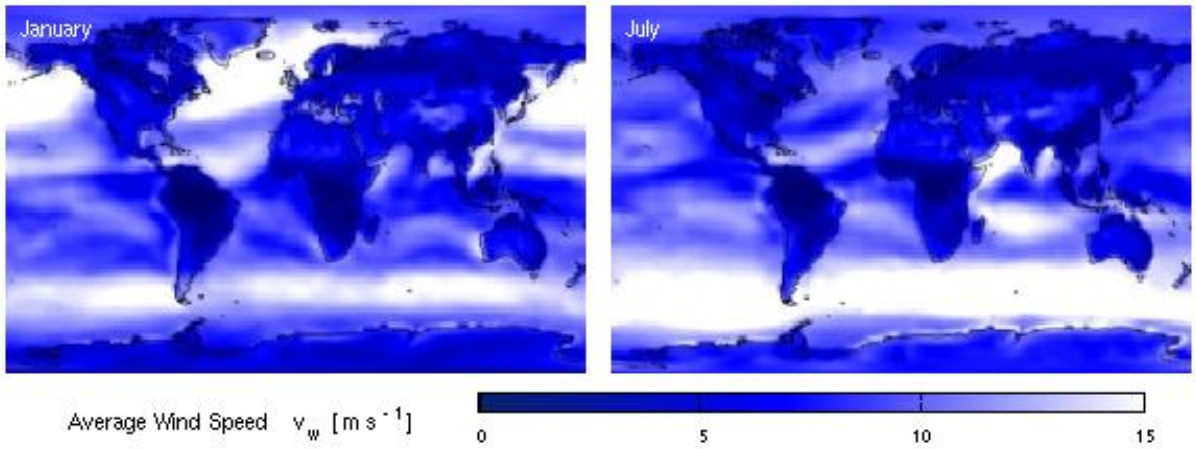

Figure 1. Global maps of the average wind speed v_w in January and July (the images are adapted from the NASA Earth Observatory web page[1]).

Sea state is the general condition of the free ocean surface. Thereby, we distinguish between wind sea and swell. Wind sea is an immediate response to local wind, that features comparatively steep waves with sharp crests and usually has a wide-band spectrum. Swell is the aftereffect of a previous wind field or it approaches from a distant widespread windstorm area. Those waves are generally more rounded with less steepness. Swell has a narrow-band spectrum [*Krauss and Meldau*, 1983]. As a rough rule of thumb, a period of 10 s is taken as separation from sea and swell, although wave systems with periods > 6 s are also referred to be swell [*Kinsman*, 1965].

The development of a sea state is determined by three factors: the strength of the wind, the duration, and the fetch (affected area). Sea states are characterized by the significant wave height H_s, which is the average wave height of the one-third largest waves, and by a mean wave period, e.g. the period between consecutive wave crests (peak period T_p) or the averaged time interval between two successive upcrossings of the mean water level (zero-upcrossing period T_0). Figure 2 shows the global occurrence of significant wave heights and zero-upcrossing periods. The climatology for January is from the web-based *KNMI/ERA-40* wave atlas [*Sterl and Caires*, 2005]. The climatology reveals the wide spreading of fully developed sea states and swell systems. From this follows that, concerning the underwater light field variability, both potentially influencing parameters, local wind and sea state, should be kept in mind.

[1] NASA Earth Observatory web page: http://earthobservatory.nasa.gov/IOTD/view.php?id=1824

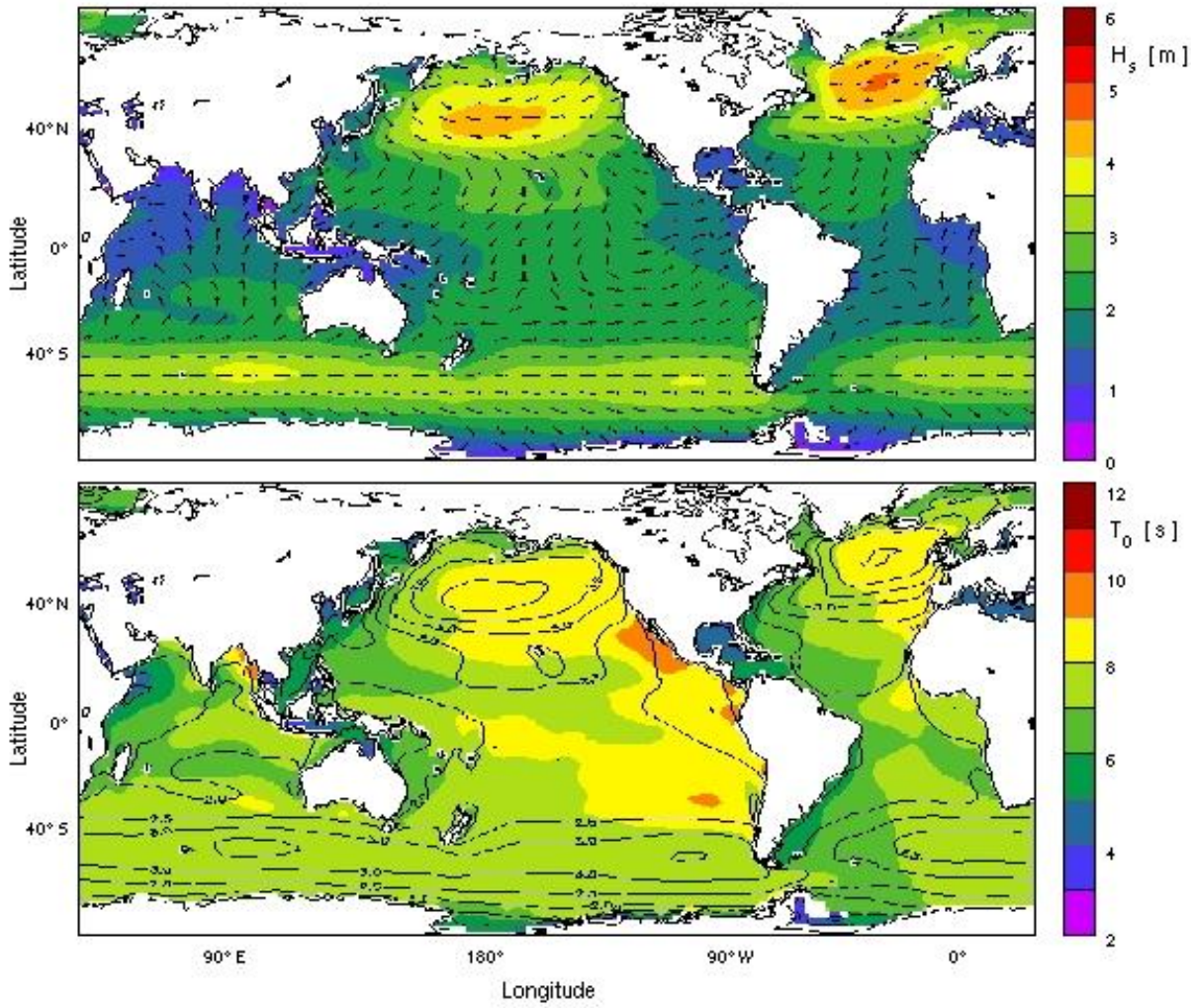

Figure 2. Climatology of the significant wave height H_S (top) with mean wave directions (arrows) and of the zero-up-crossing period T_0 (bottom) with H_S as contour lines; the surface plots show the monthly mean values for January as derived from ERA-40 ocean wave data (1971-2000); the graphs are adapted from the web-based KNMI/ERA-40 wave atlas[2] [*Sterl and Caires*, 2005].

The radiative transfer in water depends on the ocean color. Phytoplankton varies in size, form, orientation, depth, and optical properties. The composite of phytoplankton contributes to the color of seawater. In the oceanic radiative transfer theory, planktonic particles are quantified in terms of the chlorophyll-a content *Chl* of seawater in units [mg m^{-3}]. The global distribution of *Chl* is subject to some regional and seasonal variability (Figure 3). *Jerlov* [1968] classified water types with regard to its spectral irradiance transmittance. The water turbidity that is used in this work is widespread at high seas and it is referred to as clear oceanic water of Case 1 (with *Chl* = 0.03, 0.1, and 1 mg m^{-3}). Variations in ocean color, water classifications, and properties of the clearest natural water are discussed in detail by *Morel and Prieur* [1977], *Morel et al.* [2006] and *Morel et al.* [2007] respectively. *Wernand and van der Woerd* [2010] report of long-term North Pacific Ocean color changes; on multi-year time scales, the ocean color can vary significantly between blue and greenish-blue, e.g. the bluest ocean was encountered during 1990-1994, greenest values were found during the early 1950s.

[2] The KNMI/ERA-40 Wave Atlas web page: www.knmi.nl/waveatlas/

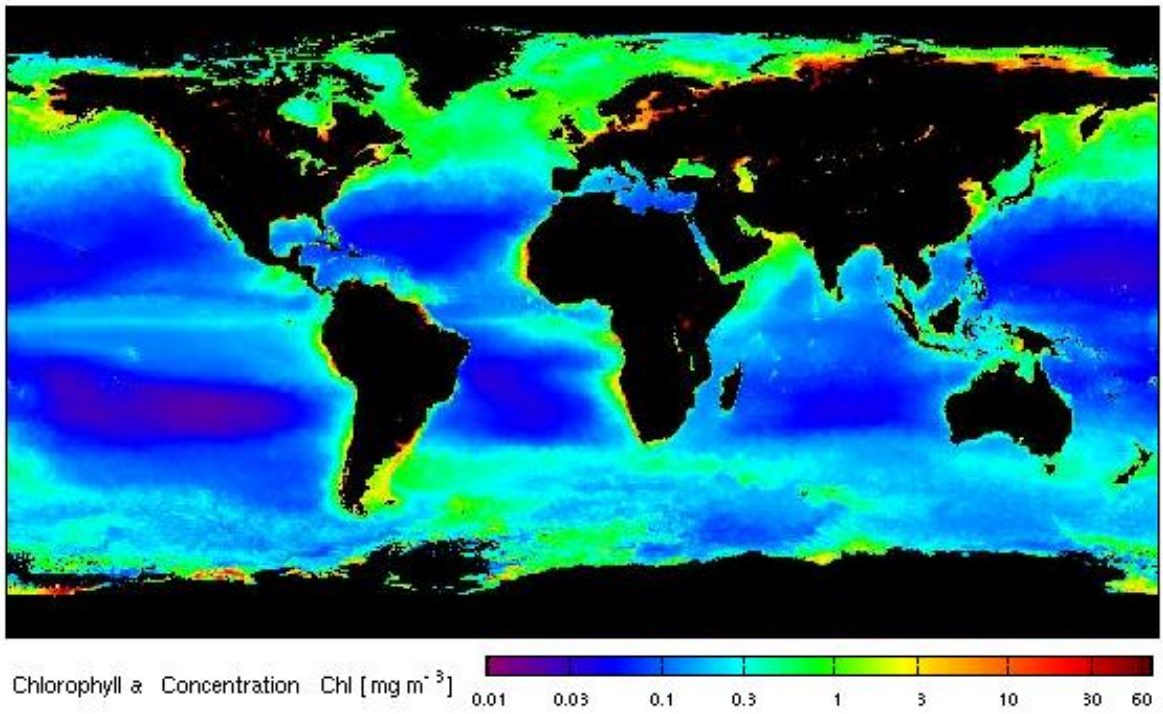

Figure 3. Global distribution of chlorophyll *Chl* averaged over the period from 01/01/2002 to 01/31/2008 using MODIS data from the Aqua satellite. The data are provided by NASA[3], and the map is adapted from the web page[4] of *Stewart* [2005].

In this respect, an interesting question is: Why is the ocean blue? *Dickey et al.* [2011] summarize the latest theories: In very clear water with few particles, the optical properties depend primarily on the scattering and absorption properties of the water molecule itself. There is very little absorption at blue wavelengths (at round 420 nm), but almost thousandfold more absorption in the red (at 730 nm). Absorption in the blue requires excitation of the vibration modes of the molecular water bonds to higher-lying states (vibration at high overtones of the fundamental vibrational mode). The density of such molecular states is low, and this is, why there is little absorption at blue wavelengths. Thus, the indigo blue water color is due primarily to molecular vibrations and not to direct electron interactions, which are the primary determinants of color in almost all other substances.

1.2 Ecological significance of the solar radiative input in the ocean

Solar radiation drives important physical, chemical, and biological processes in the ocean. Light is the fuel for the heat engine that drives the ocean's currents and the atmosphere's circulation [*Dickey et al.*, 2011]. Photosynthesis by marine phytoplankton produces roughly half of the oxygen in our air [e.g. *Johnsen and Sosik*, 2004]. Marine predators use light to hunt; prey use light to camouflage. A choice of topics that are

[3] NASA ocean color web page: http://oceancolor.gsfc.nasa.gov/
[4] R. Stewart, Department of Oceanography, Texas A&M University, Online Textbook: http://oceanworld.tamu.edu/resources/oceanography-book/phytoplanktondistribution.htm

related to the impact of solar radiation on the marine environment (with overview literature) is:

- Primary production [*Jerlov and Steemann Nielsen*, 1974; *Longhurst et al.*, 1995],
- Photosynthesis [*Long et al.*, 1994; *Wozniak et al.*, 2003],
- Photochemistry [*Zafiriou et al.*, 1984],
- Upper-ocean thermodynamics [*Fedorov and Ginsburg*, 1992; *Ohlmann et al.*, 1996],
- Remote sensing [*Dickey et al.*, 2006],
- Marine life [*Hanlon and Messenger*, 1996; *Wahl*, 2009].

Some of these topics and processes respond very fast on changing light conditions. That means that some processes in the marine environment immediately react on wave-induced high-frequency irradiance fluctuations. For example, *Greene and Gerard* [1990] showed that at high daily irradiance, growth rates (of red algae) were higher under fluctuating light than under constant light. Fluctuating light effects were frequency-dependent; growth was enhanced by fluctuations at 0.1 and 1 Hz, but not at 0.01 Hz. Their results also provided indirect evidence that high-frequency light fluctuations may enhance instantaneous photosynthetic rates, which could increase the daily carbon gain and this, in turn would stimulate growth of phytoplankton and algae. It is estimated that more than half of the primary production occurs in depths less than 40 m [*Siegel et al.*, 1995] where light availability can be subject to wave-induced fluctuations. Thus it is of interdisciplinary interest to better understand the variability of light in the ocean.

1.3 Objectives of the work

The aim of the dissertation is to quantify the range of light variability in the ocean that is caused by sea surface waves. By means of radiometric measurements and radiative transfer simulations, the following questions shall be addressed in this thesis:

- What maximum radiative enhancements can occur due to the wave lensing effect?
- What fluctuations appear at different depths? What time scales are relevant? What irradiance amplitudes occur?
- Which roles play single wave types, from very small capillary to fully developed swell waves, in terms of light field variability?
- How do individual light fields interact under realistic sea surfaces?

2 Measurements at sea

2.1 Data collection

2.1.1 Measurement locations

Measurements have been carried out on board the Research Vessel *Polarstern* during four north-south traverses of the tropical and subtropical Atlantic Ocean (measurement locations are marked in Figure 4 and cruise details are given in Table 1). The reported measurements are carried out within the framework of the *Oceanet* project. Therein, the energy and material exchange between ocean and atmosphere is subject to research. Detailed datasets on atmospheric conditions (e.g. of clouds, radiation budget, aerosols) and marine properties (e.g. inherent optical properties of water, biomass concentrations and composition) are recorded.

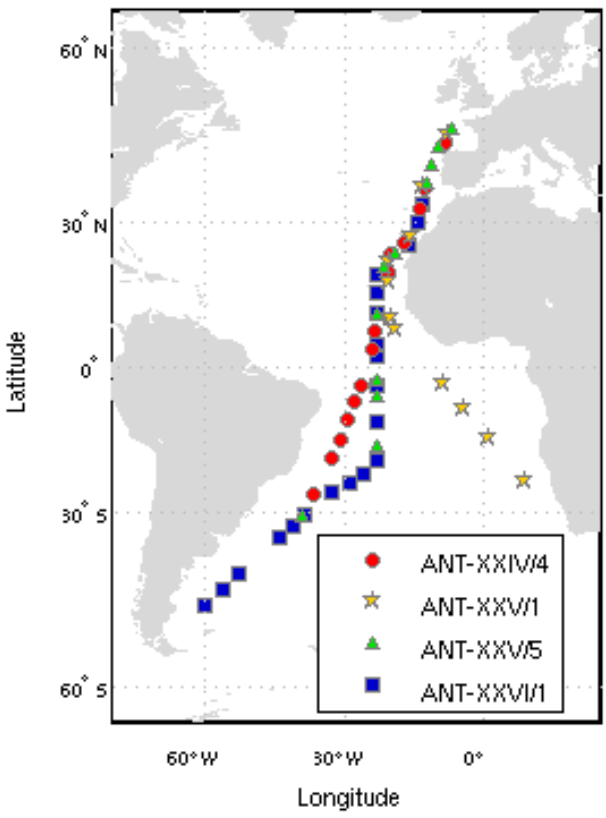

Figure 4. Measurement sites on board the Research Vessel *Polarstern* at the Atlantic Ocean.

Table 1. Details of the cruises with the Research Vessel *Polarstern*.

Year	Period	Cruise	Track	Reference
2008	04/18 – 05/20	*ANT-XXIV/4*	Punta Arenas – Bremerhaven	*Macke* [2009]
2008	10/31 – 12/03	*ANT-XXV/1*	Bremerhaven – Cape Town	*Kattner and Koch* [2009]
2009	04/11 – 05/24	*ANT-XXV/5*	Punta Arenas – Bremerhaven	*Zenk and El Naggar* [2010]
2009	10/16 – 11/25	*ANT-XXVI/1*	Bremerhaven – Punta Arenas	*El Naggar and Macke* [2010]

Light fluctuations in the upper ocean are investigated under conditions that afford strong light variability, like direct sun, high sun altitude and not too choppy seas. These requirements limit the number of missions. Since the vessel is moving, some aspects need to be kept in mind, which may influence the results. The light attenuation depends on water composition, which was not the same at different stations – the water was sometimes turbid tropical-subtropical water and often extremely pure ocean water, but always so called case 1 water [*Morel and Prieur,* 1977]. Additionally phytoplankton and thus scattering particles were not distributed homogeneously within the water column. With changing ship positions the maximum sun altitudes change as well. Our measurements were carried out at zenith angles always lower 40°. However, according to *Gernez and Antoine* [2009] the fluctuation parameters should be around the same order of magnitude at these zenith angles.

2.1.2 Registration of the sea state

The registrations of the sea states are accomplished by on-board meteorologists via visual assessment and additionally by means of a wave radar system (only at the *ANT-XXV/5* cruise [*Zenk and El Naggar,* 2010]). The sea state parameters are distinguished for swell and wind-sea, for each the significant wave height H_s (which is defined as the mean wave height of the one-third highest waves), the mean peak period T_p, and the corresponding directions of propagation. Wind speed and direction are registered automatically.

The overall significant wave heights at the measurement sites were between 1 and 3.5 m, and the mean wave periods were normally in a range of 6 to 9 s. That corresponds in general to moderate through rough sea state characteristics. Our observations are in accordance with the wave climatology for the relevant sea areas and seasons [*Sterl and Caires,* 2005]. In terms of the relative ratio of energy associated to each wave system [*Rodriguez and Guedes Soares,* 2001], we had mainly swell dominant sea states (50 of 57 times). Only three times wind-sea dominated sea states occurred. Four cases with comparable influence of wind-sea and swell were observed. This is an interesting point since the appearance of swell waves may imply strong sea surface deflections despite of the absence of local wind.

2.2 Motion pictures of underwater light pattern

In order to support the interpretation of ship-based radiometric measurements we use an additional system to visualize spatiotemporal patterns of underwater light. This consists of movie shots allowing straightforward conclusions on surface waves that cause certain light fields. Image analysis facilitates indication for light fluctuation amplitudes (i.e. the strength of irradiance oscillations), ranges of temporal fluctuation periods, and spatial patterns respectively.

The system utilized consists of a commercial digital camera in an underwater housing which is mounted on a pyramidal frame with a white plate underfoot (technical specifications in Table 2). From above the camera films the horizontal projection screen on which light patterns are displayed. This platform with tilt and pressure sensors is suitable down to maximal 40 m of water depth – below 30 m depth fluctuations in brightness are hardly detectable. The construction is lowered from a zodiac boat manually to compensate partly enormous hydrodynamic forces pulling at the screen due to wave motions. Water depth is to be seen as water column above the plate – with significant wave heights up to 3.5 m it is not feasible to hold the device in constant depths relative to the zero level. Another important advantage of operating from a zodiac is that the measurements can be taken from the undisturbed wave fields and away from light shadowing by the ship. Motion pictures of 1 to 2 min length are taken at defined depths. The focus of the camera and the sensor's integration time are held constant during measurements.

Table 2. Specifications of the underwater camera device.

Camera	*Canon Power Shot A620*
- resolution	7.1 megapixels
- image size	480 x 640 pixels
- image frequency	30 fps
- memory card	2 GB
Underwater housing	*WP-DC 90*
- maximum depth	40 m
Projection screen	0.4 x 0.6 m

Limitations of the system can be for example: shadows by the camera and the frame onto the projection screen (which happens often), certain inclination of the plate (distorted compared to a perfectly horizontal projection), automatic adjustments of the camera cannot be avoided, and motions in general must be accepted. In principle, one can stabilize the construction at a particular depth – the up- and downward transit often is related with movements and horizontal displacements which can lead to slack-cable situations that contain the risk of damage or loss [e.g. described in *Hieronymi*, 2008]. A grid with 10 cm spacing at the white plate allows areal mapping of the light fields and features bench marks for camera focusing.

2.2.1 Methods and instrumentation

2.2.1.1 Image analysis

The first step of image analysis is to cut the film into single pictures and allocate them to the pertinent depths. Images are composed of red, green and blue pixel information (*RGB* value) which assign the spectral intensity. In the first meters of the water column pixel values of each color develop temporally similarly with high correlation. With increasing water depth the individual color fractions separate. Green and blue parts are still quite similar and highly correlated. The red information disappears because of stronger absorption in this spectral band. Below 10 m of water depth the images are noticeable bluish and greenish in more turbid water. Pixel analyses in the time and frequency domain are performed separately for each color portion. In the following the so called gray value G is used (values between 0 and 255). This value mirrors the pixel brightness independently of the spectral range. The colors are weighted by the spectral sensitivity of the human eye:

$$G = 0.299 \cdot Red + 0.587 \cdot Green + 0.114 \cdot Blue \quad (1)$$

2.2.1.2 Spatial light fields

The single pictures provide areal information on the grade of attenuation and the overlapping of clustered light beams. Within the first meters the major portion of visible light is not absorbed jet, which leads to potentially strong superposition due to the lensing effect. Depending on the electromagnetic wavelength, light is refracted at the air-water interface with different focal depths. For example, focal points of bluish light emerge deeper than red light at a given lens profile. And because of stronger absorption in the reddish frequency band, blue light develops more extreme intensity when focusing. Thus, a horizontal plane contains different development levels of color-depending focal planes.

Small scale structures of the mirrored water surface can be identified at pictures taken from 1 m of water depth (Figure 5). The images show the gray value pattern at different wind conditions, under calm conditions with a wind speed of v_w = 2 m s^{-1}, and at relatively strong wind of 11 m s^{-1} (strong breeze). The left picture shows much stronger brightness enhancements due to the focusing effect. Here, the structure of the light pattern is well-pronounced and the horizontal structure of the water surface above is traceable straightforwardly. This is different at strong wind. The light field is more blurred; radiative enhancements are less intense and appear more punctual on smaller contiguous areas. We cannot deduce the surface shape directly from the photograph. The information about the vertical surface deflection is not available from the two-dimensional projection of the three-dimensional surface.

The distance between two local intensity maxima at a line gives an estimate about the wavelength of the causing surface waves. Smallest recognizable distances correspond to approx. 1 cm long capillary waves, whose dynamics are dominated by the effects of surface tension. The most intense brightness variations in 1 m depth result from 20 to 35 cm long waves, which are small gravity waves. Figure 5 left shows no projection of capillary waves at all, since there is no noticeable wind, the pattern is predominantly governed by 10 to 20 cm long waves.

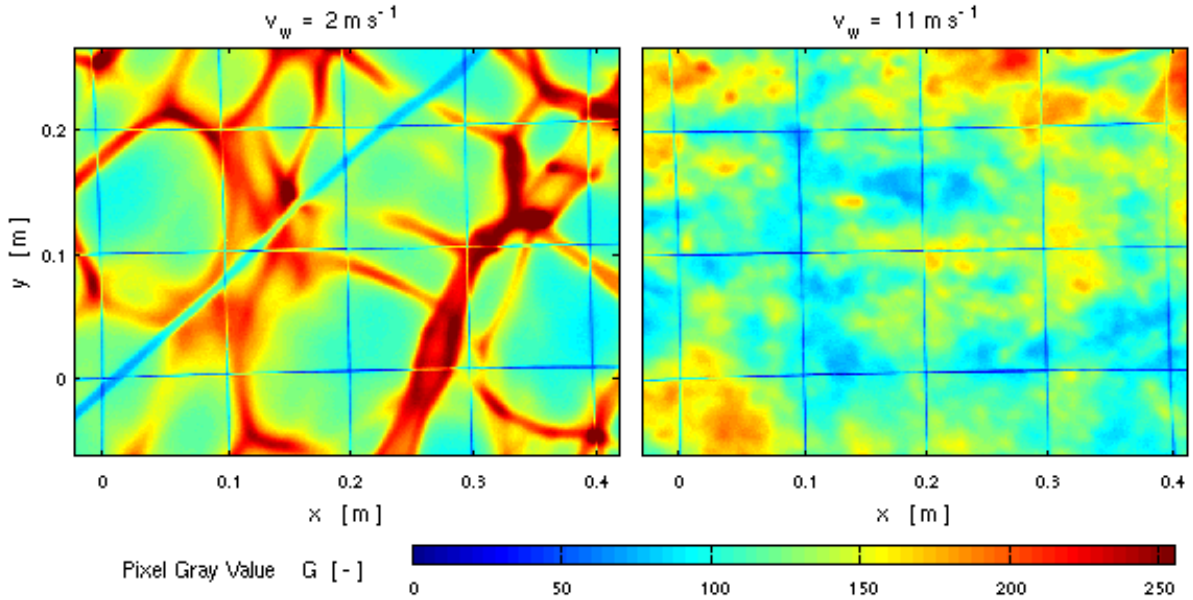

Figure 5. Snapshots of typical spatial light patterns at 1 m water depth; left: at very low wind speed of v_w = 2 m s^{-1} (10/28/2009), right: at relatively high wind speed of 11 m s^{-1} (10/30/2009). The color-coding indicates the pixel gray value *G*, the grid shows 10 cm distances. Shades of the frame and the camera may occur (e.g. left).

With increasing water depth the size of spatial light flecks grows. Light beams cluster together due to superposed larger surface waves. In addition, single light beams diffuse within the water body which handicaps the development of distinct focal points. At 5 m water depth typically smallest distinguishable structures are around 10 cm in distance. The patterns are dominated by intensity peaks of more than 25 cm space. The images show almost uniform brightness over the entire projection screen at depths of more than 20 m. Small changes of the pixel gray values become apparent from the chronology of the images only.

2.2.1.3 Time domain analysis

Figure 6 shows typical 20 s film sequences of the gray value along a 45 cm long image cut at water depths *z* of 1, 3, and 7 m. At the measurement site wind of 10 m s^{-1} was recorded. In the beginning very small light structures abound enlarging and smearing with depth. The most intense brightness peaks can often be observed at medium depths of 2 to 5 m (especially at high wind speed). In the example picture, the highest gray value is actually at 3 m depth. But obviously near the surface at 1 m intense peaks occur much more often which has an influence on the general variability of light.

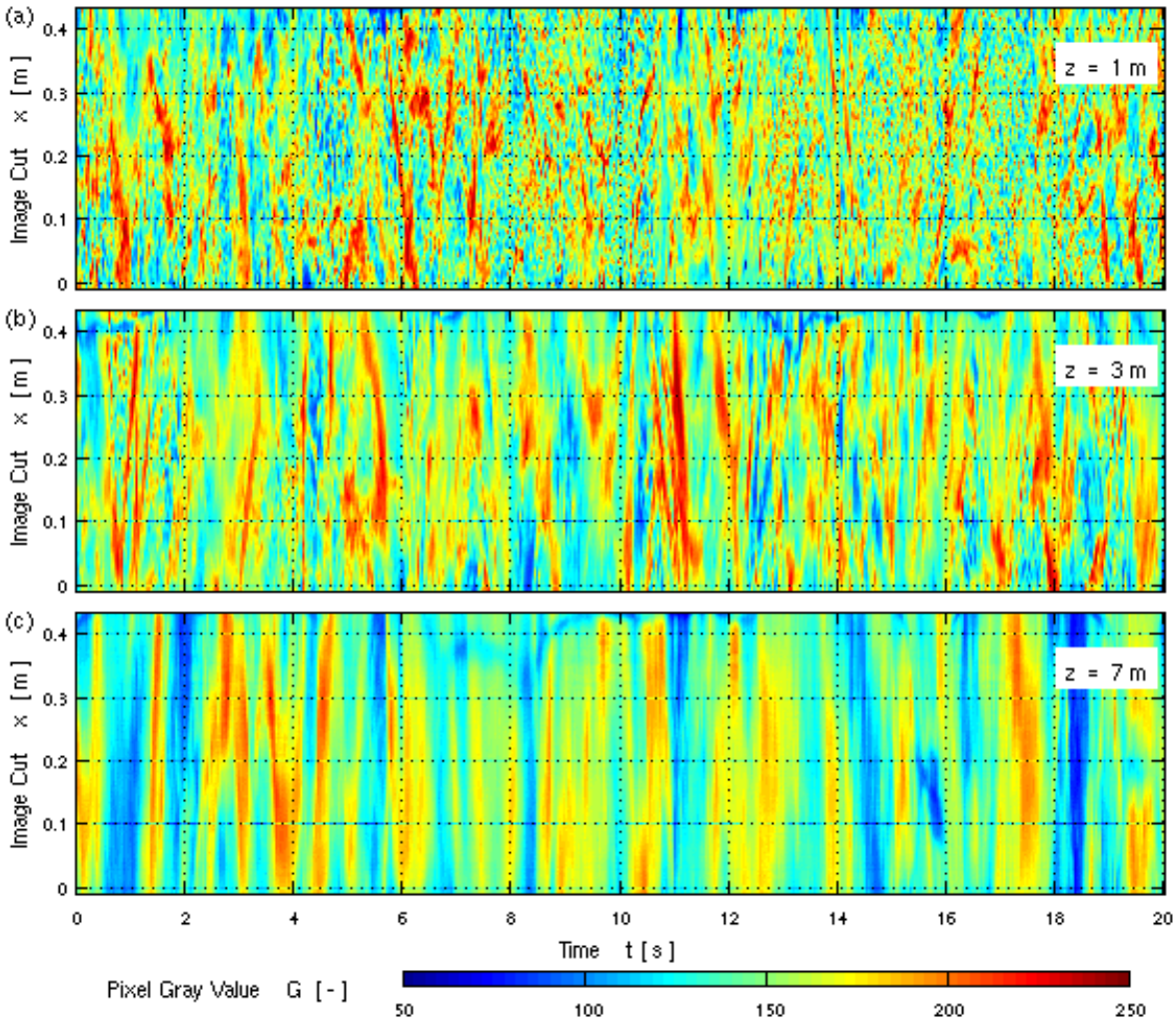

Figure 6. Spatiotemporal light fields at three water depths: (a) 1 m, (b) 3 m, and (c) 7 m. The ordinate shows a spatial cross section of the images and the x-axis shows the temporal change of the corresponding pixel gray values. The data are from 05/10/2008.

For time series analysis, image pixels are considered that are not subject to frame shadows or other disturbances like air bubbles only. Each time series has a length of 1 or 2 min with 30 frames per second resolution. One parameter used to characterize light intensity fluctuations is the coefficient of variation *CV* which is according to *Gernez and Antoine* [2009] computed as:

$$CV = 100\,\frac{\sigma_m}{\mu_m}, \qquad (2)$$

where μ_m is the median of the time series and σ_m is the standard deviation relative to the median. Figure 7 shows two time series of an image pixel taken at 1 and 15 m depth. The corresponding coefficients of variations are marked.

Note that the statistics of the image pixel intensity fluctuations cannot be related directly to that of the downwelling irradiance. Especially in the upper meters time series of irradiance typically show extreme enhancements, so called light flashes [*Dera and Stramski,* 1986]. Thus, the irradiance distribution is skewed. Compared to this, the distributions of pixel brightness are more *Gaussian* (not skewed). Extreme peaks are

bounded above by the upper limit of *RGB* values (the maximum [255 255 255] *RGB* color combination is a white pixel). A second reason for not recording extreme light flashes (and thus normal distribution of light intensity) is the camera's sensitivity and internal image processing. Nevertheless, for all intents and purposes the coefficient of variation can be qualitatively related to fluctuation amplitudes. *CV* is of around the same magnitude comparing the gray level with the irradiance at a depth.

2.2.1.4 Frequency domain analysis

The frequency band or a mean period respectively is the second parameter to specify light fluctuations. The temporal change of a pixel's brightness is evaluated by means of its spectral density (also variance spectrum). Based on fast Fourier transform (*FFT*) the frequency content of the signal is estimated. In Figure 7 typical variance spectra of corresponding time signals are shown. The maximum of the frequency weighted spectrum indicates the averaged peak period T_p of the signal, which often can be seen directly as a major superposed oscillation in the time signal. In the shown examples the dominant period is around 1 s at 1 m depth, and approx. 3 s at 15 m. This parameter is not always suitable and can lead to inaccuracy especially at wide spectral maxima or in case of peaks in close neighborhood. That problem can be faced by applying spectral moments:

$$m_i = \int_0^\infty f^i \, S\,(f)\, df \;, \tag{3}$$

where *f* is the frequency and *S (f)* is the spectral density of the signal. The mean period of fluctuation T_m indicates the spectral center of gravity, and thus more comprises the relevant frequency band:

$$T_m = \frac{m_0}{m_1}, \tag{4}$$

the area below the integral divided by the first moment. The mean period can be seen as grade of light field smearing. Normally, the mean period T_m is smaller than T_p and differences increase with depth. Both parameters are adequate to specify the signal's fluctuation.

FFT based spatial wavenumber analysis is inapplicable due to the limited size of the image plane (ca. 0.35 x 0.45 m). Instead of using the brightness time series of a single pixel, only one-dimensional image cuts of 45 cm length can be used. With dominant light patterns with spatial distances of more than 23 cm between intensity maxima, this approach lacks accuracy. Thus, the wavelength as a descriptive fluctuation parameter is less reasonable, for the given experimental setup.

For gravity waves spatial information can be gained indirectly out of dispersion relation of the surface wave period T and the wavelength L. In linear wave theory the wavelength (for deep water) is:

$$L = \frac{g}{2\pi} T^2 , \qquad (5)$$

where g denotes the acceleration of gravity. In this context the wavelength L describes the distance between two peaks (or local maxima) of light intensity.

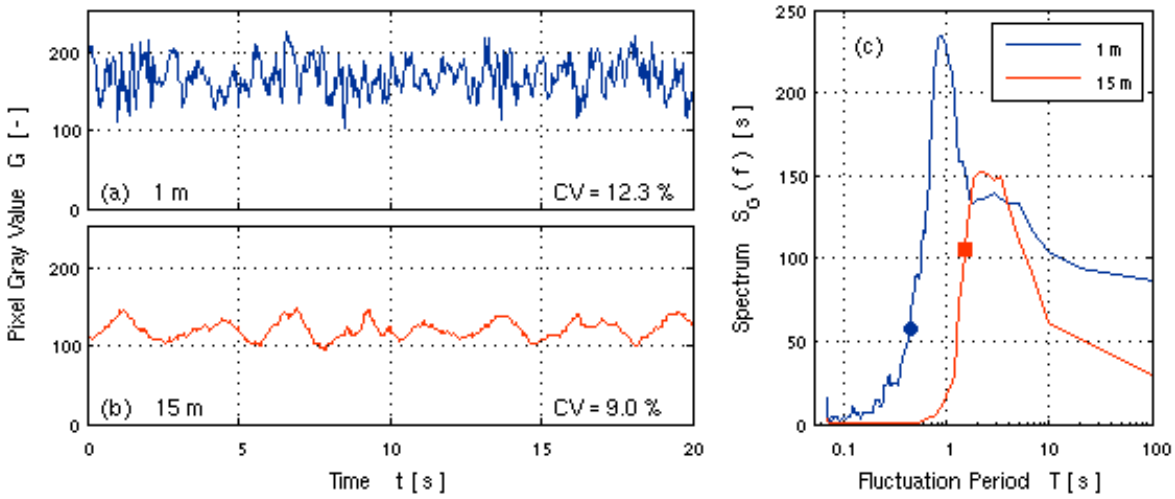

Figure 7. Left: typical time series of a pixel gray value G at (a) 1 m, and (b) 15 m depth; right: corresponding frequency spectra S_G of the same time series with marks of the mean fluctuation periods T_m (05/10/2008).

The spatiotemporal smearing of light field structures with increasing water depth is more obvious in Figure 8. Here, characteristic correlations between single pixel time series are plotted against the areal distance between both pixels. The mean values and the according standard deviations are shown for depths of 1, 7, and 20 m. While in the upper meters the correlation decreases fast after some millimeters of pixel distance, correlation is higher at larger depth. In 20 m depth, the whole picture is more or less of the same color that brightens and darkens slowly with time.

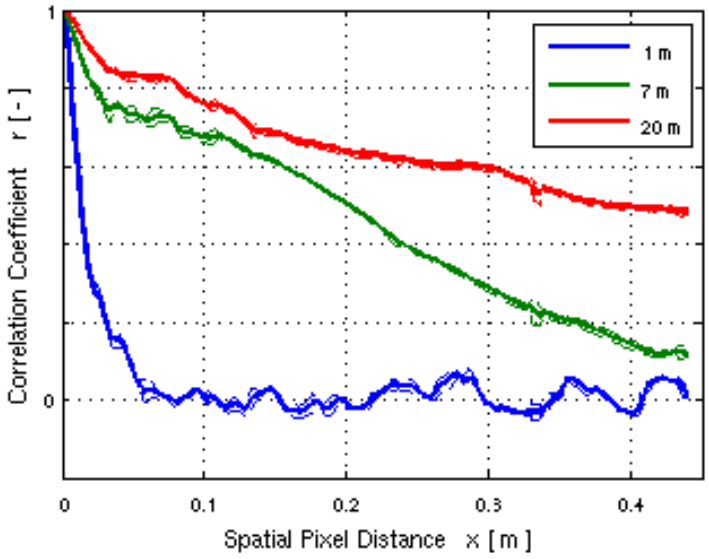

Figure 8. Typical correlation of the pixel gray value time series with respect to the distance of image pixels for three depths; solid lines represent the mean values and the dashed lines correspond to the standard deviation at the particular depth (05/10/2008).

2.2.2 Results of the motion picture analysis

The coefficient of variation CV and the mean fluctuation period T_m are used to describe the light fluctuations. These values can be related to environmental conditions as sea state parameters (periods and wave heights of both swell and wind sea), wind speed, water properties, sun altitude and water depth. Because of the limited number of data sets (57 measurement stations) just indications on those relationships can be given, e.g. effects due to different water properties or sun positions are not considered. In terms of underwater light fluctuations, the most important influencing parameters are wind speed and wave height [e.g. *Dera and Stramski*, 1986; *Gernez and Antoine*, 2009].

Figure 9 shows CV and T_m as function of classes of significant wave height H_s of the entire sea state. The colors stand for water depth down to 25 m. In general, CV decreases with water depth. The data suggest that CV, and thus the amplitud of fluctuations, is maximal at wave heights of 1.5 to 2 m for water depths below 3 m. Near the surface (< 3 m) less high waves seem to produce the most intense fluctuations. This is differently published by *Gernez and Antoine* [2009]; their irradiance measurements show maximum fluctuations due to waves of round 0.5 m height and reduced fluctuations at wave heights of > 1.5 m (measured at 3 m depth, relatively near the cost). We never had significant wave heights of less than 1 m during sampling; but the trend of our 3 m depth-data indicate maximum fluctuations in cases with 2 m wave height. However, the influence of the fully developed waves onto CV is shown.

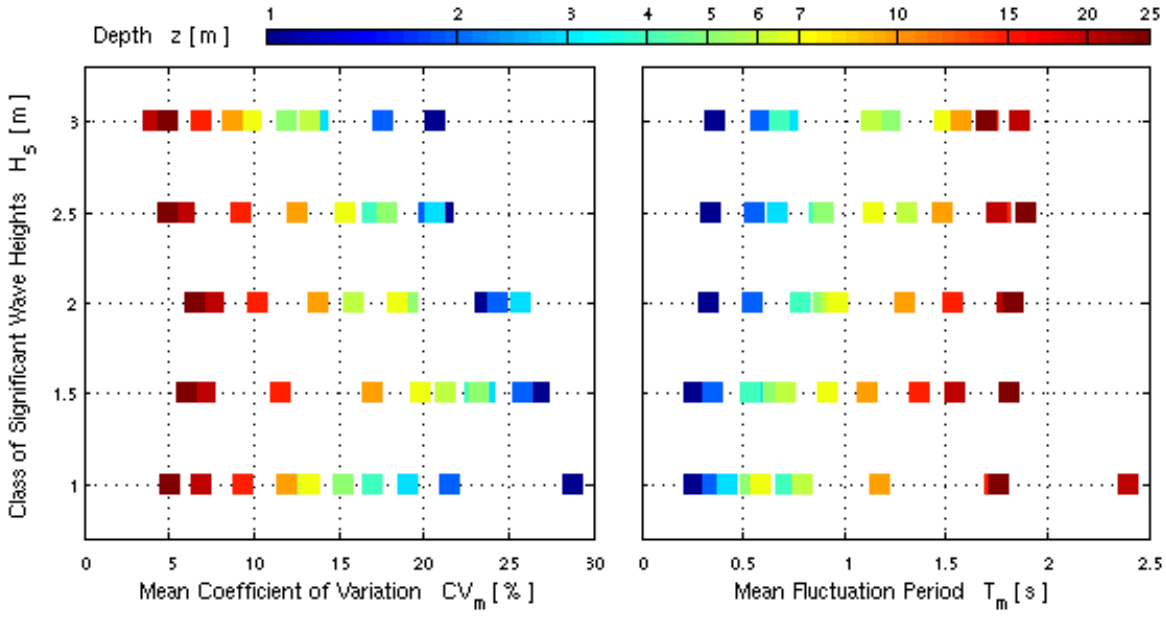

Figure 9. Summary of all motion picture data sets; left: the averaged coefficient of variations CV as a function of the order of magnitude of the significant wave heights H_s (within a ± 0.25 m range); right: the corresponding averaged mean fluctuation periods T_m. The colors show the employment depths z.

The mean fluctuation periods generally increase with increasing water depth. In relation to the wave height Figure 9 (right) shows trends for medium depths of 5 to 10 m only. With growing wave height, which is associated with longer waves and thus

extended wave periods, also the mean fluctuation periods of the light field increase. The data give evidence that surface waves of less than about 1.5 m length (or 1 s wave period in accordance to Eq. 5) do not play a decisive role for light fluctuations below 10 m depth; the mean fluctuation is obviously governed by developed gravity waves. For this reason we can state that local wind (with short fetch) has no influence on the light field below the upper 10 m layer. Light variability beneath is caused by larger waves of a more developed sea state (or longer wind fetch and dwell time respectively).

Wind and sea state cannot be treated separately. Wind generates waves. The size of waves depends on the length (fetch) of water and duration over which a given wind has blown. As shown before, swell systems often overlay local wind seas at the open ocean. Those aspects of inter-relation we have to keep in mind when analyzing the data.

Figure 10 shows *CV* and T_m of pixel gray values at different water depths and plotted versus wind speed. The color bar indicates H_s. In previous works mostly light regimes in two to four water depths are investigated, this study presents data from eleven depths and thus gives a more detailed vertical resolution. Every dot stands for the average value of 100 image pixels of one analyzed movie at a certain depth.

With regards to the *CV*, the strongest fluctuations appear at relative low wind speeds (< 6 m s^{-1}) within the first three meters, which is consistent with observations by *Dera and Stramski* [1986], or *Gernez and Antoine* [2009]. Higher wind speeds increase the mean square slope of the sea surface regardless of wind direction [*Cox and Munk*, 1954]. This impairs the efficiency of generating lens-surfaces for intense focusing; that is the *CV* decreases. Local winds provoke the development of small-size waves. Their impact on the light regimes in terms of the focusing effect is limited to the upper meters of the water column. From this perspective, *CV* seems to lose its wind dependency with increasing water depth. There is no clear trend below 5 m depth. At 20 m depth slightly larger fluctuations can be observed at stronger winds. Here, light fields disperse and depend more on large scale structures of the water surface shape, i.e. wave height.

With regard to T_m, the mean fluctuation periods increase with depth from high-frequency dominance below 2 Hz (< 0.5 s) to slow varying of up to 3 s which comes along with dominant and clear peak periods of up to 6 s. The data show a tendency towards longer light fluctuation periods when the wind speed grows. This is equivalent to rising waves with longer wave periods. Below 10 m, mean and peak periods signify distances (wavelengths) of light intensity maxima of 2 m to 40 m. This gives evidence of gravity wave and sea state impact on underwater light regime. Even swell waves with periods of 5 to 10 s (40 to 150 m wavelength respectively) provoke potentially significant fluctuations of light intensity in deeper waters.

As an aside, some few data have been collected at overcast sky. Differences compared to clear sky can be observed down to 5 m depth. *CV* is generally smaller, whereas the temporal component is significantly decelerated; T_m values are noticeably higher. This point is further discussed in Section 4.2.1.

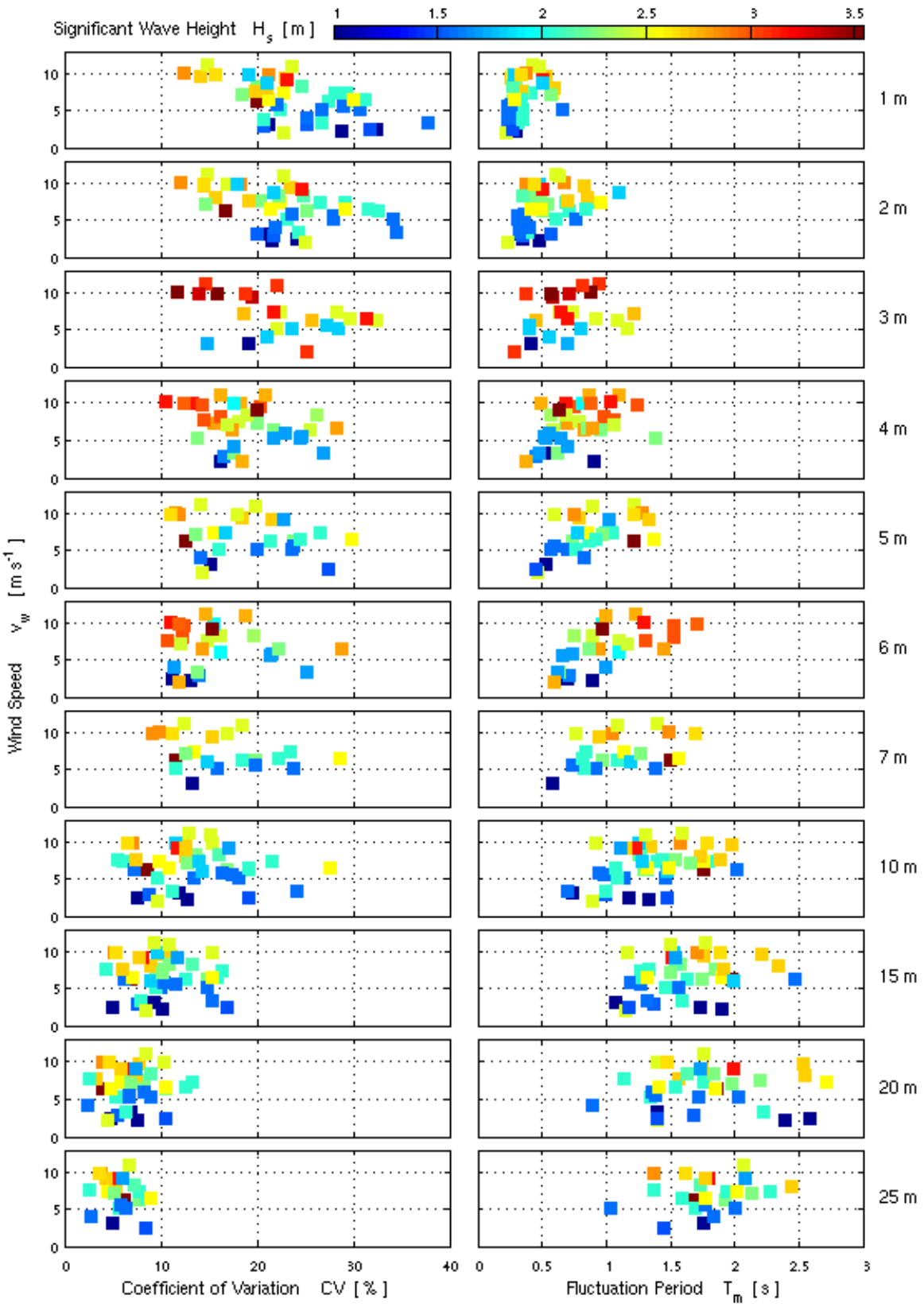

Figure 10. Summary of all motion picture data sets; left: coefficient of variations *CV* against wind speed; right: the corresponding mean fluctuation periods T_m. The water depths are marked top down to 25 m. The colors indicate the significant wave height H_s.

2.3 Spectral irradiance measurements

In order to characterize the underwater light regime, radiometers are lowered from the working deck of the vessel over a crane arm. The vessel is orientated (according the sun's position and wave direction) in a way that minimizes influences of the ship's hull on radiation and wave fields. Still the shadow of the hull compromises the quality and the representability of the radiometric datasets [e.g. *Smith,* 1974]. This drawback and the draft of the employed vessel *Polarstern* of about 11 m should be kept in mind when interpreting the results. Other possible effects on the dataset result from ship motions that are transmitted to the tethered sensors. At a specific measurement depth, the displayed depth varies by up to 0.5 m due to these motions. Declinations of the radiometer are recorded but disregarded for the data analysis since the tilt angles are comparably small.

The sensor employed is a *RAMSES-ACC-VIS*[5]. It maps downwelling irradiance E_d in the *UV* and visible spectral range (320 to 950 nm). Integration times for scanning the spectrum elongate with water depth, ranging typically in the upper 50 m of the water column from 8 to 512 ms but nevertheless, the sampling interval is around 2 s. This sampling rate clearly is insufficient to capture high-frequency light flashes and even longer fluctuation periods cannot be registered adequately. The mean value of E_d can be better estimated when sampling over longer times at particular depths. The sensor package is lowered to certain depths with step sizes of 2, 2.5 and 5 m down to a maximum depth of 50 m. At each depth, the sensor measures for 2 min. With sixteen stops, a complete mission can last for 50 min with environmental conditions assumed to be steady.

Figure 11 illustrates exemplary results of our radiometric measurements at high sea without any clouds at the sky. The upper picture shows the theoretically downwelling irradiance as it is measured at the top of atmosphere (*TOA*). The data originate from the *Solar Radiation and Climate Experiment* [*SORCE,* 2002]. The red line shows our measurement of the spectral E_d at sea level. Within the atmosphere solar radiation is partly absorbed (mainly by water vapor) and attenuated due to scattering at air molecules and aerosols. A major part of the radiation of the visible range reaches the sea surface; the corresponding spectral colors are marked at the top. The actual total radiation budget of the oceans (and the global mean) is reviewed by Trenberth et al. [2009]. Figure 11 (a), (b), and (c) show measured underwater E_d spectra at depths of 2, 10, and 20 m. By collecting 2 min data per depth level (about 80 spectra), we obtain a broader view of the light supply and variance in the water column. The mean spectra are plotted in red, minimum and maximum are denoted by the gray-shaded area to show wavelength-depending ranges of fluctuations. Most intensity is associated with wavelengths λ between 400 and 575 nm (blue and green range). At every depth the peak of the irradiance spectra is at wavelengths around 480 nm. Near the surface (a), waves cause irradiance maxima that partly exceed the actual insolation at the top of

[5] TriOS Optical Sensors: www.trios.de

atmosphere (wavelength depending). Very often our measurements show so called light flashes in the top layer. That means maximum $E_d(\lambda)$ values exceed the mean irradiance level by a factor of more than 1.5 [*Dera and Stramski*, 1986]. We measured light flashes down to 21 m depth (at 490 nm in very clear water). The penetration depth of light strongly depends on the spectral range. In 20 m depth, radiation in the red band is absorbed almost fully, whereas still 50 % of bluish light can be detected. The wavelength 490 nm is highlighted in the figure; that particular wavelength is of special interest in the modeling section of this work.

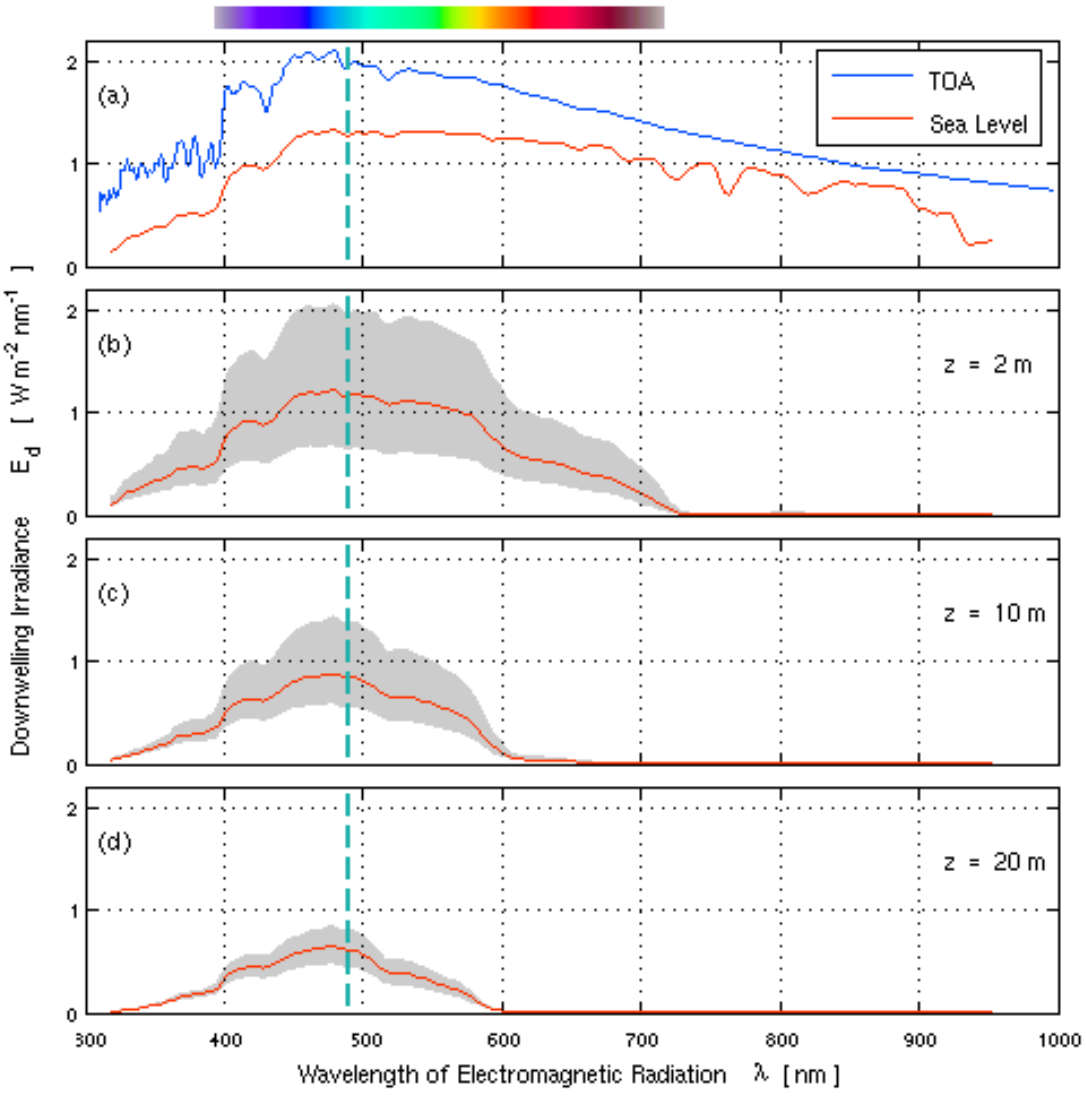

Figure 11. Measured spectral downwelling irradiances E_d: (a) theoretical insolation at the top of the atmosphere[6] (TOA) and measurements of the actual spectral irradiance just above the sea surface, (b) measured underwater spectra at 2 m depth, (c) at 10 m, and (d) at 20 m water depth. The red lines show the mean values at the particular depths, the gray shaded area indicates the range of fluctuations (minimum and maximum). The dashed line is at a wavelength of 490 nm. The color-bar at the top stands for the corresponding visible colors. Within the blue spectral range light flashes (50 % radiative enhancement) appeared down to 15 m depth at that day (10/30/2009).

[6] Data from the Solar Radiation and Climate Experiment SORCE web page: http://lasp.colorado.edu/source/index.htm

The following Figure 12 shows E_d depth profiles (of the same day) for the selected wavelength 490 nm and for the integrated range of photosynthetically active radiation (*PAR*). Commonly PAR is designated to the wave band of 400 to 700 nm, that marine phytoplankton is able to use for photosynthesis. This spectral range is almost identical with the range of light visible for the human eye. The crosses in Figure 12 mark the measured data relative to the surface downwelling insolation of 100 %. The squares indicate the averaged values within a horizontal layer of ± 0.3 m depth (that is due to hydrodynamic motions). The data illustrate the enormous variability of light in the upper ocean layer. With higher sampling rates, even more extreme radiative peaks can be detected. For example, *Gernez et al.* [2011] measured light pulses exceeding 10 times the average irradiance near the surface. Our low frequent data do not include such extreme radiative enhancements, but they prove that even below the 10 m surface layer strong wave-induced light variability does exists.

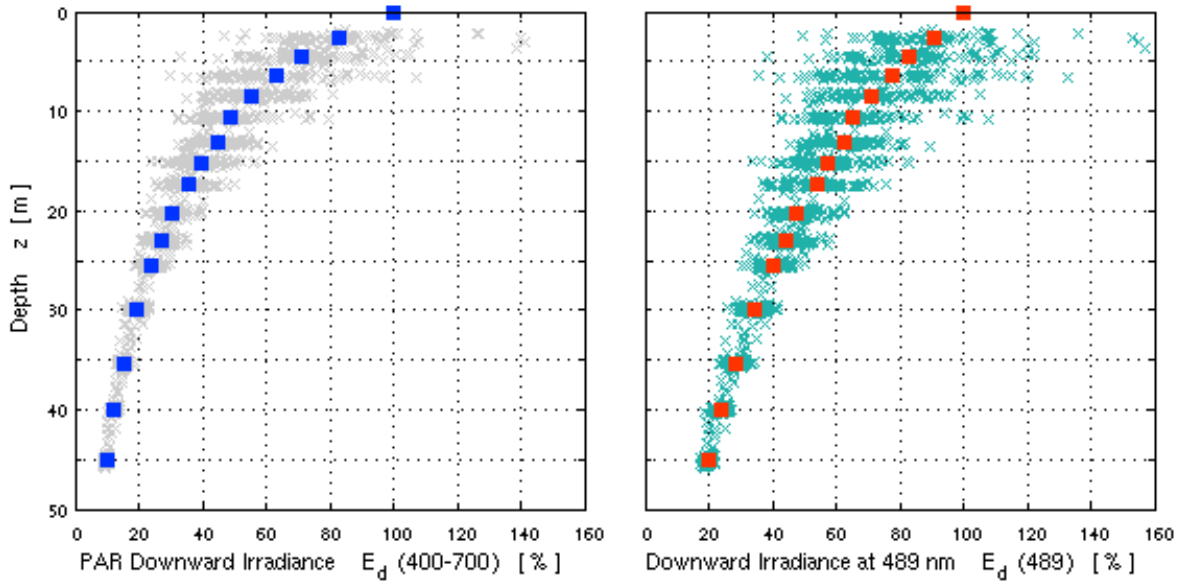

Figure 12. Measured downwelling irradiance E_d as a function of water depth, left: spectrally integrated over the range of photosynthetically active radiation (PAR) of 400 to 700 nm, right: downward irradiance at the single wavelength of 489 nm. The square signs show the averaged irradiance value per water depth. The data are normalized to 100 % surface insolation. Data of 10/30/2009.

The averaged E_d values characteristically decrease exponentially within non-stratified waters. The total attenuation coefficient for downwelling irradiance $K_d(\lambda)$ can be obtained out of these mean values [e.g. *Morel et al.*, 2007]. The coefficient is calculated (from just beneath the surface 0^- to a certain depth z) as

$$K_d(\lambda) = \frac{1}{z} \ln\left(\frac{E_d(\lambda,0^-)}{E_d(\lambda,z)}\right). \qquad (6)$$

The (spectral) diffuse attenuation coefficient is mainly governed by the absorption coefficient a, which adds up the absorption properties of sea water, particles, and dissolved colored matter (yellow substance); but K_d also strictly depends on the particle (chlorophyll) content of the water [*Morel*, 2009].

2.4 Conclusions of the field campaign

Measurements of spectral downwelling irradiance in the upper 50 m of the water column are presented and interpreted with respect to the focusing effect. These data are used for comparisons with results of underwater radiative transfer simulations (Section 4.2.3). The most important result from the offshore irradiance measurements is that wave-induced irradiance peaks of more than 1.5 times of the mean level irradiance (so called light flashes) were observed down to depths of more than 20 m. This applies to spectral wavelengths of the blue-green range. The fact that light flashes occur below 5 m water depth shows the significance of fully developed ocean waves onto the light variability.

Furthermore, an off-the-shelf underwater camera mounted on a projection plate is deployed for spatiotemporal light field visualization. With this, characteristic fluctuation parameters can be determined which help to interpret radiometric measurements. In addition, hints can be gained on corresponding surface waves that cause these light fluctuations.

The analysis of underwater motion pictures shows that small gravity and capillary waves cause high-frequency (> 1 Hz) intensity fluctuations with focal depths in relative shallow water (roughly above 5 m). In the first meter light fields are well pronounced. They show mirroring of capillary waves patterns with lengths as small as 1 cm. The most intense brightness variation results from 20 to 35 cm long surface structures, which matches small gravity waves. Within the top 5 m, the speed of wind is correlated to light fluctuation amplitudes in terms of *CV*. Relative slow winds (v_w of 2 to 7 m s^{-1}) cause strongest fluctuations and *CV* tends to decrease with increasing wind speed (which is a confirmation of previous works, see for example *Gernez and Antoine* [2009]).

With depth, light fields smear because of scattering and overlaying of diverse lensing systems. The light regime between 3 and 25 m of water column is affected by large scale surface structures. Significant wave heights of around 1.5 m provoke the strongest intensity oscillations and the speed of wind is only indirectly correlated with fully developed wind sea. When swells or premature wind seas dominate the sea state, which is often the case with high seas, the wind speed is no suitable comparative parameter. Ordinary gravity waves specify the irradiance distribution in this section of water column. Mean periods of intensity fluctuations range up to 3 s, which corresponds to outstanding averaged peak periods of up to 6 s. Dispersion relation shows light filed structures of 2 m to 40 m wavelength below 10 m water depth. With depth, brightness oscillations are decelerated with smaller amplitudes (*CV*).

Even longer ocean waves with periods of 5 to 10 s (which is equivalent to wave lengths of 40 m to 150 m) have potential to provoke significant fluctuations of light intensity in deeper waters. This is of relevance for light availability in the major part of the euphotic zone and thus can be of interest for all photo-relevant processes.

3 Solar radiative transfer simulations

Sea water is a diffusing medium. Thus scattering processes play a major role concerning the transport of solar radiation into this medium. They lead to a spatial spreading of light beams. When modeling the focusing effect of surface waves, light beams and the entire spread pattern must be superposed with respect to a spatial allocation.

The Monte Carlo (MC) procedure is mostly the method of choice to simulate the radiative transfer in the earth's atmosphere and ocean when non-plane-parallel geometries are to be taken into account. The physical processes of scattering, absorption and surface reflection / transmission are simulated for a sufficiently large number of individual photons. Fundamental contributions to the subject have been published by *Plass and Kattawar* [1972], and *Gordon and Brown* [1973]. *Kirk* [1981] performed Monte Carlo calculations with emphasis on very turbid yellow water. Beginning with *Plass et al.* [1975] the rough water surface is considered and with it the substantial wave influence on reflectance and downward radiation fluxes. The wave system is described as a wind-depending stochastic wave slope distribution in accordance with *Cox and Munk* [1954]. Up to now this description of the rough air-sea interface is generally applied for example in the *Hydrolight* software by *Mobley* [1994] or in the *MOMO* code by *Fell and Fischer* [2001]. In *Mobley et al.* [1993] an inter-comparison of various numerical models for computing underwater light fields is assembled, in which the standard problem of a windblown air-water surface is addressed. It is shown, that these models provide reasonable mean values for underwater radiances and irradiances. However, the extreme variance of radiative fluxes near the surface cannot be simulated with randomly distributed wave slopes. For this task a well-defined wave structure is needed. This issue is addressed by implementing successive wave slopes of superposed elementary waves from a wave spectrum [e.g. *Nikolayev et al.*, 1972; *Weber*, 2010; *You et al.*, 2010]. Whereat *D'Alimonte et al.* [2010] showed a first *MC* model where the corresponding wave amplitude itself is additionally considered.

Concerning light field fluctuations in the upper ocean layer, two points pose particular challenges: One is the realistic description of the water surface and its implementation into the radiative transfer model and the other is the propagation of light within the water column with exact spatial allocation of direct and diffuse radiative parts. Both issues are addressed in this and in the following chapters. This chapter aims to investigate the detailed expansion and attenuation of light in natural waters by means

of a new approach with a two-dimensional Monte Carlo method. Light enters the water column in one point only; the diffuse up- and downward directed irradiance is than numerically modeled with fine spatial resolution, as a function of the light's angle of incidence and the inherent optical properties of the water body. Light fields with different incidence angles are then assembled within a data bank. The basic idea is to decouple time-consuming Monte Carlo simulations from the relatively fast geometric ray tracing for light fluctuation analysis. Once the light beam entered the water body with a specific transmission angle, its propagation is always similar. The follow-up chapter shall illustrate the geometric ray tracing by superimposing areal independent subsurface light fields caused by realistically shaped surface waves. The aim is to show the potential radiation enhancements and radiative variations along the water column due to the (de-) focusing effect of waves and to clarify the relevance of diverse wave types.

3.1 Underlying data

The present study considers monochromatic light at a wavelength of 490 nm where the water body is very transparent (see Figure 11). The inherent optical properties IOP of oceanic (so called case 1) waters at 490 nm are well documented. The corresponding scattering and absorption data that are implemented in the model are taken from *Morel* [2009]. Another advantage of using 490 nm is that Raman emissions only play a minor role [*Stavn*, 1993; *Morel et al.*, 2002] and can be neglected. Scattering is regarded as perfectly elastic and polarization effects are not considered too.

According to *Morel et al.* [2007] and *Morel* [2009] (and their references) the total absorption coefficient a is the sum (a_w + a_p + a_y) of the absorption coefficients by pure seawater, particles, and dissolved yellow matter respectively and is given (for 490 nm) by

$$a_w = 0.015 \quad [m^{-1}] \tag{7}$$

$$a_p = 0.034\ Chl^{0.62} \quad [m^{-1}] \tag{8}$$

$$a_y = 0.02\ Chl^{0.62} \quad [m^{-1}] \tag{9}$$

The total scattering coefficient b consists of the scattering coefficient of optically pure seawater (at 490 nm wavelength and 20°C) and the particle scattering coefficient (b_w + b_p). The second term can be deduced from the particle attenuation coefficient $c_p = a_p + b_p$

$$b_w = 0.003 \quad [m^{-1}] \tag{10}$$

$$c_p = 0.352\ Chl^{0.62} \quad [m^{-1}] \tag{11}$$

The global scattering phase function for oceanic waters that accounts for both particle and molecular (water) scattering is based on *Petzold*'s work from 1972 [*Petzold*, 1972].

Petzold's volume scattering function is widely cited. But especially for very clear (hyper-oligotrophic) water one has to look at it critically because in this case the molecular scattering dominates the scattering properties of the water body [*Petzold*, 1972; *Mobley*, 1994]. Nevertheless, light is preponderantly scattered into the forward direction (see Figure 13). For our purpose with main interest in forward scattered parts these data are adequate. The present work applies the formulation of *Morel et al.* [2002], obtained through

$$\beta_{p+w}(\psi) = \frac{b_p\,\beta_p(\psi) + b_w\,\beta_w(\psi)}{b_p + b_w}, \tag{12}$$

where

$$\beta_w(\psi) = \frac{3}{4\pi\,(3+p)}\left(1 + p\,cos^2(\psi)\right), \tag{13}$$

with p = 0.84. The scattering angle is denoted by ψ. The adapted particulate phase function $\beta_p(\psi)$, as it is utilized in the model, is taken from *Mobley et al.* [1993]. Both highly scattering and highly absorbing cases are considered for this phase function. The graph in Figure 13 left shows the utilized volume scattering phase function for three different chlorophyll concentrations, the clearest natural water [*Morel et al.*, 2007], more widespread clear water, and relative turbid ocean water (all case 1). The small image shows the phase functions for *Chl* = 0.03 and 1.0 mg m^{-3} with respect to logarithmic polar coordinates. Extreme clear water scatters more light back (180°).

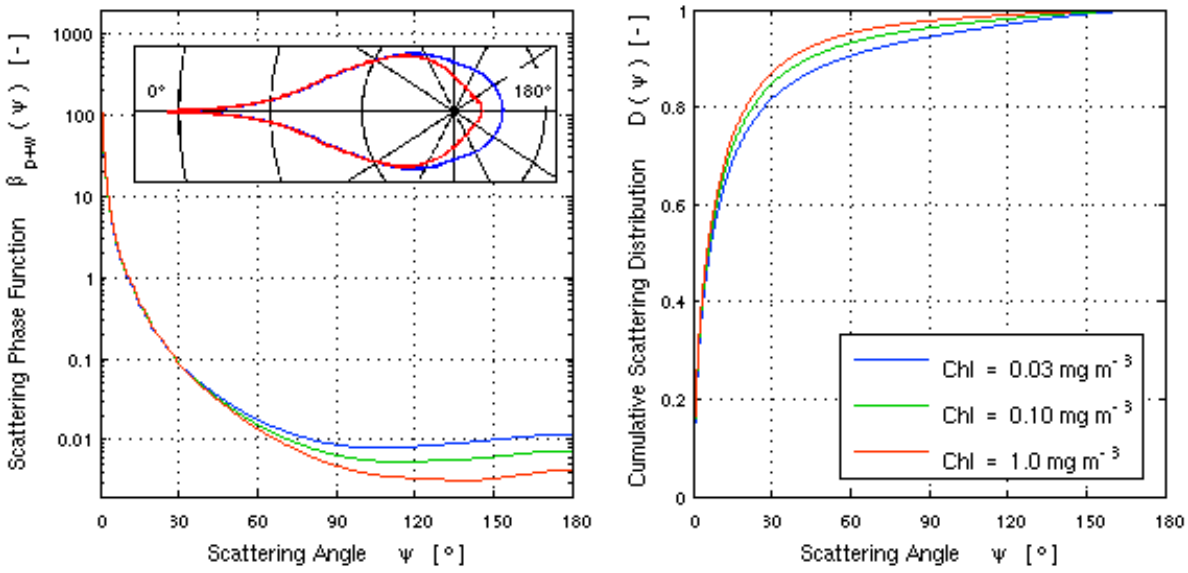

Figure 13. Scattering properties of sea water; left: scattering phase functions β_{p+w} for the three water types under consideration, right: the corresponding cumulative scattering distribution D. The small image within the left graph outlines the scattering phase function in logarithmic polar coordinates – scattering in forward direction (ψ = 0°) is most likely.

3.2 Description of the Monte Carlo model

The goal of the simulations is to determine spatial high-resolution underwater light fields with respect to surface waves. For ease, ocean surface waves are considered to be long-crested waves, they are nearly two-dimensional and the crests appear very long in comparison to the wavelength. Because of this fact and to save computational resources, we limit the radiative transfer into the ocean to a two-dimensional grid. The zenith angle corresponds to the direction of the water wave propagation; changes in azimuth are not required in 2D radiative transfer.

The model calculates the propagation of light inside the water body only. The light enters the 2D water column at one single point. The original subsurface direction of propagation corresponds to the transmission angle after *Snell*'s law, which in turn depends on the direction of the incoming light and the slope of the air-water boundary. The light intensity is normalized and always starts with 100 %. An intensity reduction due to reflection losses must be taken into account (*Fresnel*'s formulas) when adding the results for individual single ray simulations to a complete underwater light pattern.

As a first step, the inherent optical properties (IOPs) of the medium are assumed to be homogenous. The aim is to show the scattering effects under "laboratory" conditions and to allocate portions of direct and diffuse radiation under ideal conditions. In reality, IOPs of oceanic waters change along the vertical profile. Chlorophyll often peaks at a certain depth (see examples in Figure 39), where an optimal combination of light and nutrients exists.

The model grid covers 100 m water depth by 150 m width, with light beam access at one single point at the top. The mesh size is 0.1 m in both dimensions. This investigation treats a relatively large area of interest with comparatively low resolution; when it is used for wave-induced light fluctuation investigations (as in Chapter 4), less depth is required but with finer grid resolution (e.g. 0.005 m). Light can leave the system at all external grid boundaries, but never enter again. The model does not allow for periodic boundary conditions as this would violate the concept of the spatial irradiance pattern of a single beam. This is in contrast to other models where periodicity is intended, e.g. *D'Alimonte et al.* [2010]. The horizontal extension of the model domain has to be large enough to ensure that the horizontal losses due to domain leaving rays are negligible. The magnitude of these losses at the sides is discussed in Section 3.3.2.2.

The Monte Carlo procedure that we employ differs in some aspects from other models that are recently in use [e.g. *D'Alimonte et al.*, 2010; *You et al.*, 2010; *Deckert and Michael*, 2006]. For example, the ray tracing and the attenuation of light intensity are treated separately and independently. There is neither distinction between absorption and scattering as e.g. in *Kirk* [1981], nor a further identification whether the scattering process is caused by molecular or particle scattering [e.g. *Morel and Gentili*, 1991]. We do not apply the concept of "photon weight reduction", where the statistical losses by absorption and scattering are assessed by means of the singe scattering albedo $\omega_0 = b / c$

(at the scattering position: $w_{new} = w_{old}\,\omega_0$). With high grid cell resolution, i.e. with very short distances between the "detectors", this method must lead to a strong noise in the accumulated irradiance in each grid cell. In our model the (ray tracing) path length is determined by the scattering coefficient b only, and not by the attenuation coefficient c. This is compensated by a continuous light attenuation along the propagation path, which only depends on the total absorption coefficient a. Each horizontal grid segment in the area of interest is used as irradiance detector. With the given specifications of the grid this amounts to 1000 x 1500 detectors.

3.2.1 Ray tracing

The photon tracing starts at the point [0, 0] directly below the surface. The initial angle of all photons depends on the zenith angle of the sun and the slope of the small-sized wave segment and is determined by *Snell*'s law. With calm surface this transmission angle (with respect to the global coordinate system) can maximally be 48.6°. The largest possible tilt angle of a wave segment is about 30°, which gives a maximum transmission angle from air to water of approx. 70° in global coordinates (the effects of *Snell*'s law can be seen nicely in Figure 18). Therefore, the starting angle for the ray tracing is between 0° and 70° (downward directed). This parameter has to be modified with appropriate angle resolution (e.g. 0.05° steps) for the buildup of the database, which than provides as basis for wave focusing analysis.

The free path length l between two subsequent scattering events is determined by the selection of an equally distributed random number R between 0 and 1, and the total scattering coefficient b [*Macke*, 2000],

$$l = -\frac{1}{b}\,log(R)\,. \qquad (14)$$

The scattering properties of the medium consider molecular (water) and particulate scattering. In extremely clear sea water the mean free path length l_m (= 1 / b) is 25.54 m (with 0.03 mg m^{-3} particle content), while in more turbid sea water with Chl = 1 mg m^{-3}, l_m reduces to 3.12 m.

After passing the distance l, the light beam reaches a scattering point, where it changes its propagating direction according to the scattering phase function (Eq. 12), or the cumulative scattering distribution D, respectively

$$D(\psi) = 2\pi \int_0^{\psi} \beta_{p+w}(\psi)\, sin(\psi)\, d\psi, \qquad (15)$$

which again denotes a random number, equally distributed between 0 and 1 [*Morel and Gentili*, 1991]. The cumulative scattering distribution is a function of the degree of turbidity in terms of chlorophyll content (Figure 13). Fewer particles in a volume mean more weighting of molecular scattering and thus a higher probability for backscattering. Since the free path lengths are much shorter in turbid media, more scattering occurs and

in total, more photons are scattered upwardly (clearly to be seen in Figure 14). Note that although most light is scattered near the forward direction for all water types, after a sufficient number of ray paths (e.g. 200,000) radiation has captured all grid points in the entire area of interest (150 m x 100 m).

The ray tracing procedure considers a maximum number of scattering events, N_{max}. As long as the "photon package" does not leave the model domain, its way through the medium is traced up to this number. If the photon leaves the area, a new photon is selected. For example, at very low particle concentrations (0.03 mg m^{-3}) is N_{max} = 24. After travelling more than 600 m ($N_{max} \cdot l_m$) through the water body on average the "light beam" does not contribute a detectable intensity anymore (see Eq. 16). This approach is consistent with the "weight" threshold value of 10^{-6} which is often used [e.g. in *Plass and Kattawar*, 1972; *Mobley*, 1994; *Deckert and Michael*, 2006; *D'Alimonte et al.*, 2010].

At the water-to-air boundary partial and total reflection occurs. According to *Snell*'s law total internal reflection happens at nadir angles $\theta > 48°$ at 490 nm wavelength. In this case the photon remains in the system, otherwise a new photon is selected. Partial internal reflection is neglected, as it plays a minor role only [elaborately discussed in *Mobley*, 1994]. In this regard, the whole concept of superimposing individual single beam pattern contains uncertainties, which are critically discussed in Section 4.1.5. Each single beam pattern must be seen separately. The actual shape of the surface cannot be considered with respect to transmission and reflection rates. Individual light patterns do not interfere with each other.

The track of each single ray is followed in a way that every transition through a grid layer in vertical direction and within an *x*-segment is mapped with global coordinates (in the example shown the mesh size is $dz = dx = 0.1$ m). Thus, the total path passed by the photon package can be summed up and located exactly. In addition, it is possible to distinguish the direction of grid cell transition downward and upward respectively. Pure horizontal motions are traced as well, but their intensity values cannot be allocated to any *x*-segment at a defined depth.

3.2.2 Light attenuation

The actual attenuation of light occurs along its distance covered, on the grounds that the light beam transits toward a scattering point through an absorbing medium. In our model this approach is realized by a continuous intensity (or weight) reduction of the light beam, and this is characterized by the medium's absorption properties. At the scattering point no additional intensity reduction but only a randomly weighted change of the propagation direction takes place. With numerous changes of direction (within the whole model domain) the medium's scattering properties are approximately reproduced. The intensity attenuates exponentially along the covered path (similar to *Beer-Lambert*'s law)

$$I = I_0 \, exp(-a \, l_z), \tag{16}$$

with the initial weight or intensity I_0 of 100 % at point [0, 0], the total absorption coefficient a (including absorption by pure seawater, particles, and colored dissolved organic matter), and the total so far covered distance l_z with respect to the z-level.

The light's path is known with respect to global coordinates. Thus, the intensity values can be allocated and summed up for each x-segment at a z-level. Since the orientation of photon propagation is known, it can be stated whether its intensity contributes to down- or upwelling irradiances respectively. In the end, the accumulated weights for each grid cell are normalized by the total number of photons that have entered the system. The outputs of the model are areal distributions of normalized fractions of down- and upwardly directed irradiances with respect to a single-point light inlet and a certain in-water transmission angle. The adaptation of the normalized irradiance values regarding the relative light incidence angle (according to the *Fresnel* equations) must be taken into account when combining the single light pattern.

If we add all radiative fractions at a particular depth, we gain the total amount of diffuse (scattered) and direct (unscattered) irradiance at this depth. This value must be equal to the mean planar downward / upward irradiance (E_d and E_u respectively) at this particular depth for a flat water surface (this is true if the model domain is wide enough and thus all diffuse radiation is included).

3.3 Model results

The simulations provide the total radiant flux per area (or more precisely, per horizontal grid segment), which is the spectral radiant flux density or the spectral irradiance E (measured in W m^{-2} nm^{-1}). The irradiance is calculated with respect to a plane area for the downward and upward directed fractions. The summation of both parts gives the undirected irradiance, which for example could be of interest for the estimation of the total radiant energy supply of a horizontal layer of planktonic particles in the water. For this study, model runs have been carried out exemplarily with an initial zenith angle of 0° and with three different oceanic water types (each with invariant inherent optical properties over the whole water column). Furthermore, the light input due to diffuse sky radiation is illustrated.

3.3.1 Spatial distribution of down- and upward irradiance

Figure 14 shows the calculated downward (left) and upward (right) irradiance patterns for the three different water types. The color-scale is set logarithmic in order to better distinguish the spatial distribution. The E_u values are two orders of magnitude smaller than E_d (and therefore multiplied by the factor 100). At point [0, 0] the E_d values start with 100 %. The greenish tone of the color-scale labels the one-tenth of a percent

(1 ‰) range of the downwelling irradiance and 0.001 % for E_u. With perpendicular light incidence the E_d 1 ‰ region horizontally expands approx. ± 30 m in the clearest case and approx. ± 15 m at 1.0 mg m^{-3}. The scattering properties cause the typical oval to circular shapes of E_d distribution; more circular with increasing chlorophyll content, i.e. with more scattering. In all cases fractions of downward irradiance exist within the model domain. But it can be seen that the irradiance contributions per depth are vanishingly small beyond 50 m of horizontal displacement from the inlet (less than 0.01 %). Thus, a horizontal model domain width of 100 m should be sufficient.

On the right hand side of Figure 14 typical shapes of the E_u distributions can be seen. The "V" shape points out the more pronounced molecular backscatter and the lower scattering density in water with few particles (the upper both); here the E_u values are significantly higher compared with the "U" shaped distribution at high particle concentrations. In the bottom right subplot, the radius of the 0.01 % E_u contour line (orange color) is about 10 m, and the 0.0001 % radius expands to approximately 60 m (light blue). The results for the lateral boundaries and especially for the lower layer (below 80 m) must be taken with care, since here an insufficient number of photons passes the segments in upward direction to account for upwelling radiant fluxes. This is because all photons that left the model are not further considered and cannot re-enter again. However, below 80 m of water depth, E_u fractions are so small that their contribution to the energy budget can be neglected.

More and more irradiance is upwardly directed as the in-water transmission angle grows (not shown here). The shape of radiation spread in a specific water type does not change, but with respect to a planar global coordinate system, the ratio of down- to upwardly directed parts changes. This means in general, the lower the sun's position is, the more upward irradiance can be registered in the top layer. This is partly compensated by stronger reflection at the water surface and a reduced transmission rate in the context of the *Fresnel* equations. Enhanced upward directed irradiance near the surface is accompanied by enhanced water-leaving radiation, which in addition, increases with growing particle content. The most water leaving radiation originates from high incidence angles and large quantity of scattering particles (chlorophyll); this must be seen in relation to the incoming radiation.

Some statistical scattering features can be registered in the computer program, for example the number of photons which is reflected or which leaves the water-air boundary. In the case of a flat surface and very low chlorophyll, approx. 5 % of all traced rays (total radiation) are internally reflected at the surface with 0° subsurface light incidence, and 7.5 % at 48°. More than twice of these percentage values are observed at *Chl* = 1.0 mg m^{-3}. A comparison of the number of water-leaving and internally reflected photons shows, that always a bit more leaves the water body into the atmosphere instead of being in-water reflected and downwardly directed again.

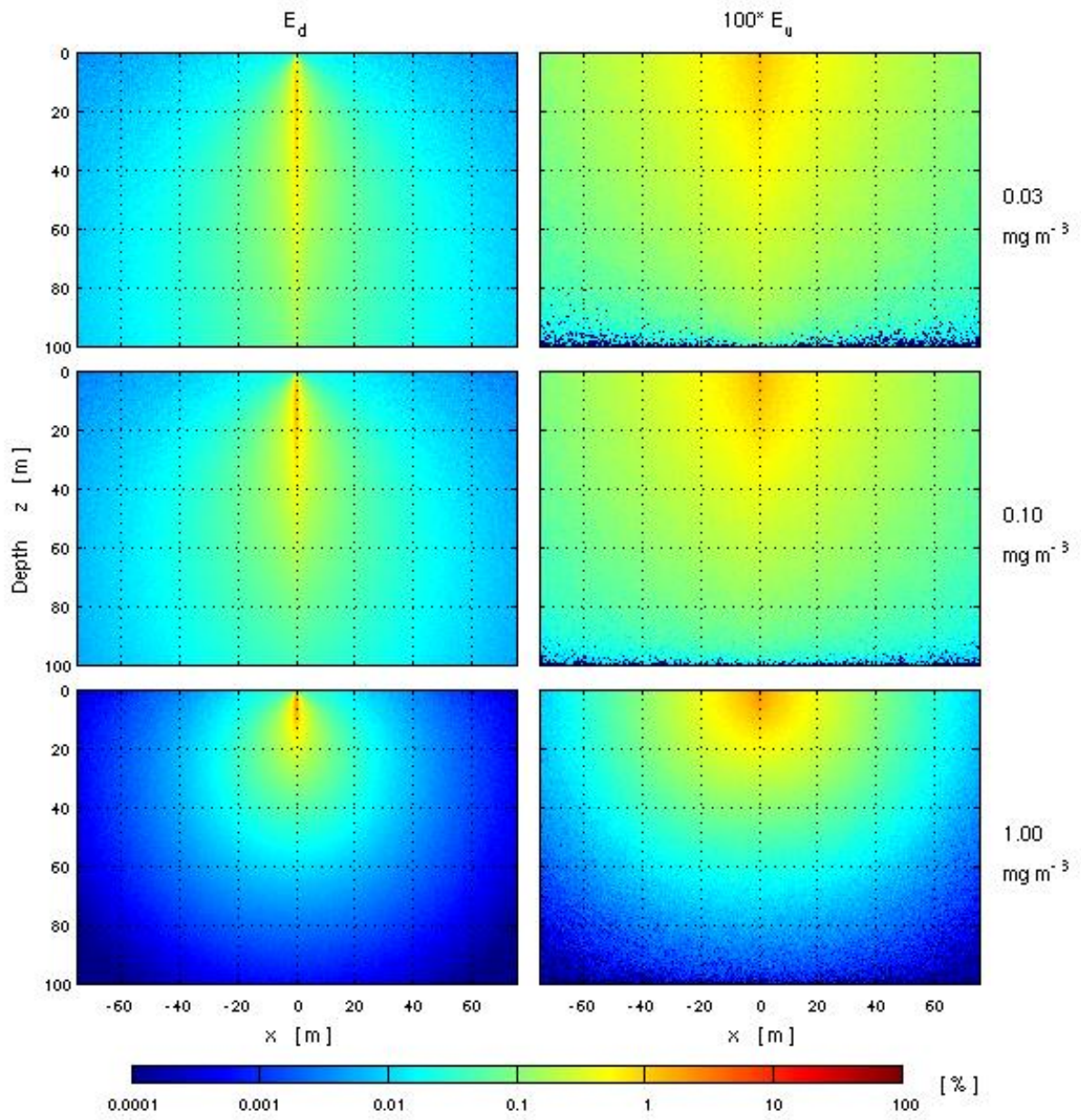

Figure 14. Spatial propagation of single light beams in different water types: allocation of downward irradiance E_d (left) and E_u (right) at perpendicular light incidence (note the logarithmic color scale and the factor of 100 for E_u).

3.3.2 Discussion of the model accuracy

3.3.2.1 Number of photons

The number of photons, which are necessary for a reliable irradiance picture, is a function of depth and horizontal distance to the photon entrance. Figure 15 shows the number of required photons for each grid point to achieve at least 95 % of the E_d value gained with one million ray tracings (0.03 mg m^{-3} particle concentration, 0° solar zenith angle). With the given grid properties, the pixel E_d values directly beneath the starting point (down to round 50 m) do not change anymore already after 10^3 photons. The original propagation path down to 100 m depth is saturated after about 10^4 runs. The

further away the detector is from the original propagation path, the more photons are required. With 10 m horizontal displacement around 200,000 photons are needed to reach the pre-defined statistical accuracy. Accurate patterns are realized much faster for the downward irradiance because of the strong dominance of the forward scattering. For the present study the model runs are carried out with $5 \cdot 10^5$ photons.

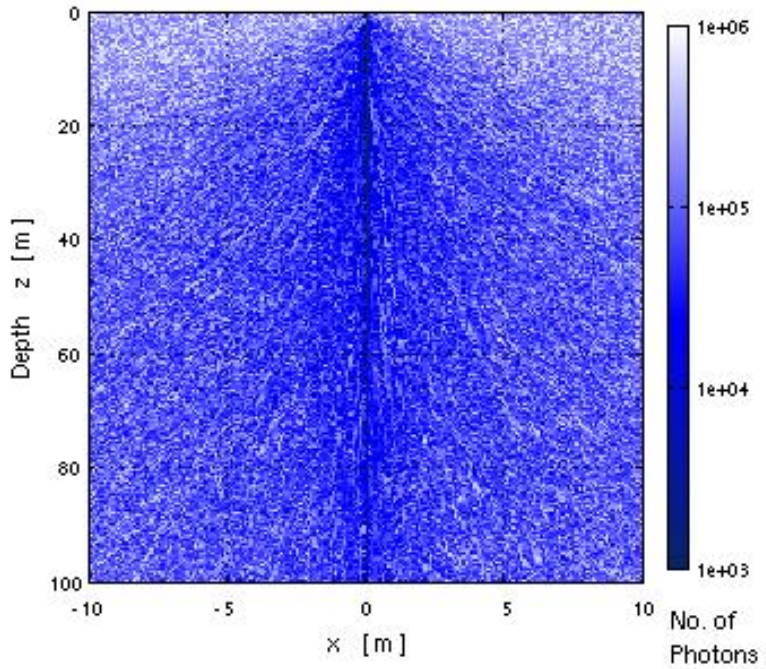

Figure 15. Number of photons needed to reach 95 % of the reference picture with 10^6 ray tracings with given grid properties, *Chl* = 0.03 mg m^{-3}, and ϑ_{tg} = 0 ° (note the logarithmic scale).

3.3.2.2 Size of the model domain

Obviously, the model domain width must be large enough so that the lateral outgoing radiation is negligible. If we consider a domain width of 150 m (i.e. 75 m distance from the inlet) and water with very few scattering particles (0.03 mg m^{-3}), linear approximation of the total losses of E_d on one side amount to 0.005 % directly beneath the surface and maximal 0.025 % in 80 m depth (with 1.0 mg m^{-3}: max. 0.0003 % at 20 m depth). This supports that at least 99.95 % of the total downward irradiance (for all water types and depths) are considered within the given range (of 150 m width). Furthermore, typically down to a water depth of 50 m, more than 99 % of the total downwelling irradiance per depth is conserved within a horizontal model width of only 100 m. Below 50 m depth the fractions of diffuse light beyond 50 m horizontal distance from the inlet increases marginally. Thus, a model domain width of 100 m is sufficient for all intents and purposes.

A model domain with 100 m water depth is not always required, especially when studying light fields below small-scaled waves. There a higher grid resolution is more relevant. Three sizes of model ranges are utilized in the follow-up chapter, where water with chlorophyll content of 0.1 mg m^{-3} (relatively clear sea water) is used: 100 m x

100 m (width times depth) with dx = 0.1 m for large ocean waves, 20 m x 40 m (dx = 0.01 m) for small gravity waves, and 7 m x 10 m (dx = 0.005 m) in case of large ultra-gravity waves. The total losses of diffuse E_d fractions at the lateral boundaries amount to 1 to 25 % in up to 40 m depth with ± 10 m, and in the case with ± 3.5 m horizontal grid size losses are not exceeding 6 % (both relative to 150 m model width). Hence, we have to recognize a certain escape of scattered light, in particular with increasing water depth. Nevertheless, the overwhelming majority of radiation is captured within the three different model sizes.

3.3.2.3 MC Model vs. Hydrolight

Horizontal summation of all irradiance parts at a certain depth leads to the total down- or upwelling irradiance at that depth. These values are comparable to results from other radiative transfer codes, which in turn can be used to validate the capability of our MC model to represent radiometric fields for different IOPs. Several benchmark tests have been performed with the well-established *Hydrolight* software[7] (HL), which solves the unpolarized radiative transfer equation with high accuracy [*Mobley*, 1994]. Some test results are shown in Figure 16. The MC radiative transfer results used in the following comparison are those shown in Figure 14. The corresponding *Hydrolight* input parameters are: equivalent constant IOPs, scattering phase function for averaged particles, no wind, use of an idealized sky model, with total E_d above the surface of 1000 mW m^{-2} nm^{-1}, solar zenith angle 0°, and a black sky (no diffuse sky radiation). The model's quality is assessed by means of the percent relative difference ε at defined depths as used in *D'Alimonte et al.* [2010]

$$\varepsilon = 100\ \frac{E_{MC} - E_{HL}}{E_{HL}}, \tag{17}$$

and via the percent root mean square error *RMSE* which is according to *Pan and Zimmerman* [2010]

$$\mathrm{RMSE} = 100\ \left[\frac{1}{\mathrm{n}} \sum \left(\frac{\mathrm{E_{MC}}}{\mathrm{E_{HL}}} - 1\right)^2\right]^{1/2}. \tag{18}$$

[7] Sequoia Scientific, Inc.: www.hydrolight.info

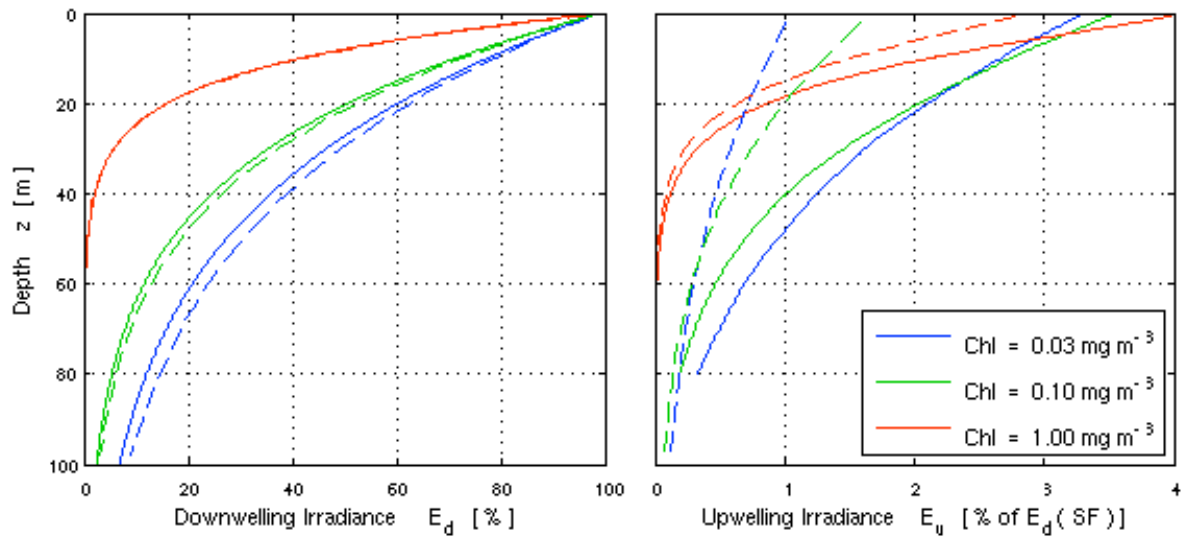

Figure 16. Monte Carlo Simulations (solid lines) vs. *Hydrolight* (dashed lines); left: total downwelling irradiance E_d decrease with water depth for different IOP, right: corresponding upwelling irradiance E_u in [%] of the surface insolation.

With regard to E_d, our MC simulations match the radiation fields very well for all three water cases. Down to a water depth of 30 m, the differences are smaller than 5 %, which is commonly considered an uncertainty threshold for in-situ radiometric measurements [*Mobley et al.*, 1993; *D'Alimonte et al.*, 2010]. Relative differences ε (Eq. 17) and the *RMSE* (Eq. 18) are listed in Table 3 as a function of reference depths used for similar comparisons with *Hydrolight* in *D'Alimonte et al.* [2010] (whose depths are 5, 10, and 15 m), and *Pan and Zimmerman* [2010] (one optical depth) respectively, and for 100 m water depth also. Both references show values in the same order of magnitude. Moreover, for E_d our model delivers results that are close to those from the seven-model inter-comparison study published by *Mobley et al.* [1993].

Table 3. Comparison of MC model and *Hydrolight* according to Eq. 17, and Eq. 18 for Down- and Upwelling Irradiance and different *Chl* Contents (τ = Optical Depth).

	Chl	***ε* [%]**				***RMSE* [%]**		
	[mg m^{-3}]	**z = 5 m**	**z = 10 m**	**z = 15 m**	**z = 100 m**	**τ = 1**	**τ = 5**	**z = 100 m**
E_d	**0.03**	- 0.88	- 1.86	- 2.95	- 21.0	1.83	9.95	11.93
	0.1	- 0.98	- 1.85	- 2.75	- 15.5	0.95	4.95	9.55
	1.0	- 1.23	- 1.75	- 1.55	+ 24.1	0.71	1.33	22.12
E_u	**0.03**	210	205	199	- 68	196	160	147
	0.1	111	108	106	- 70	100	96	77
	1.0	42	40	38	- 49	32	38	41

Small differences between the MC model and HL can be seen directly beneath the surface (see also Figure 19). Because of the internal reflection of upward directed diffuse radiation at the water surface the downward directed values gain extra amounts. In our MC model, this explains a small spillover beyond the 100 % mark of initial intensity near the surface (up to 0.5 m depth). This additional diffuse fraction can amount to maximal

3 % (with water types in this study) in favor with low light incidence and in highly scattering waters (also discussed e.g. in *Mobley* [1994]). The *Hydrolight* software reverts to pre-assembled results of Monte Carlo calculations, where the issue of wind-blown sea surface reflectance and transmittance, and the phenomenon of internal reflection of water-incident rays are taken into account. Our MC simulations show somewhat higher E_d values directly beneath the water surface compared to the three on hand results of *Hydrolight*.

In general, the deeper we go, the larger is the difference to HL (up to 25 % in 100 m depth; note: *D'Alimonte et al.* [2010] show such big divergence already at 15 m depth in case of highly absorbing waters). The lower the particle content is the larger the actual differences are (clearly to see in Figure 16, left). In case of clearest oceanic water (0.03 mg m^{-3}), it seems that the backscattering is increased in the MC model, which also could be linked to the use of *Petzold*'s phase function for averaged particles [*Mobley*, 1994]. Nevertheless, for clear sea water with *Chl* = 0.1 mg m^{-3} (which is used in Chapter 4) the agreement in averaged E_d values between the MC model and *Hydrolight* is good. The differences are still small with changing light incidence angles (not shown); whereas generally accepted E_d at a certain depth is always greater at smaller angles of light incidence (i.e. high sun altitude). Hence, we think our model is appropriate to represent the diffuse downwelling irradiance field.

The comparison between the modeled upwelling irradiances E_u shows strong discrepancies (right hand side of Figure 16). The values are very small, and thus, direct value comparison could be misleading. E_u is described in terms of the percentage of E_d that enters the water column (with 100 %). Near the water surface in total 3 – 4 % of the inserted (downward) radiation is scattered upward (remember Section 3.3.1: around half of the radiation is internally reflected at the surface and the residual leaves the water body). The MC simulations suggest that there is principally more upwelling radiation in the top layer (compared to HL). The percent relative difference is huge for extreme clear sea water: namely three times higher in the MC model; yet less serious in more turbid media (still about 40 % at *Chl* = 1.0 mg m^{-3}). The E_u benchmark denotes a weakness of our MC model. The scattering properties of seawater and in particular the backscattering are essential for the total amount of upwelling irradiance. Accordingly, E_u is sensitive to the choice of the volume scattering phase function.

Looking at the overall picture, the benchmark test shows consistent results. The Monte Carlo model provides slightly smaller values for the total downward directed irradiance, and a similar radiation excess for the total upwelling irradiance. There is consensus that Monte Carlo models for in-water radiative transfer generally have a disadvantage in the computation of upwelling quantities or at great depths [*Mobley et al.*, 1993]. With all uncertainties – concerning the estimation of the water's IOPs (e.g. by satellite imagery), or the light field noise due to a rough water surface, or the technical limitations of radiometric measurements – we show evidence that our MC model is adequate to simulate the downward radiative transfer into the ocean.

3.3.3 Additional considerations about the model output

3.3.3.1 Ratio of direct and diffuse radiation

The fraction of downwelling irradiance that is not scattered along its propagation path is additionally recorded in the model. The graphs in Figure 17 show the ratio of the direct to total diffuse E_d with respect to the water depth and chlorophyll content of the sea water at 0° light incidence. According to Eq. 14, the distance that one out of one million photons undisturbedly transmits through the water body is more than 350 m (with *Chl* = 0.03 mg m^{-3}). Thus, for very low chlorophyll content, at 20 m the percentage of direct unscattered light is 50 %, and still at 100 m depth, around 4 % of the total downward irradiance results from the unscattered light beam. After 60 m water depth only 1 % is left in case of 0.1 mg m^{-3} particle content. With 1.0 mg m^{-3} the direct beam contributes less than 1 % after already 15 m of depth. Of course, the more particles float in the medium the more relevant is the diffuse radiation at larger depths.

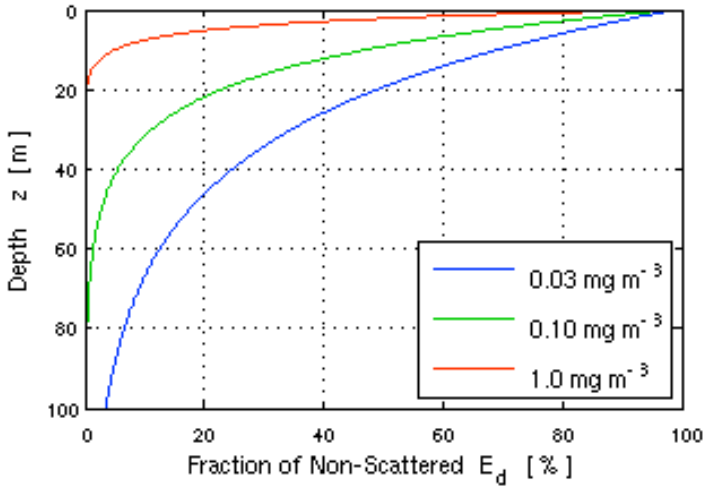

Figure 17. Ratio of non-scattered (direct) to total diffuse downward irradiance (at perpendicular initial direction of propagation).

3.3.3.2 Diffuse sky radiation

So far, we have considered a single light beam from a point light source (the sun) in a "black" sky. In the following the diffuse skylight from atmospheric *Rayleigh* and *Mie* scattering is additionally taken into account. The fraction of diffuse irradiation depends amongst others on the wavelength, the sun position, cloudiness, and aerosol load. For example, an overcast sky with no visible sun is completely diffuse, whereas the ratio of background sky irradiance to total irradiance can be 10 % under very clear sky conditions with high sun at 490 nm wavelength. Here, we have to consider that the absolute values of irradiance input strongly vary between clear sky and overcast.

The underwater E_d distribution that is caused by a uniform diffuse background sky is derived from the following considerations: 1st, the incidence of diffuse radiation is

assumed to be isotropic. 2nd, the half-space is partly shadowed in case of an inclined wave segment. 3rd, the effective transmission angle of each irradiation part is determined via *Snell*'s law, and 4th, the transmission rate of each single portion is calculated from *Fresnel*'s equations.

The two examples in Figure 18 show the downward directed irradiance field due to totally diffuse irradiation through a point-size wave facet (with Chl = 0.1 mg m^{-3}). The color scale again is set logarithmic to resolve the orders of magnitudes of E_d. The distribution on the left graph (arising from a non-tilted wave section) shows a well-defined *Snell*'s window. The cone of light has a width of about 96°. The light propagation is radial-symmetric and covers a relatively large area. The one per thousand level of input irradiance (0.1 %) has a radius of roughly 30 m. A comparison of the total E_d shows similar agreement with *Hydrolight* as discussed above. An interesting aspect of light propagation can be seen on the right picture. The small wave segment is inclined to a maximum angle of 30°. Thereby, a part of the light input is shadowed; the relative light cone is situated between 18° nadir angle to the left and 70° to the right. Because of the transmission angle allocation due to *Snell*'s law, light beams merging near the 18° limit and thus enhance the downward directed radiation input in this region. This feature brings forward very special pattern of light foci with diffuse irradiation. Relative steep and long waves and a high ratio of diffuse insolation are the requirements to form this specific light field characteristic (illustrated in Chapter 4).

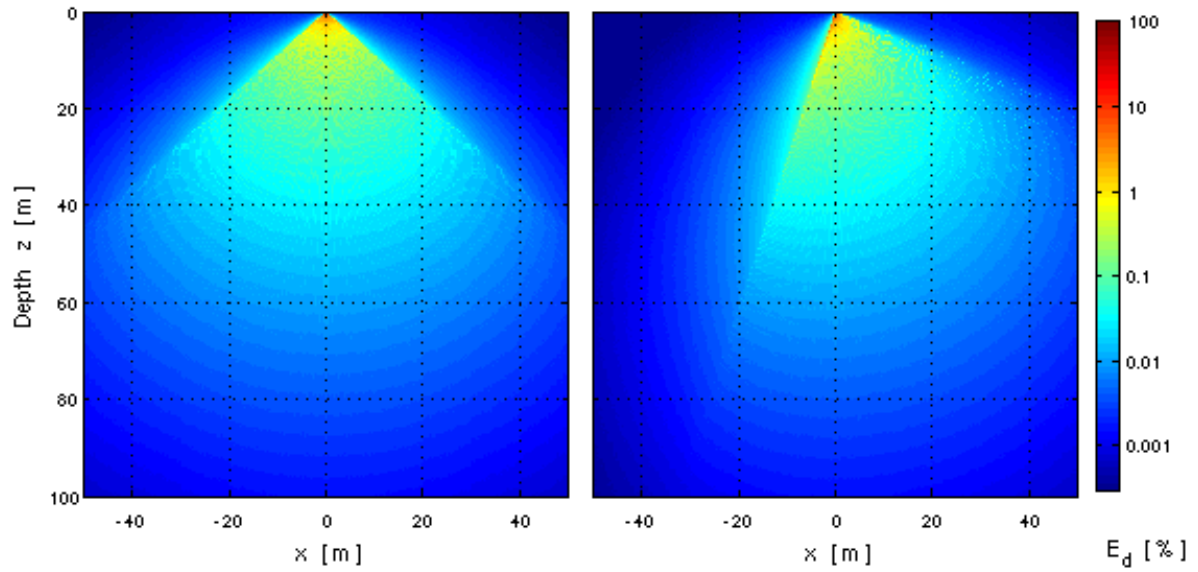

Figure 18. Spatial distributions of downwelling irradiance E_d due to 100 % diffuse insolation, left: for a flat surface, right: for a 30° tilted wave segment (note the logarithmic color scale).

In order to estimate the maximum focusing effect of waves, a fraction of 10 % diffuse skylight is utilized in the follow-up chapters. The effective diffuse and direct light beam input, which enters at a small wave segment, is the sum of both parts weighted with the corresponding ratio [e.g. *Mobley*, 1994]. Some aspects become apparent when diffuse skylight is included in our considerations. With increasing diffuseness of the incoming radiation light can penetrate less effectively into the deep because more light is directed

to the sides. Also, more diffuse atmospheric radiation causes more reflection at the water boundary and thus less transmission of radiation into the water column. The difference just below the surface makes in total around 10 % of the initial value, i.e. 98.8 % (of E_d above the surface) without any diffuse skylight compared to 89.4 % with total cloud cover and no direct light. The effective transmission rate for the 90/10 combination is round 98 %. The composition of the direct solar beam and the diffuse sky irradiance with known sky and water conditions is discussed in more detail in *Pan and Zimmerman* [2010].

3.3.3.3 Simplifications

The top layer of the water column (i.e. 10 m) is of particular importance in terms of wave-induced light fluctuations, since here light flashes are generally most pronounced. The results shown in this work indicate that the major part of radiation propagates on a very small path whose direction is determined by the in-water transmission angle. Especially in clear ocean water the fraction of total downwelling irradiance due to scattering in the first meters of the water body is small compared to the direct light beam (see Figure 17). Furthermore, most of the scattered light is located very close to the initial route, because of the predominance of forward scattering (see Figure 14, left). These considerations give some leeway to simplifications. With regards to the focusing effect the path of the initial light beam contributes most. Along that direction most of the radiant flux is accumulated from neighboring light pencils, in case of clear sea water. In our model representation the attenuation of this pencil of rays is achieved by means of the *Beer-Lambert* law (Eq. 16) using the total absorption properties of the water body. Thus, under these assumptions it is reasonable to only consider the direct beam and neglect all scattered light.

Figure 19 shows a comparison of the total downward irradiance attenuation within the top ocean layer at Chl = 0.1 mg m^{-3} and with 10 % diffuse sky light. The solid line represents the accumulated Monte Carlo output, the dotted line is the exponential decay from Eq. 16 (*Beer-Lambert*), and the dashed line stands for the equivalent *Hydrolight* run. The high correlation of the curves is evident; the root mean square error (Eq. 18) between HL and *Beer-Lambert*'s law is 0.6 % down to 5 m and 0.95 % down to 10 m depth, while the *RMSE* between MC model and the exponential formula is 1.06 % (5 m) and 1.71 % down to 10 m water depth.

The fundamental simplification is the utilization of the ray tracing procedure as used in *Schenck* [1957] or more recently in *Zaneveld et al.* [2001] and in addition a continuous attenuation (absorption) of the individual rays by *Beer-Lambert*'s law. The contribution of all accumulated rays in a detector field provides an adequate estimate of the downwelling irradiance. This method is applicable for clear sea water and down to depths of about 5 m. We use the proposed proceeding for investigations on light field fluctuation in Chapter 4.

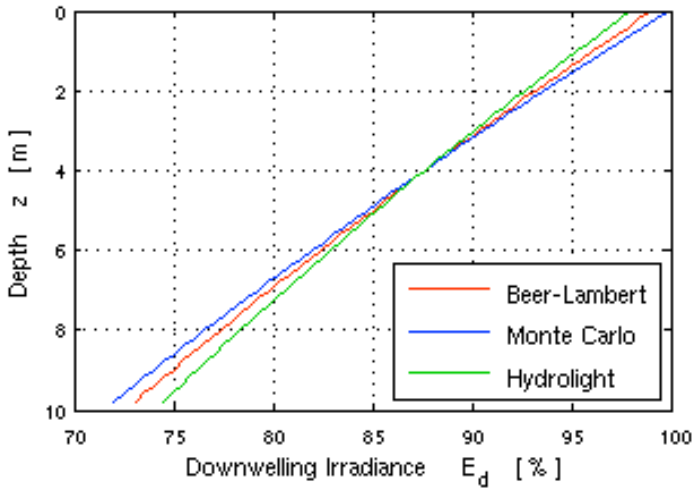

Figure 19. Comparison of the total downwelling irradiance E_d from MC calculations, a HL run, and results from *Beer-Lambert*'s law as stated in Eq. 16 (with *Chl* = 0.1 mg m^{-3}, 10 % diffuse sky radiation, and perpendicular sun insolation).

3.4 Conclusions of the radiative transfer simulations

Based on Monte-Carlo radiative transfer simulations we study the spatial expansion of a single-beam illumination inside absorbing and scattering sea water. In principle, the resulting patterns do not provide new insights into the subsurface radiation field. However, they set the basis for a new approach where the complete irradiance field is calculated by adding such self-contained single-beam results for a set of below-surface zenith angles that reproduce the ocean surface geometry.

Monochromatic light at 490 nm wavelength is considered in the present work. The MC model is applied to water absorption and scattering properties at various turbidities, the latter being quantified by a chlorophyll concentration. The MC method accounts for continuous absorption along the propagation path. The free path length between scattering events depends on the scattering coefficient of the medium. The model's output consists of the downward and upward radiation fluxes at a high spatial resolution. The expansion of the incident light beam is discussed as a function of chlorophyll concentration and the zenith angle at which the light is transmitted after passing the air-water interface. The total downward, upward and net radiation flux can be calculated by means of the MC model. Furthermore, the ratio of direct (unscattered) to total diffuse irradiance is introduced which emphasizes the importance of the diffuse part in calculating the total irradiance. And in addition, the radiative input into water by diffuse sky radiation is deduced from the model.

Benchmark tests with *Hydrolight* document the model's qualification to investigate in-water downward irradiance. Moreover, our presented model is capable of performing high spatial resolution simulations in a large-scale domain, and thus is coequal to a new generation of radiative transfer models that are published recently [*D'Alimonte et al.*, 2010; *You et al.*, 2010].

Finally, an alternative suggestion how to adequately simulate the radiative transfer within the top 5 m water layer with much less effort is provided. The approach is applied together with the MC model for analysis of wave-induced light field fluctuations which is accomplished in the follow-up chapter.

4 Irradiance fluctuations due to surface waves

The solar irradiation in the ocean is subject to enormous variability caused by surface waves. Waves have the optical effect of a lens system; they cause an accumulation and spread of light beams. The size and shape of these lenses determine the optical efficiency in terms of the ability to converge light beams at certain depths. The sea surface is covered by superposed single waves – from very small capillary waves directly associated with local wind (wind shear stress) to fully developed large gravity waves independent of local wind conditions. The spatiotemporal variation of the subsurface irradiance field below an irregular wave train is characterized by the choice of superposed waves. For example in Chapter 2, I showed that small waves due to local induce intensive high-frequency fluctuations in relatively shallow water (roughly down to 5 m); while below 10 m of water depth larger gravity waves dominate the irradiance distribution.

This Chapter is a contribution to the better understanding of the mechanisms of wave-induced E_d variability along the entire illuminated water column. The hybrid-model that is used comprises two components: firstly geometric ray tracing, with fixed transmission direction and initial weight of the solar light incidence at a specific point of the sea surface, and secondly the scattering and absorption of the light within the sea water as described in the previous Chapter 3. The motivation for the splitting is the assumption that light always propagates and attenuates identically within a homogeneous water body; it only depends on the in-water transmission angle of the light and on the optical properties of the water. Thus in the second component we decouple the time-consuming Monte Carlo (MC) radiative transfer simulations for underwater light, whose resulting spatial radiative fields are stored in a database, from the relatively fast geometric ray tracing that accounts for different insolation conditions and sea surface shapes. By means of the proposed model procedure it is possible to study the influence of any possible sea surface profile on the underwater light field. In this thesis, results of almost 300 different wave shapes are presented. The consideration of the actual surface elevation (change of light inlet in vertical z-direction) is one key feature of the model compared to previous models where the wave elevations themselves are not taken into account as a direct source of light fluctuations [e.g. *Deckert and Michael*, 2006; *You et al.*, 2010]. Another advantage of the introduced model procedure is the high-resolved spatiotemporal information on the resulting underwater light field on different scales with water depths down to 100 m.

4.1 Model arrangement

4.1.1 General input data

The model input parameters are selected in such a manner that maximum light field variability can be achieved. Preferred conditions for the most pronounced light fluctuations are described by *Dera and Stramski* [1986], and *Gernez and Antoine* [2009]. All following results are based on the general conditions that are summarized in Table 4. The input data for the Monte Carlo radiative transfer simulations (Chapter 3) are the wavelength and the extinction properties of the water (*Chl*).

Table 4. Model Parameters that are utilized for all following calculations.

Variable	**Value**
Wavelength of light λ	490 nm
Sun zenith angle ϑ	0 °
Chlorophyll content *Chl*	0.1 mg m^{-3}
Refractive index of sea water *n*	1.34
Diffuse sky radiation	10 %

The radiative transfer simulations are carried out for monochromatic light at a wavelength of 490 nm. The attenuation of light in sea water at this wavelength is comparatively small. Thus light can penetrate especially deep, and light field distortions due to the lensing effect can potentially occur within the entire illuminated water column, especially at high sun elevations. For this reason we selected the sun's zenith angle θ to be 0°. Nevertheless, it is possible to vary the angle of light incidence e.g. to simulate the changes of the subsurface irradiance field in a diurnal cycle.

The water body is well-mixed (non-stratified) with homogeneous inherent optical properties. The chlorophyll concentration *Chl* is chosen to be 0.1 mg m^{-3} which corresponds to very clear oceanic water that can be found over a wide range of the tropical and subtropical regions of the earth. The real part of the refractive index of sea water *n* depends on wavelength of light, water temperature and salinity, and is set to 1.34 [e.g. *Segelstein*, 1981]. The imaginary part of *n* indicates the amount of absorption in water that is described in Section 3.1. Whitecaps and bubbles near the surface are not considered in this work as they influence light fluctuations under calm conditions to a minor degree only.

4.1.2 Underwater light propagation

4.1.2.1 Monte Carlo model

Based on the introduced parameters a series of Monte Carlo radiative transfer simulations (Chapter 3) have been carried out to simulate the spatial light propagation within the water column. In this process three model domain sizes are deployed with water depths of 10, 40 and 100 m (more details are given in Table 5). The spatial resolution of the grid, i.e. size and distance of the irradiance detectors, depends on the dimension of the surface shape under consideration. In each case the in-water initial angle has to be varied only. This is the actual in-water transmission angle, calculated after *Snell*'s law with the sun zenith angle and the inclination of the wave segment. With a non-deflected surface, the largest possible transmission angle is about 48°. With a maximum wave tilt of approx. 30° the relative in-water transmission angle is 70°. For this reason the MC simulations are carried out with light incidence angles between 0° and 70°, subdivided in 0.1°, 0.2°, and 0.4° steps, each with 200,000 photons. The output of a MC run is a discretized picture of the irradiance spreading of one single light beam. Each irradiance field is saved in a database, to which we can access for combining underwater light fields.

The picture of subsurface downwelling irradiance E_d due to diffuse sky radiation (from atmospheric *Rayleigh* and *Mie* scattering) is composed from these weighted individual single beam pictures (see Section 3.3.3.2). From this a further data base for underwater irradiance fields from diffuse illumination is set up as function of the wave inclination angle. The total amount of radiation that enters the water at a small surface segment is a combination of the "direct sun" contribution and the diffuse skylight contribution. In this work we assume a very clear sky whereby 90 % of the radiation is coming directly from the direction of the sun (θ = 0°) and 10 % is isotropic diffuse skylight. Some simulations have been carried out for 100 % diffuse sky. They provide considerably different light field characteristics as shown in Figure 22 (e) and discussed in Section 4.2.1.

4.1.2.2 Ray tracing model

The following simplifications for the top 5 m of the water column are assumed (Section 3.3.3.3). Within this layer the light propagation is predominantly determined by the direct (non-scattered) light beam along the initial path and its attenuation follows approximately Eq. 16. For resolving small-scale light fluctuations especially below small waves I utilize the ray tracing procedure as similarly used in *Schenck* [1957], *Nikolayev et al.* [1972], *Stramski and Dera* [1988] or in *Zaneveld et al.* [2001] in combination with continuous light beam attenuation according to *Beer-Lambert*'s law. The total flux of all accumulated light beams within a plane detector field (of 2.5 mm width) is an adequate estimate of the downwelling irradiance E_d.

4.1.3 Representation of the sea surface

The ocean surface is a complex three-dimensional structure that arises from superposition of various waves with different size, orientation and origin. Single waves interact with each other in a nonlinear manner and make it difficult to create a realistic surface representation. In terms of the subsurface irradiance field the interference of different sized and shaped waves is an important issue. They produce radiation noise and disable the development of a clear and homogeneous irradiance pattern. For the sake of understanding the principle structure of light fluctuations along the water column we first look at regular single waves and later at irregular wave structures.

Only gravity waves are regarded in this section (wavelength $L > 1.73$ cm). The principle restoring force of these waves is gravity, in contrast to capillary waves, where mainly the surface tension acts as the maintaining force. Capillary waves are important in the context of remote sensing of the oceans, and they do play a role in light field fluctuations just below the surface. However these waves are not considered in this study. The smallest realized horizontal grid (detector) resolution dx is 2.5 mm, which is about the same order of magnitude as the head size of common radiometers for high-frequency sampling. The cross section of our irradiance sensor for comparative measurements (a *RAMSES-ACC-VIS*) is 5 mm. The shortest single wave that is accounted for in the present thesis is 2.5 cm long. Nevertheless, all waves are horizontally resolved with 0.1 mm (in x-direction).

4.1.3.1 Regular single waves

The waves are assumed to be long crested (constant along y-direction) and quasi-stationary. Therefore, we can use the 2D model to describe the spatial subsurface light field. In addition we know that the time rate of change of the underwater light field directly corresponds to the phase speed of the surface wave. Long water waves propagate faster than shorter ones, an effect that is called dispersion in fluid dynamics. In linear wave theory (*Airy* theory) the water wavelength L and the wave period T are related (for deep water) by:

$$L = \frac{g}{2\pi} T^2, \tag{19}$$

in which g is the acceleration of gravity (same as Eq. 5). And vice versa, this relation allows inferring dominant surface wavelengths from time series of irradiance measurements at certain depths.

The shape of the wave is very important in determining the resulting light field. In previous publications sinusoidal wave structures are deployed in the radiative transfer models [*Schenck,* 1957; *Nikolayev and Khulapov,* 1976; *Stramski and Dera,* 1988; *Zaneveld et al.,* 2001; *Deckert and Michael,* 2006; *D'Alimonte et al.,* 2010]. Describing water waves as a sine curve is feasible for vanishingly small amplitudes, with wave

steepness H/L (wave height to wave length) up to 0.006. Beyond that steepness waves are represented by means of *Stokes* wave theory of higher order. Substantial deviations occur in the shape, i.e. the wave crest is higher and sharper and the trough is flattened (see Figure 20 top), and in the hydro-dynamical behavior, e.g. the *Stokes* wave moves slightly faster than a small-amplitude wave. Based on the formulation of *Kinsman* [1965], the nonlinear elevation ζ of any gravity wave can be sufficiently described by means of *Stokes* theory of fourth order:

$$\zeta = \zeta_a \cos kx + \frac{1}{2} k\zeta_a^2 \left(1 + \frac{17}{12} k^2 \zeta_a^2\right) \cos 2kx + \frac{3}{8} k^2 \zeta_a^3 \cos 3kx + \frac{1}{3} k^3 \zeta_a^4 \cos 4kx, \tag{20}$$

where ζ_a is the amplitude, k the wave number, and kx the phase. The term $k\zeta_a$ stands for the wave steepness, too. The theoretical limitation of the formula is for waves with maximum H/L = 0.14 (for deepwater); steeper waves break.

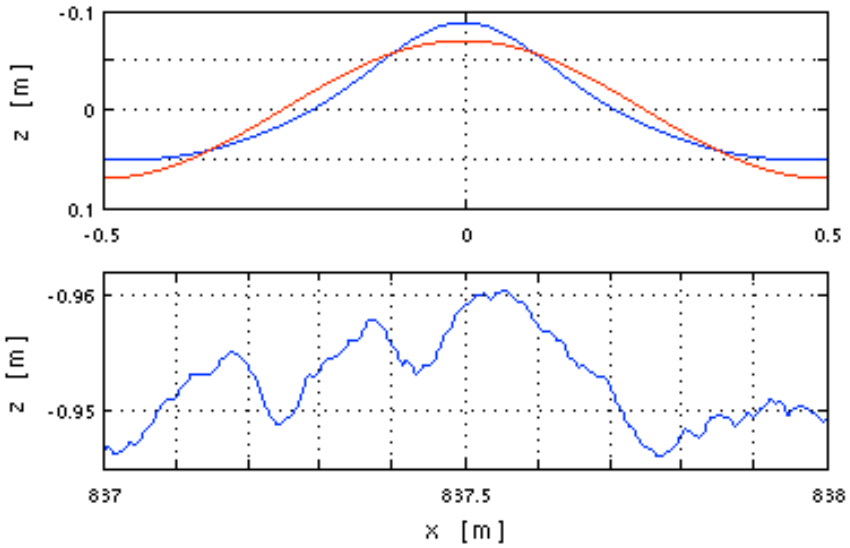

Figure 20. Water surface profiles; top: sine curve (red) vs. Stokes wave of 4th order (blue) both with maximum steepness H/L = 0.14; below: detail of the utilized 500 m irregular wave profile (remark: z is defined downward positive).

The implemented single waves are classified into five categories each with size adapted model grid dimensions (details in Table 5). The first three wave classes cover so called ultra-gravity waves with periods T of less than 1 s. These waves are particularly associated with local winds (depending for example on the fetch length). Class four and five contain fully developed gravity waves that also arise from wind, but they are not necessarily associated with the local wind situation as waves propagate away from their area of origin. According to the ocean wave statistics by *Hogben and Lumb* [1967], 95 % of all visually observed sea conditions in the tropics and still more than 90 % globally (for all seasons, all directions, and all areas) are accumulated within wave category five. One may argue about the relevance of almost 200 m long and 7.5 m high waves regarding subsurface radiation fields (since their occurrence is very unusual), but for the sake of completeness I show their potential of influencing the radiation field in

deeper water. In general, most wind-generated waves have a steepness in the order of H/L = 0.03 to 0.06 and very rarely more than 0.09.

Table 5. Classification of the single wave types with details for corresponding model domains.

Wave class		**1**	**2**	**3**	**4**	**5**
Description of wave class		Small Ultra Gravity	Medium Ultra Gravity	Large Ultra Gravity	Ordinary Gravity	Ocean Waves
Wave length	L [m]	0.025 – 0.1	0.15 – 0.5	0.6 – 1.4	1.5 – 20	25 – 192
Wave period	T [s]	0.12 – 0.26	0.31 – 0.57	0.6 – 1.0	1.0 – 3.6	4 – 11
Wave height	H [m]	0.0008 – 0.009	0.0045 – 0.045	0.018 – 0.126	0.045 – 1.8	0.5 – 7.5
Wave steepness	H/L [-]	0.03, 0.06, 0.09	0.03, 0.06, 0.09	0.03, 0.06, 0.09	0.03, 0.06, 0.09	0.002 – 0.13
Appl. Method		Ray tracing	Ray tracing	Monte Carlo	Monte Carlo	Monte Carlo
Grid depth	z [m]	2	5	10	40	100
Grid width	x [m]	-	-	5	20	100
Vertical res.	dz [m]	0.001	0.001	0.01	0.05	0.1
Detector width	dx [m]	0.0025	0.0025	0.005	0.01	0.1
Sampling rate	f_s [Hz]	80 – 158	194 – 353	194 – 296	153 – 559	63 – 173

4.1.3.2 Irregular wave trains

In this Section one irregular wave profile is treated, to show the functional reliability of the model procedure and to point out the importance of wave-wave interactions regarding the light field. Detailed sea state analysis will be subject to future works (see outlook Chapter 5.1). For the purpose of a comparison with measurement data, I develop an analytical surface description that corresponds to observed sea state parameters. The data have been collected onboard the RV *Polarstern* (research cruise *ANT-XXVI/1* [*El Naggar and Macke, 2010*] – at the 10/30/2009) in the tropical North Atlantic (19°4'N, 23°W). During sampling time, the trade wind blew with 11 m s^{-1}. The wind sea was registered with 1.5 m wave height and 5 s peak period. An additionally 2 m high and 9.5 s long swell wave was dominating the sea state at that time.

The applied sea wave spectrum consists of two parts; the long waves were handled with a double-peaked wave spectrum according to *Ochi and Hubble* [1976], while the short directly wind-driven waves were represented by means of a formulation by *Elfouhaily et al.* [1997]. Out of the sea wave spectrum weighted harmonics are extracted and then superposed with random phase, which corresponds to linear wave theory. The resulting wave profile shows a *Gaussian* slope distribution. The approach does not allow for nonlinear wave interactions, which would lead to steeper wave crests and shallower troughs. Further small-scale surface irregularities, as e.g. the phenomenon of wind-

induced capillary wave trains ahead of steep wave crests [e.g. *Longuet-Higgins*, 1963] and the subsequently slope asymmetry as accounted for in the *Cox-Munk* slope distribution [*Cox and Munk*, 1954], are not considered either. In any case the modeled wave profile is very close to reality as it conforms the stochastic requirements of the observed sea state. Figure 20 shows a section of the implemented irregular wave train. The total wave profile has a length of 500 m with 0.1 mm horizontal resolution. The characteristic peaks of the used sea spectrum, i.e. at 140 m length (swell), 40 m (wind sea), and 1.7 cm (gravity-capillary), are clearly visible.

4.1.4 Superposition of individual light fields

The basic concept of our model combines the advantages of both geometric ray tracing at discrete wave segments and MC radiative transfer calculations in sea water. Thus, an exact positioning of diffuse and direct parts of single light beams below the surface is possible. The actual superimposition of downward irradiance fields follows the procedure as described below. Figure 21 assists the description by a schematic diagram of the superposition of self-contained E_d fields.

1) The overall grid system with global coordinates x and z is initialized. The grid dimension depends on the length of the surface structure and the size of the single beam light field. For example in case of wave class five individual light fields are 100 m deep, 100 m wide (each with photon inlet at the top in the middle), and resolved with 0.1 m both horizontally and vertically. Hence the horizontal detector width is 10 cm. Thus, the overall grid has the same spatial resolution and involves an area of about 100 m depth, and the total horizontal grid width is made up of the length of the wave (e.g. 156 m at 10 s wave period in Figure 21) plus two times 50 m, at the beginning and at the end respectively. The area of interest is the domain below one complete wave cycle which is located in the center of the overall grid. The lateral boundaries of this area are affected by diffuse radiation that enters the water column up to 50 m horizontally apart from the inner grid.

2) The regular wave (extended by two times 50 m) is localized in the global grid. Now for each horizontal wave segment a vertical position of the light inlet into the water body and a corresponding wave slope can be allocated.

3) In the next step the global in-water transmission angles and the transmission rates are determined via *Snell*'s law and the *Fresnel* equations using the relative sun position and the wave slope.

4) Starting from left to right, the total light inlet within a 10 cm wide wave segment is determined. Here for every wave facet of 0.1 mm width the corresponding downward irradiance fields for the single beam and the diffuse skylight are taken from the database and weighted according to the transmission rate and the ratio of direct-to-diffuse insolation.

5) The complete 100 m x 100 m underwater light subfield that arises from a 10 cm wide light inlet at the surface must now be adapted to the global coordinate system. The vertical light inlet (point [0, 0] of the subfield) is exactly positioned in accordance to the current surface elevation. All downward irradiance values from the subfield must be interpolated to global coordinates and then added up to the overall grid.

6) The part of the 100 m x 100 m light field above the water surface is cut off, which represents a fundamental model inaccuracy that is discussed in the following section.

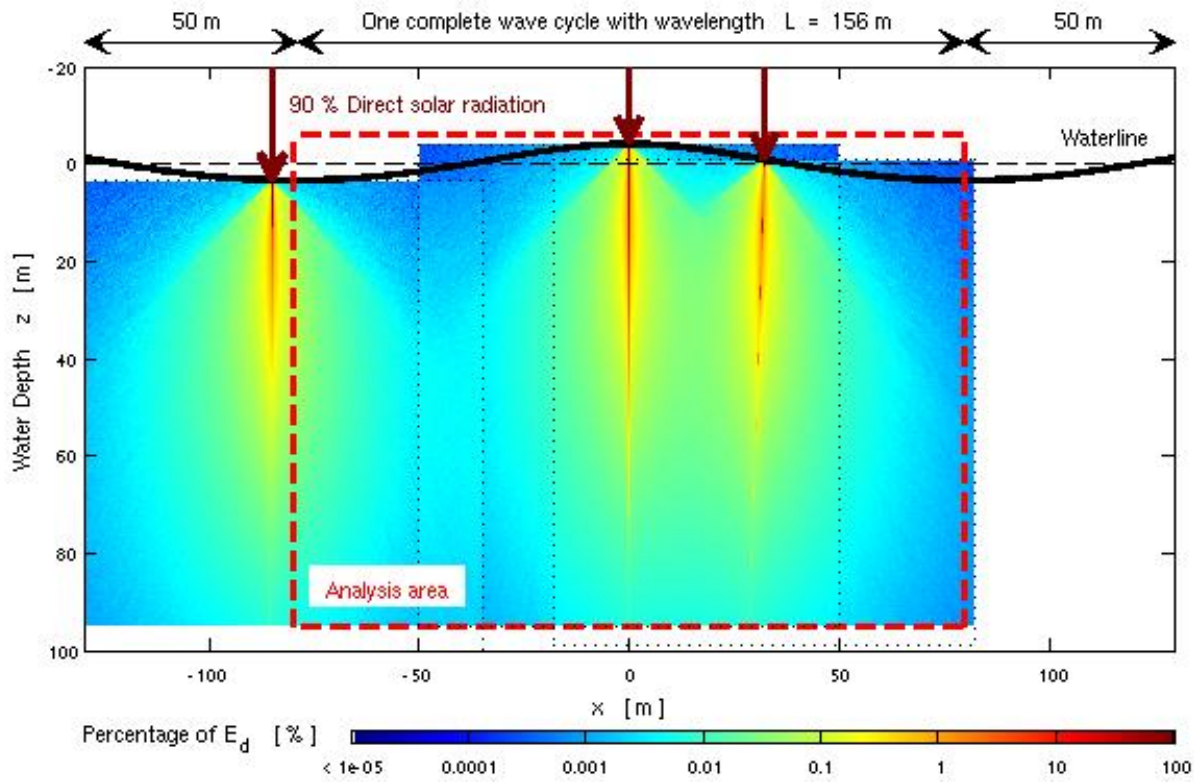

Figure 21. Schematic diagram of the overall grid according to a single regular wave: At three points light beams enter the water body (with 10 % diffuse skylight and 90 % directly from the sun). The corresponding subsurface patterns of individual and independent light propagation influence the actual analysis area (red dashed framed), which covers one complete wave cycle in *x*-direction and maximal 100 m in *z*. The radiative fractions above the deflected surface are separated and neglected.

The statistical evaluation of the subsurface downward irradiance refers to the analysis area below the complete single wave with one crest and one trough only. The vertical size of the water column between the actual surface elevation and a detector point is defined as reference or true depth z_t. In the following all radiative data bear on this reference depth, so that the depth contours (of same hydrostatic pressure) are always shaped as the water surface. The reference depth is handled differently in other publications e.g. in *D'Alimonte et al.* [2010]. They refer to a virtual depth displaying the surface wave effects on the pressure gauge and therefore to depth lines of same pressure. This approach makes sense but it is based on linear wave theory, which makes an adaptation onto nonlinear wave systems intricate.

4.1.5 Estimation of the model accuracy

Two points affect the accuracy and reliability of the model procedure with superposed individual light fields: 1st backscattering of upwelling photons at the curved sea surface is not accounted for; and 2nd the raster image shows numerical artifacts (informal: *jaggies*).

A conceptual error of our superposition model arises due to the fact that internal reflection would come from virtual surfaces out of the wave train. Recall that the downward irradiance fields described in Chapter 3 result from an extended plane surface segment. For this reason and because of the small contribution to the overall irradiance field, internal reflections of the upwelling photons at the curved surface back into the water column are neglected. However, especially for very steep waves the downward internally reflected radiation might affect the total irradiance to some extent. With the strongest wave curvature under consideration and the given environmental conditions (Table 4) we have estimated the total amount of the neglected diffuse down-welling irradiance to be smaller than 0.6 % of the total inserted irradiance. By the way, the commonly considered uncertainty threshold for in-situ radiometric measurements is about 5 % [*D'Alimonte et al.*, 2010], and the detection accuracy of our comparative data is stated to be better than 6 – 10 % (depending on spectral range).

In this context we have to compare alternative models for wave-induced irradiance fluctuations near the surface by *Plass et al.* [1975], *Deckert and Michael* [2006], or *You et al.* [2010]. These different models have the photon inlet always at the z = 0 m level (z-invariant), with random slope allocation according to surface statistics or with a fixed succession of predefined wave slopes. The surface elevations are not taken into account as a direct source of underwater light fluctuations. For this reason it is difficult to separate the effects of E_d variations due to differing water depth caused by waves from those variations due to lensing. Obviously, this model bias is largest near the surface. In this respect our model (and also the model by *D'Alimonte et al.* [2010]) represents an improvement concerning the E_d field near the surface and especially at open sea with high surface elevations.

The second point that systematically disturbs the resulting irradiance picture arises from the discrete registration of the light field with relative low resolution. The direct light beam (that dominates the irradiance field) is mapped as a stair-like line, thus the differences between neighboring grid cells can be high. These so called *jaggies* become apparent as visible stripe pattern especially above 40 m of water depth (see Figure 22). Due to the superimposition of light regimes, local minima occur at the sides and punctual maxima appear directly below the wave crest; the mean values stay untouched because of the energy conservation. Thus, the resolution artifacts interfere with the determination of minima, maxima, and other statistical values per depth layers. In the end the light field is subject to some variability due to overlaid waves anyway. The principle character trait of the wave-induced light field can be defined precisely.

4.2 Results of the irradiance fluctuation simulations

4.2.1 Downwelling irradiance fields below single waves

Water waves do not represent perfect lenses and therefore do not form perfect focal points. There is always some degree of distortion or spherical aberration introduced by the wave, which is further amplified by the nonlinear wave shape. Figure 22 shows some examples of underwater downwelling irradiance fields E_d (x, z) due to regular single waves. The white color at the logarithmic color scale defines 100 % E_d insolation above the surface, bluish colors mark smaller E_d, red larger E_d values. The horizontal sum of all E_d values at a depth z_t is equal to the total downwelling irradiance, which always decreases exponentially with water depth. Light fluctuations are commonly described by two parameters: The first parameter is the coefficient of variation CV

$$CV = 100\ \frac{\sigma}{\mu}, \tag{21}$$

given as the ratio of the standard deviation σ and the mean downwelling irradiance μ at the reference depth z_t (this formulation is different to Eq. 2, where CV is calculated using the median). The second parameter is the normalized downwelling irradiance, denoted as χ in this work:

$$\chi = \frac{E_d}{\mu}. \tag{22}$$

It describes the multiple of a punctual E_d value compared to the mean irradiance at a depth. *Dera and Stramski* [1986] defined irradiance pulses that exceed the mean irradiance by a factor (here χ) of more than 1.5 as underwater light flashes.

Figure 22 (a) illustrates light fluctuations below a typical small ultra-gravity wave of class one (details are given in the caption). In this particular case the first focal point is very shallow at 10 cm depth with an E_d maximum of 700 % of the value above the surface. In z-intervals of around 40 cm, the second, third, fourth and so on focal points are developed by neighboring parts of the regular wave. The corresponding E_d accumulations are 390, 320, 290, and 250 %. The irradiance enhancement compared to the mean is χ = 7 at the focal point in this case. It decreases in the same manner as the maximum E_d values. Waves with lengths shorter than 10 cm (capillary waves and small ultra-gravity waves of class 1) cannot generate light flashes (χ = 1.5) in depths greater than approximately 5 m.

In case of the second wave the maximum irradiance at the focal point is around 2700 % which corresponds to a local enhancement χ of 28-times the average irradiance at 1 m depth (Figure 22 b). Even at 5 m water depth the maximal E_d is 500 % ($\chi \approx 6$). The light collection length of this "laboratory" wave is 40 cm in the example and the detector size dx is 2.5 mm. Figure 22 (c) shows the light field beneath a 6 m long wave with grid cell width 1 cm. The focus is at 7.5 m depth with almost 2000 % irradiation enhancement ($\chi \approx 25$). Irradiance values of 100 % of the surface value can penetrate down to 20 m water depth. At that depth the mean irradiance has decreased to about

50 % so that χ is two. The fourth example wave (Figure 22 d) develops its focus in 27 m depth with an enhancement of 260 % ($\chi \approx 6.6$, with dx = 10 cm). This forth wave can cause light flashes down to 50 m water depth. At this depth the mean irradiance has decreased to round 20 % but locally (or short occurring) 30 % can be reached (twice per wave cycle). Of course all these waves are perfectly smooth and thus not realistic. However, the analysis shows the potential mechanisms for producing light flashes and the magnitudes of irradiance variations especially below the top 10 m of the ocean.

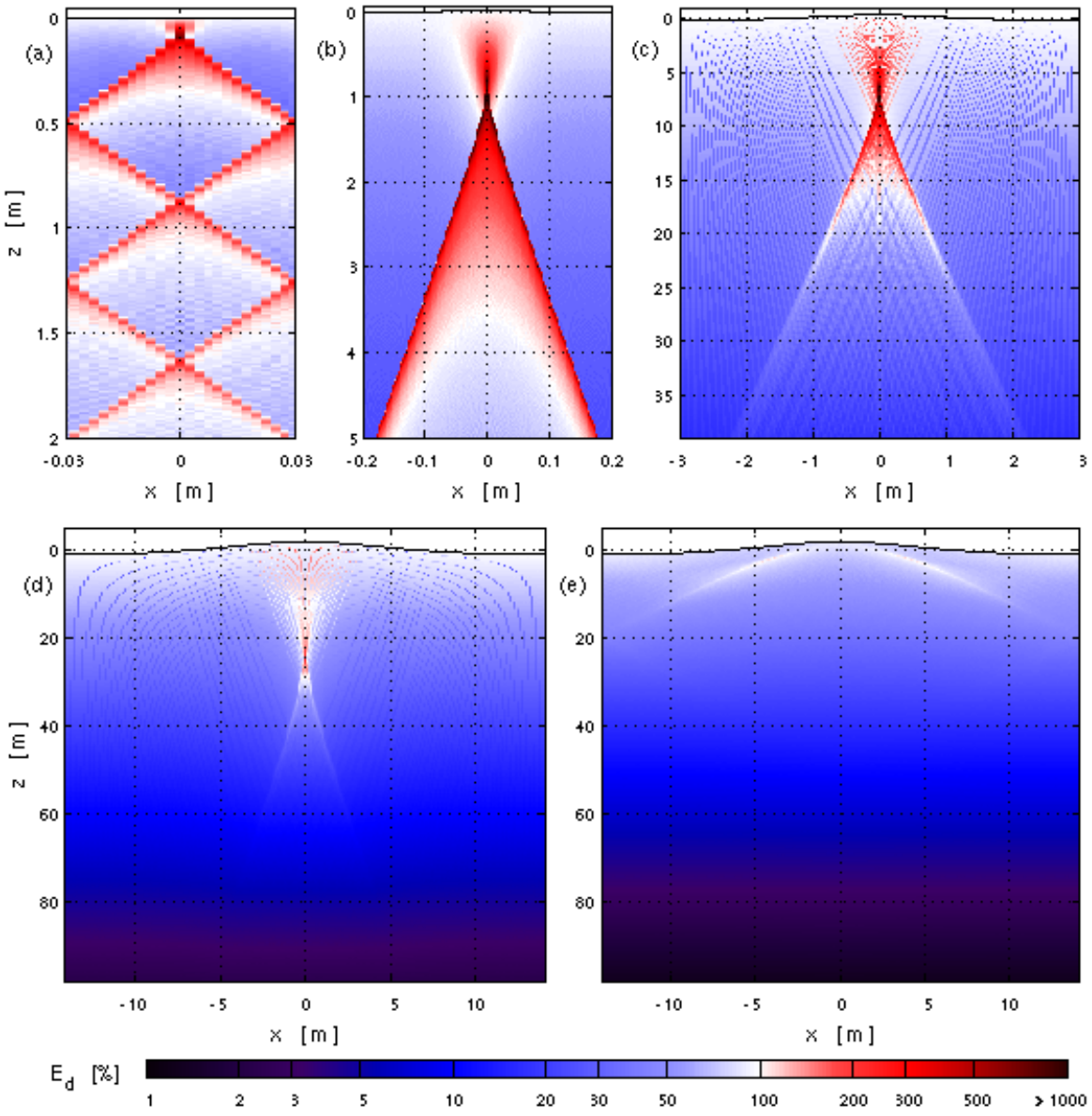

Figure 22. Examples of downward irradiance field beneath single regular waves; (a) wave of class one (L = 6 cm, H/L = 0.09, dx = 2.5 mm); (b) wave of class two (L = 40 cm, H/L = 0.06, dx = 2.5 mm); (c) wave of class four (L = 6 m, H/L = 0.09, dx = 1 cm); (d) ocean wave (L = 26 m, H = 3 m, T = 4 s, dx = 10 cm); (e) same wave as left but with total (100 %) diffuse skylight instead of 10 % at the clear sky case (note the logarithmic color scale).

The impact of the sky diffuseness on the irradiance field is shown in Figure 22 (d) and (e). The same wave yields different light field characteristics under clear sky (90 % direct and 10 % diffuse sky radiation) and overcast sky conditions (100 % diffuse radiation). At clear sky the focal point is well developed directly beneath the wave crest. In case of diffuse radiation a part of the light input is shadowed by the inclined wave segment and the typical light cone (associated with *Snell*'s window) is sidewise shifted as described in Section 3.3.3.2. From this it follows that most diffuse radiation is accumulated below that wave sections where the facets are most tilted. We have two local irradiance maxima that are marked as the white areas down to 15 m (Figure 22 d). The E_d maximum of 109 % (relative to the surface irradiance) is located at z_t = 3 m depth, and it appears twice per wave cycle. Below 20 m depth there is no considerable E_d variation any more. In general, there is less total downward irradiance per depth due to the lack of the direct light beam, which is well pronounced under clear sky conditions. The effect of daylight diffuseness on the focusing of sunlight by sea waves is discussed in detail by *Stramski* [1986], *Stramska and Dickey* [1998], and *Gernez and Antoine* [2009]. Their different observations agree that light fluctuations under cloudy sky conditions are clearly slowed and that they have much smaller amplitudes. An explanation is that smaller waves cannot build up significant irradiance enhancements in this respect. Relatively long and steep waves are more capable in developing considerable irradiance variance. Even though the occurrence of relative radiative peaks is more frequent, i.e. focal enhancements appear twice per wave cycle instead of one time under clear sky, the total mean fluctuation frequency under an irregular sea is decreased due to the major influence of larger waves.

The essence of all single wave simulations is assembled in Figure 23. The (logarithmic) color mapping indicates the maximum normalized downwelling irradiance χ_{max} that is possible at the given wavelengths and at the three wave steepness under consideration. The ordinate shows the reference depth z_t. Along the x-axis varies the surface wavelength L and on top the corresponding wave period T, respectively the light fluctuation period according to Eq. 19. The wave classes 1 to 5 are framed to underline the changing detector sizes dx. Three diagonal lines of irradiance enhancement are clearly visible. They correspond to the focal points at the particular wavelengths whereat the upper line corresponds to the steepest waves with H/L = 0.09, the middle line is for H/L = 0.06, and the lower line for flat waves with H/L = 0.03. Remember that most wind waves have a steepness between 0.03 and 0.06. Especially at class 1 the foci of higher order play a certain role as described above. Their irradiance enhancements are also visible but less well pronounced. The figure basically shows the range of impact for certain waves types. For example, the most intense light fluctuations at 1 m depth (with E_d maxima of more than 500 %) arise mainly from waves with lengths of 10 cm to 1 m (ultra-gravity waves), whereas at 10 m depth waves of 1 m to 10 m length cause most fluctuations (ordinary gravity waves). For the first three wave classes flatter waves develop more intensive and deeper irradiance pulses at a given wavelength. Capillary waves (L < 1.73 cm) do not directly cause the most intense light fluctuations. The strength of enhancements at the focal points clearly decreases at the left hand side of the

figure. More relevant are the well pronounced narrow light rays that follow from such very small waves. Those rays are clustered somewhat deeper due to longer waves (see Figure 22 a). It is obvious that the longer the wave is the deeper is its potential impact. Even 200 m long swell waves can develop an enhancement of χ = 1.15 below 90 m of water depth; *CV* can be up to 6 %. The short irradiance pulses that distinctly exceed the mean irradiance along the entire water column may be of ecological significance, especially in the deep light limited zone. Note that only selected wavelengths are studied. The white vertical stripes represent information gaps at wavelengths in between.

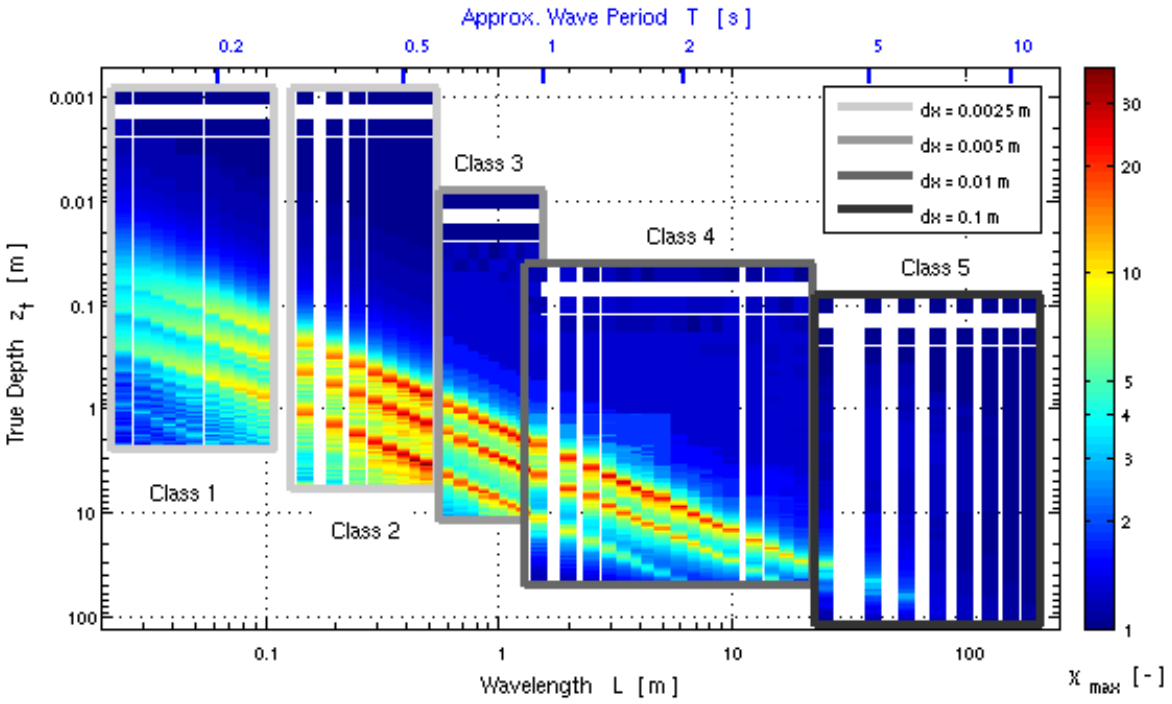

Figure 23. Maximum possible normalized downwelling irradiance χ_{max} due to single waves per water depth z_t and in accordance with the surface wavelength *L* (and period *T* at the top); the five wave classes refer to different detector sizes *dx* (note the logarithmic color scale).

The magnitude of irradiance enhancement depends on the detector width *dx* and the sampling rate, e.g. a 10 cm wide radiation sensor below a 10 cm long wave cannot resolve any enhancement; it only measures the mean value at that depth. For the present study we make use of four different spatial grid sizes *dx* which basically depend on the deployment depth. The growing spatial resolution in the models mirrors the extension of the radiometer integration time, i.e. in shallow clear water our hyper-spectral radiometer samples with 4 ms (effectively two spectra per second), while at greater depths the data integration can last for up to 8 s. The conversion of the areal detector size *dx* to a corresponding temporal information, the sampling rate f_s in [Hz], is approximated by means of Eq. 19 and is listed in Table 5, too. The equivalent sampling rate depends on the surface wavelength, because of the faster propagation of longer waves.

Figure 24 shows the maximum possible radiative enhancements χ_{max} per water depth that originate from the lensing effect of the steepest single waves (H/L = 0.09). Here we vary the detector size dx. Of course the smaller the sensor head the higher is χ. An irradiance pulse can (theoretically) exceed the mean irradiance by a factor of 40 at a water depth of 1 m with respect to a 2.5 mm sensor. At the same depth a 5 mm collector would capture a maximum factor of around 20, with 1 cm χ_{max} = 12. With a detector length of dx = 10 cm the enhancement is less than a factor of 3. The corresponding wave that causes the light pulse is 80 cm long. In theory, χ-values of more than 50 are possible in the corresponding depths with both detectors 2.5 mm and 5 mm. The model domain sizes are restricted for the sake of credibility of the results, e.g. the model with grid resolution of 2.5 mm does not account for light beam spreading (see Section 4.1.2.2) which definitely plays a role for the estimate of the radiative enhancement within the focal point beyond around 2 m depth. The larger the focusing surface wave lense, the more energy is concentrated into the focal point. On the other hand, larger waves imply deeper focal points and thus stronger attenuation. It is obvious that an optimum between both must exist for a given water turbidity. Irregular surface waves, however, make it difficult to obtain such an optimum situation for light enhancement under real conditions. The greatest possible depth of light flashes (χ = 1.5) is at approx. 80 m, and this is caused by an over 60 m long wave (T = 6 s, H = 5.5 m, and thus rare occurrence probability). At 80 m depth E_d is on average 5.5 % under the given conditions, the narrow irradiance peak accumulates up to 8.3 % in regular intervals of 6 s, which equals the actual mean E_d at 69 m depth.

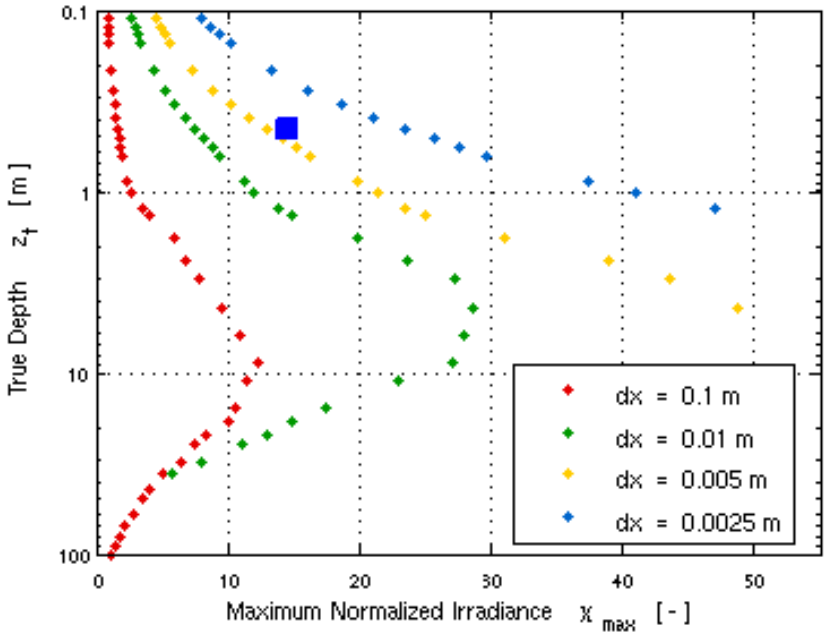

Figure 24. Maximum possible normalized downwelling irradiance χ_{max} due to perfectly shaped single waves plotted against depth level z_t and with respect to the different detector sizes dx. The blue square marks a maximum value that was measured (see text).

Gernez et al. [Ocean Optics Conference, 2010] presented measured E_d data (sampling rate 1 kHz, light wavelength 532 nm), where at 45 cm water depth the maximal normalized irradiance χ reached a value of 14, marked with the blue square in Figure 24. Other jet unpublished data of the same group show a maximum χ of 13 at 0.86 m depth [*Gernez et al.*, 2011]. In theory we would expect the theoretical maximum χ_{max} to be 23 at that depth (with 490 nm and dx = 2.5 mm) which is due to a 35 cm long perfectly smooth surface wave. *You et al.* [2010] showed also extreme values with equivalent sampling parameters, where χ_{max} is larger than 8 at 0.86 m depth, and more than 4 at 1.7 m depth. These are the highest values published so far. These data underline the importance of the superposition of different sized waves; the effect restricts the ability of waves to form such efficient lensing systems. Nevertheless, in particular cases perfect regular waves of great steepness and of the mentioned magnitudes can occur, for example the wave system on a smooth lake that is caused by a motor boat.

4.2.2 Downwelling irradiance fields below a sea state

Light fluctuations below irregular wave profiles are shown in Figure 25. The downwelling irradiance distributions where simulated using three model domains with different resolutions. The first model covers an area of 400 m horizontal expansion and 100 m depth with dx = 10 cm (note: the wave profile length is 500 m with 0.1 mm resolution, where in each segment 200,000 photons are regarded, this corresponds to 10^{12} photons in total). Figure 25 (a) shows a 100 m x 100 m selection. The second field includes a domain of 150 m x 40 m with 1 cm resolution. Again, a zoom in is shown in Figure 25 (b). Finally, I discuss a high-resolution model domain with 2.5 mm horizontal detector size that covers an area of approx. 5 m x 5 m to study near surface fluctuations. The corresponding irradiance field is shown in Figure 25 (c). The surface consists of a well pronounced wave crest which affects the resulting light regime to some degree. Here we want to underline the importance of the actual surface elevation on the radiative allocation, since the statistically highest wave H_{max} under the given conditions can be almost 5 m. The disregard of such large wave amplitudes (i.e. vertical photon inlet only at the mean waterline) is a potential source of errors, when simulating underwater light fluctuations. The color coding in the figure is logarithmic again with red colors for E_d > 100 % and bluish for decreasing values.

Figure 25 (c) nicely shows the impacts of very small waves. Waves of around 2 cm length (transition range of capillary to ultra-gravity waves) dominate the surface profile at that scale. They build up clear single stripes of E_d enhancements shown in red. These single rays are further refracted by overlaying waves of 10 cm to 50 cm length which leads to intensified light beam grouping at true depths of 1 to 4 m. With increasing depth the fine differentiation of single rays wears away. The unscattered (direct) light beams approach each other. Image analysis of spatial underwater light fields at different depths (Chapter 2) confirms the increasing blurring of small-scale structures [*Hieronymi and Macke*, 2010].

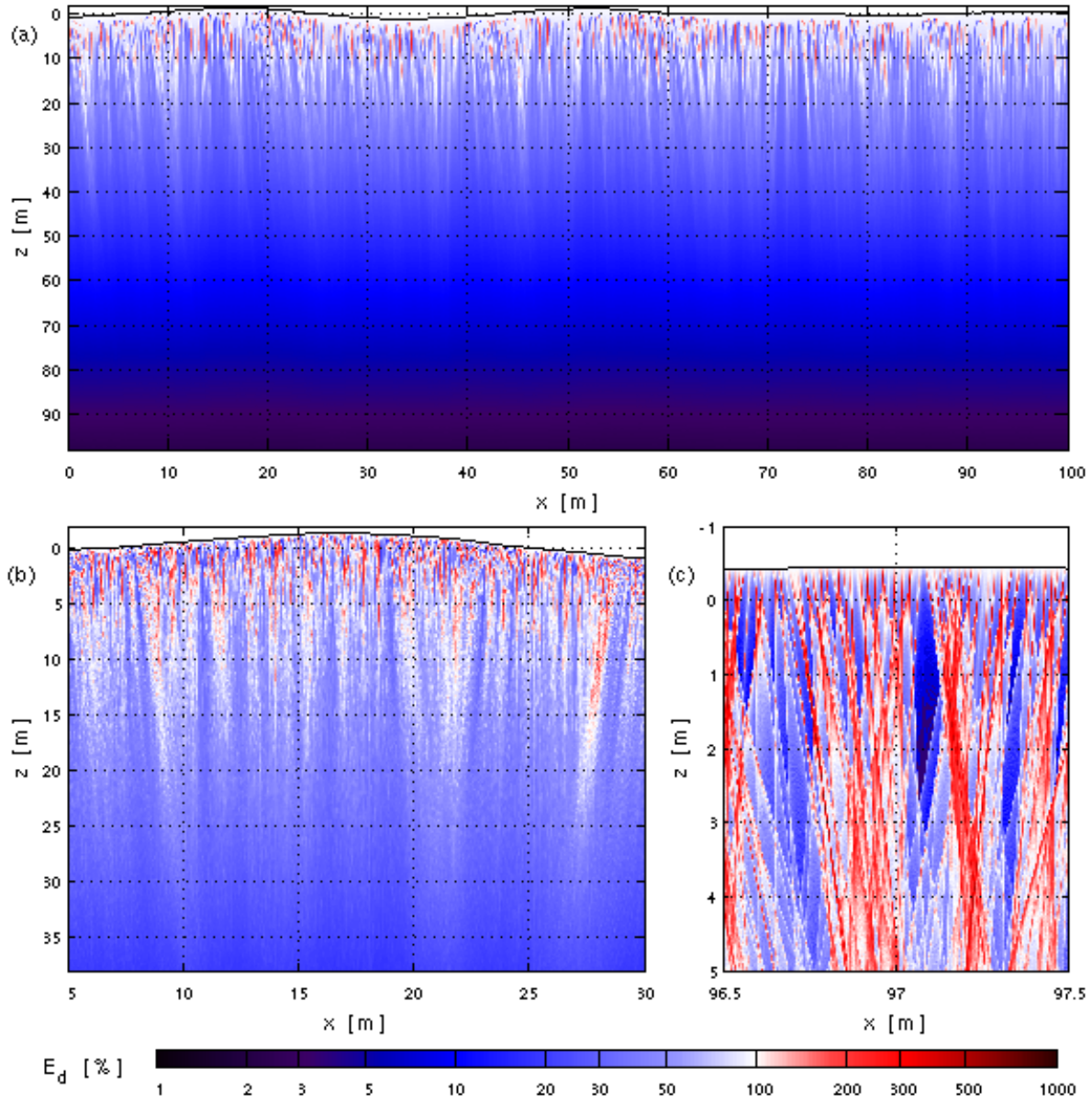

Figure 25. Downwelling irradiance E_d distribution beneath an irregular wave profile; (a) detail from a 100 m long wave section with detector width dx = 10 cm; (b) light field with resolution dx = 1 cm; (c) zoom into the fine structure of near-surface fluctuations with dx = 2.5 mm (note the logarithmic color scale). The simulated environmental conditions (e.g. zenith angle and IOP) correspond to observed conditions at the 10/30/2009.

In comparison to a plane surface the total downwelling irradiance (sum of all individual E_d portions per z_t) is reduced along the water column due to the deflected or "wind-blown" sea surface. This is generally accepted and in agreement with measurements and other models [e.g. *Plass et al.*, 1975; *Mobley et al.*, 1993]. The actual importance of larger waves without local wind-effects must be subject to future research (this issue is addressed in the Outlook Chapter 5).

The change of the normalized downwelling irradiance χ at three different depths z_t is exemplarily shown in Figure 26. On the right hand axis of the graphs the corresponding surface shapes are each identified (note: z is positive downward). The top subplot (a) shows the irradiance variability over a x-range of 1 m length at a depth of 1 m. The run of the curve is similar to observed irradiance time records e.g. reported by *Dera and*

Stramski [1986] or *You et al.* [2010]. The extreme irradiance pulses exceed the level irradiance by a factor of 6. The direct attribution of the wave shape is not distinguishable in this case. The middle graph (b) displays a 50 m cross section at the reference depth of 25 m. The peak distances between significantly increased irradiance pulses are between 3 and 8 m. With Eq. 19 this corresponds to dominant light fluctuation periods of 1.4 to 2.3 s. This again is consistent with observations at that depth and at the same wind speed (of 11 m s^{-1}) published by *Hieronymi and Macke* [2010]. The underlying wave structure of approx. 2.4 m height and 40 m length (H/L = 0.06) is not clearly mirrored in the radiative profile at that depth. At z_t = 90 m the variations of χ are small, in the range of 0.9 to 1.1 only. But the run of the χ-values evidently reflects the fundamental surface structure. And by the way: at those depths the projection of χ onto a stationary depth z with equal mean irradiance level (which refers to a pressure gauge) yields similar statistical output – and above all – yields comparable fluctuation attributes in terms of amplitudes and frequency. However, the impact of major ocean waves is evident, but certainly hard to measure.

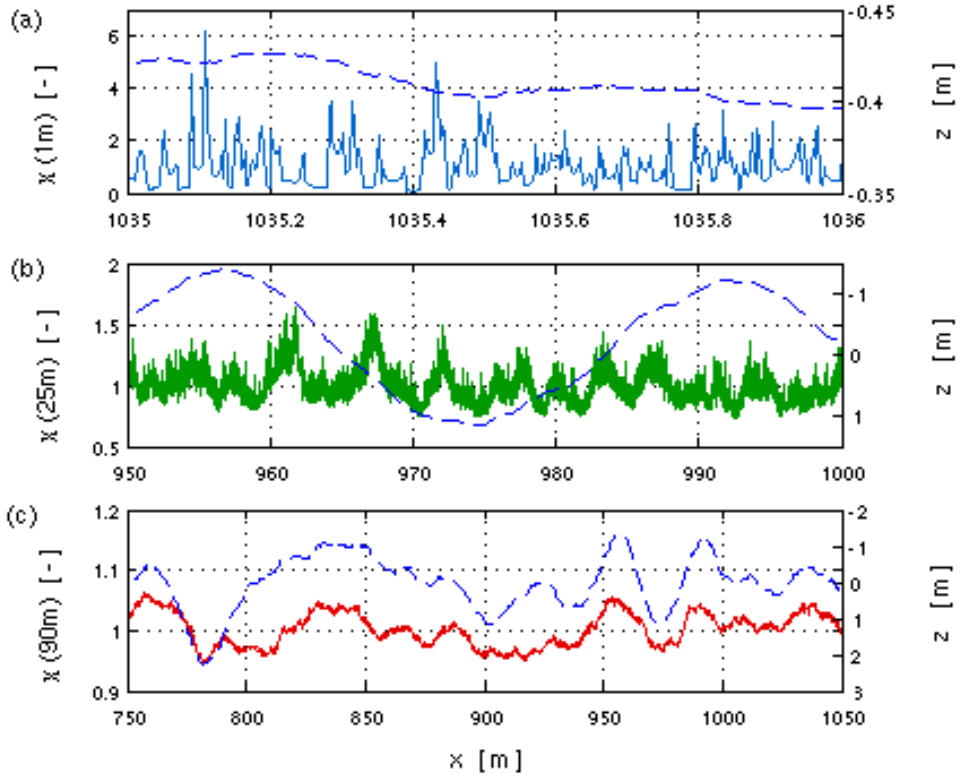

Figure 26. Profiles of normalized downward irradiance χ at different depths z_t (solid lines); on the right ordinate is the corresponding surface elevation (dashed); (a) at 1 m depth with dx = 2.5 mm, (b) 25 m with dx = 1 cm, and (c) 90 m with corresponding detector sizes dx of 10 cm.

In order to characterize the associated wavelength content of the fluctuations, the power spectral density of the modeled signal is computed (Figure 27 left). This is done by using fast *Fourier* transformation (FFT) of the χ-sequences (for every depth and all three model sizes). The maximum of the spectra indicates the dominant distance between two subsequent E_d peaks, e.g. the peak wavelength at 25 m depth is 3.3 m (compare to Figure 26 b). The proximity of the peak length is not always non-

ambiguous. The use of spectral moments provides more stable information (equal procedure as described in Section 2.2.1.4 but for a different parameter). The spectral moment of the order *i* is given by

$$m_i = \int_0^\infty k^i \, S_\chi(k) \, dk \tag{23}$$

where k denotes the wave number (the reciprocal wavelength) and S_χ the spectral density of the signal $\chi\,(x)$. The spectral center of gravity indicates the average distance (wavelength) of all fluctuation components and thus weights the relevant spectral band more. This we call the mean length of fluctuations

$$L_m = \frac{m_0}{m_1}, \tag{24}$$

i.e. the area below the spectrum divided by the first moment. The different magnitudes of the spectra in Figure 27 show the strength of variance at a certain waveband that in total decreases with depth, i.e. the fluctuation amplitudes are very small at 90 m depth compared to depths near the surface.

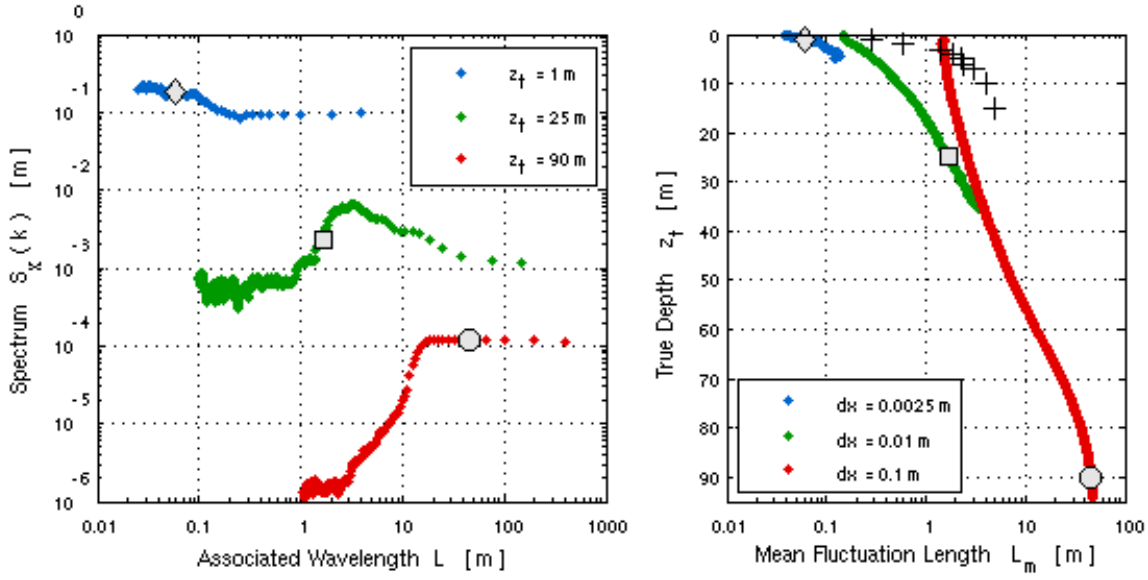

Figure 27. Left: Power spectral density of the three normalized irradiance profiles χ from Figure 26; right: mean fluctuation length L_m of the modeled radiative profiles, the plus signs show observed L_m data as derived from the motion picture analysis (10/30/2009).

The mean length L_m can be seen as grade of the light field blurring. The development of L_m with increasing water depth is shown in Figure 27 right. The gray symbols (diamond, square and circle) point out the location of the mean length of the three example depths with corresponding grid resolution. In general, the mean fluctuation length increases with increasing depth. The three model sizes yield different fluctuation characteristics due to the different spatial resolutions. For comparison we inserted measured values of the mean fluctuation length into the figure (plus signs). The data are estimated from the mean fluctuation period (Eq. 19) that is derived from motion picture analysis of spatiotemporal light field fluctuations at defined depths (same external conditions at the 10/30/2009). The procedure is described in Section 2.2.1.4. Basically

high-frequency fluctuations are more weighted in the model than actually observed. In reality single light beams (from the capillary-small gravity wave transmission range) are less often well-pronounced, and the light fields are more clustered and blurred. An explanation for this must be the potentially insufficient representation of the irregular wave profile in the model; the real surface is much more roughened by the relative strong wind, and thus choppy waves cause nonlinearities at the surface. Moreover whitecaps and bubbles near the surface damp the lensing efficiency of the surface [e.g. *Stramski and Tegowski,* 2001]. The model strictly depends on the accuracy of the sea surface that is implemented. The proposed approach yields much better correlation at sea states with moderate wind (not shown here). However, accordingly to the model we expect that the mean fluctuation length is smaller than 1.5 m (< 1 s period) within the top 5 m, and it extends up to almost 50 m at 100 m depth. The mean wavelength of the irregular wave train itself is close to 56 m. Thus it seems that the light field fluctuations adjust more and more to the dominant waves of the sea state. This statement is supported by spatial and temporal irradiance measurements performed by *Fraser et al.* [1980] or simulations by *Nikolayev et al.* [1972]. The graphs show the principal impact of the corresponding wave band on the subsurface irradiance oscillation. Local wind with short fetch affects the light field down to roughly 10 m only, whereas below this threshold depth fully developed ocean gravity waves play the leading part.

Figure 28, 29, and 30 show the probability density functions *PDF* of the simulated downwelling irradiance E_d within one plane meter for each of the three model domains. The *PDF* color code is logarithmic, with white indicating zero probability (or < 10^{-4}). The *PDF* data show similar features as the three records by *You et al.* [2010] but with high depth discretization (dz = 1 cm, 5 cm, and 10 cm). In the high-resolution model one fluctuation maximum is located between 25 and 50 cm depth, which must be associated with waves of 4 to 60 cm length (ultra-gravity waves). A second maximum is located at 2 to 4 m depth, generated by 20 cm to 3 m waves. Figure 29 shows the *PDF* maximum at a depth of approx. 1 m, while in the model with dx = 10 cm (Figure 30) the fluctuation maximum occurs near 5 m. Thus, the approximation of the fluctuation maximum depends on the spatial grid resolution. The general trend of the probability functions of all model sizes is plausible: initially the fluctuation amplitudes characteristically increase, then decrease gradually with depth [*Snyder and Dera,* 1970], and in the same way the level-mean irradiance decreases exponentially. Obviously, the correct choice of model size and resolution depends on the depth of interest. Near the surface irradiance fluctuations must be recorded with a high spatial resolution of dx = 2.5 mm and a correspondingly high temporal resolution. The model with detector width of 1 cm provides valuable information over most of the area of interest except for the first meter. For depths of interest beyond 20 m the 10 cm model resolution suffices.

The statistical properties of the occurrence of radiative enhancements are quantified by means of a threshold analysis of the normalized downwelling irradiance profiles [e.g. *Dera and Stramski,* 1986; *You et al.,* 2010]. By counting the number of fluctuation amplitudes that exceed the various flash threshold levels χ_{th}, we obtain the frequency of

flashes *N* (normalized per one meter) that exceed the threshold. In each case on the right side of Figure 28, 29, and 30 the frequency of irradiance enhancements is shown with respect to the reference depth. Figure 28 underlines the double maximum of extreme values below the first meter and between 2 and 4 m depth. Largest χ of more than 7 can be found in 25 cm and 2.1 m depth, each associated with different waves. A reason for the comparably moderate χ_{max} is the presence of strong wind (11 m s^{-1}), which impairs the efficiency of generating lens-surfaces for intense focusing. In general, the strongest near-surface fluctuations appear at relatively low wind of less than 6 m s^{-1} as shown in Chapter 2. The fundamental progression of the flash occurrence distributions increases

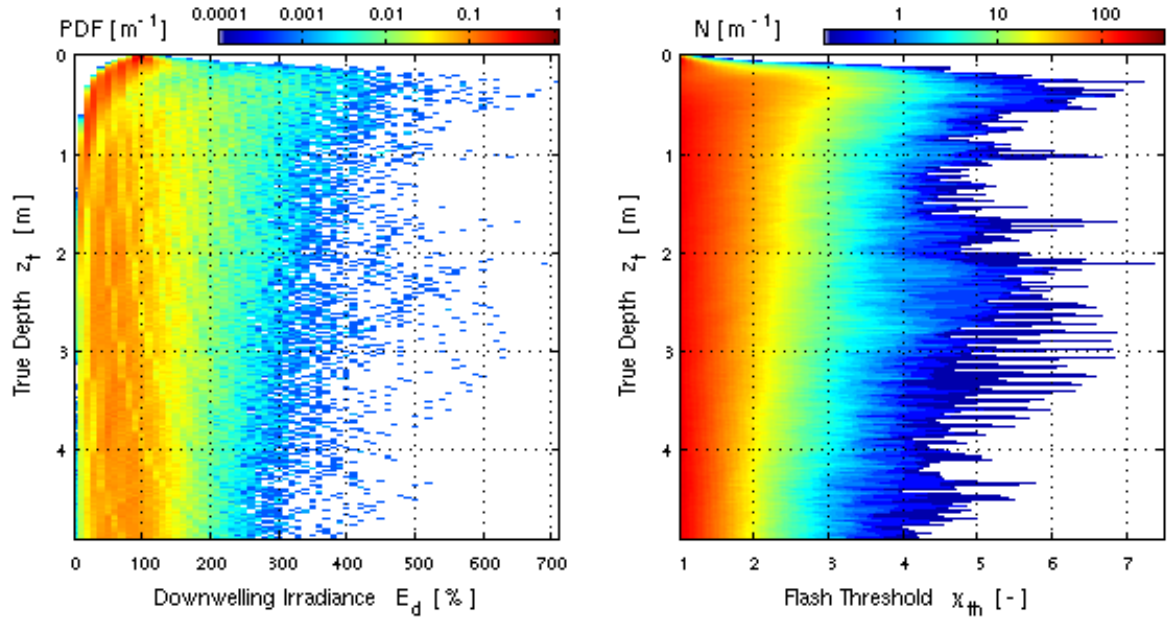

Figure 28. Statistical evaluation of the modeled light field near the surface with dx = 2.5 mm detector width; left: probability density function *PDF* of downwelling irradiance E_d, right: frequency of flashes *N* above a certain flash threshold of normalized irradiance χ_{th} (note: both color scales are logarithmic).

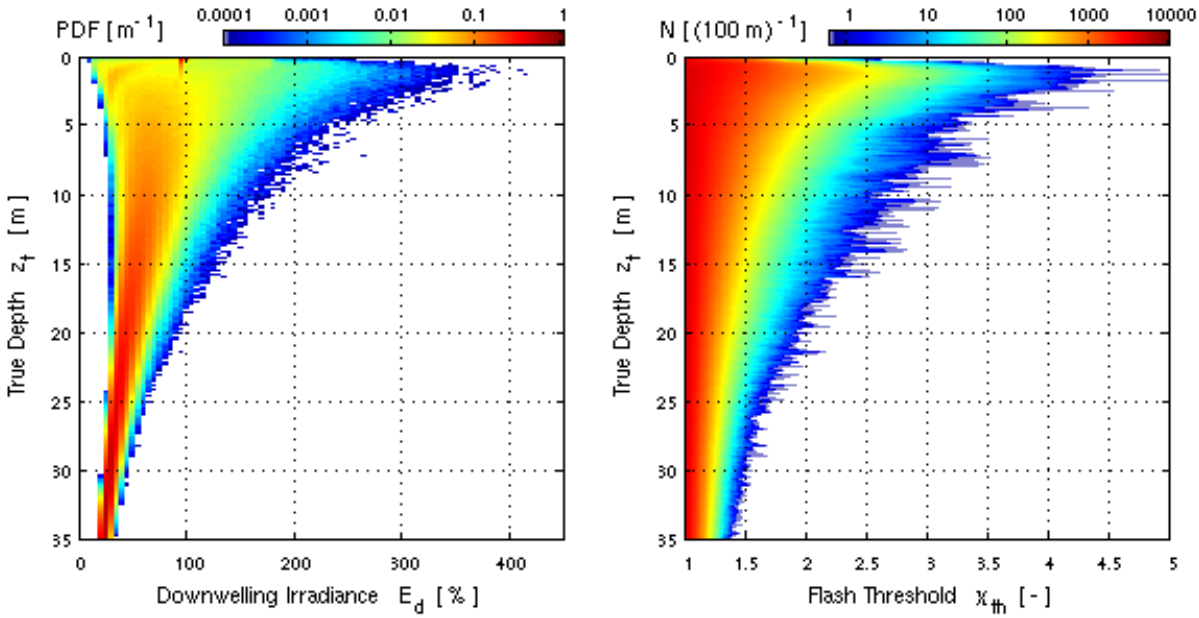

Figure 29. Statistical evaluation of the modeled light field with dx = 1 cm detector width; left: probability density function *PDF* of downwelling irradiance E_d, right: frequency of flashes *N* above a certain flash threshold of normalized irradiance χ_{th} (note: both color scales are logarithmic).

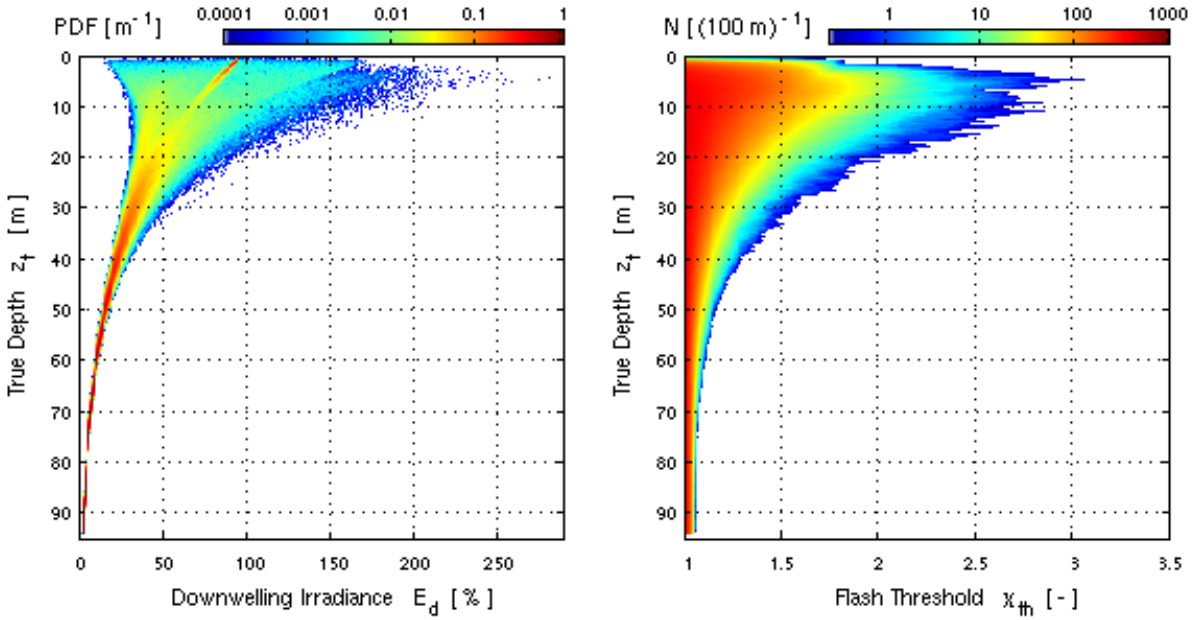

Figure 30. Statistical evaluation of the modeled light field with dx = 10 cm detector width; left: probability density function *PDF* of downwelling irradiance E_d, right: frequency of flashes N above a certain flash threshold of normalized irradiance χ_{th} (note: both color scales are logarithmic).

rapidly within the first 30 cm of the water column and then it decreases slowly. Light flashes of $\chi = 1.5$ occur down to depths of 35 m (Figure 29 and 30) under the given circumstances. In the particular case this enhancement is due to a total wave deflection of approx. 120 m length and almost 3.5 m height; this is a typical swell wave which is independent of local wind.

Some additional statistical aspects of the *PDF* of χ fluctuations with regard to two different model dimensions are presented in Figure 31. The skewness of the irradiance distribution is a measure for the deflection direction of extreme spikes. Above 54 m the E_d distributions are right-skewed, i.e. more short and intense light flashes appear. Below that depth the distribution is slightly negatively skewed. Here, more peaks with irradiance values less than the mean occur. The kurtosis is a measure for the peakedness of the irradiance distribution. Higher positive kurtosis means that a larger part of the variance results from extreme deviations. With increasing depth the distributions become more grouped around the mean value. In principle, all model sizes deliver equivalent results. Deviations may result from the different resolutions dx of 10 and 1 cm, and the different horizontal lengths of the investigated light fields of 400 and 150 m respectively (the high-resolution model is not shown in the graphs). Generally, the depth development of simulated *PDF* skewness and kurtosis are consistent with high-frequency irradiance measurements by *You et al.* [2010] or *Gernez et al.* [2011].

The most cited quantity for describing underwater light fluctuations is the coefficient of variation *CV* [e.g. *Nikolayev and Khulapov* [1976]; *Gernez and Antoine,* 2009; *Hieronymi and Macke,* 2010; *D'Alimonte et al.,* 2010; *Weber* [2010]]. The simulated change of *CV* along the water column is shown in Figure 32. The gray shades symbolize the three model dimensions. The curve processions again show the depth range validity

of the models that we just discussed. The figure shows that underwater light field fluctuations occur even in 100 m depth (at the specified irregular wave profile). Here, *CV* is still about 3 %. However, wave-induced light fluctuations depend on local wind and the peculiarity of the sea state. *Weber* [2010] shows the theoretical wind dependency of *CV* with water depth. According to this study *CV* exhibits a bimodal dependence of the depth, with a near-surface *CV* maximum that shifts towards smaller depths with increasing wind velocity. The unique influences of local wind and especially the development of the sea state have to be subject to further analysis; an approach is shown in Section 5.1.

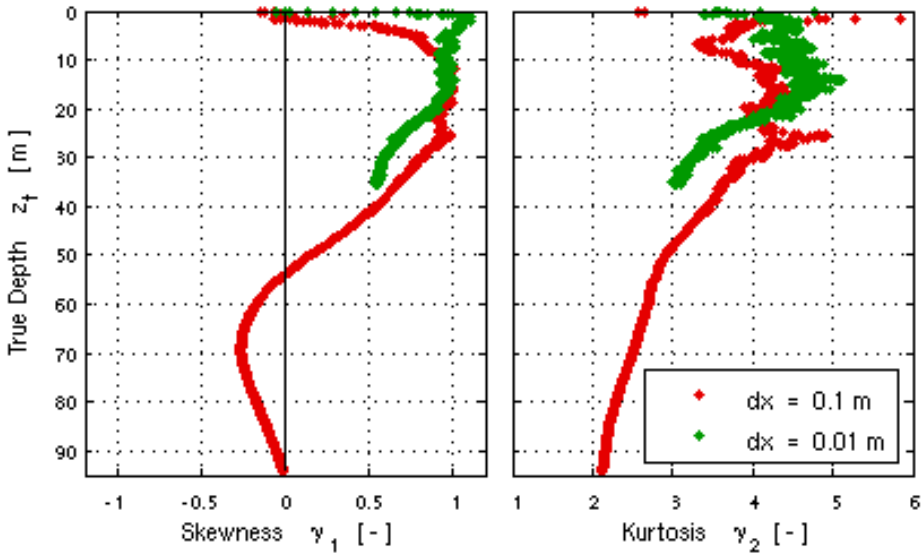

Figure 31. Statistical evaluation of the probability density functions *PDF* of the modeled light field with two detector sizes *dx*; left: skewness of the irradiance distributions at depth; right: kurtosis of the same distributions.

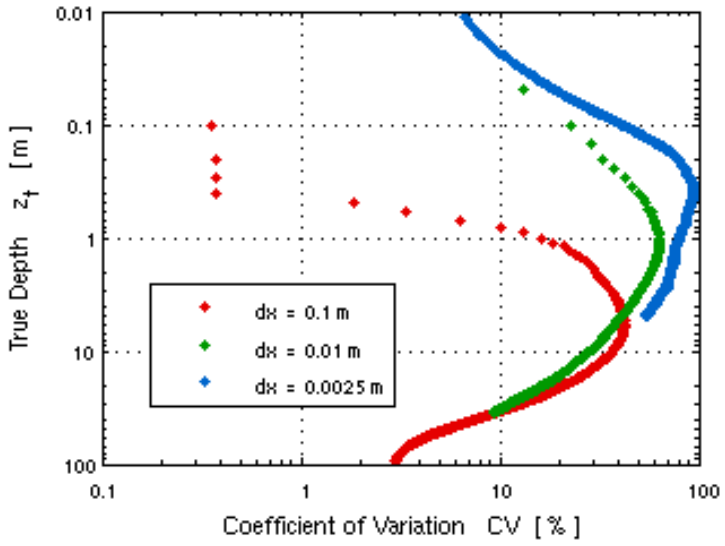

Figure 32. Change of the coefficient of variation *CV* of light fluctuations with water depth z_t and in accordance with grid resolution *dx*.

4.2.3 Comparison of model and measurements

The specific irregular sea surface has been chosen for comparisons between the modeled and observed irradiances (Section 2.3). The observed E_d data that are shown in Figure 33 correspond to the wavelength 489 nm (the model refers to 490 nm). The sun zenith angle was at approx. 30° during the measurements. The records were conducted in a way to minimize the ship perturbation onto the light field [*Gordon*, 1985]. In-situ measurements of the water properties reveal a mean chlorophyll concentration of approx. 0.1 mg m^{-3}. The fully developed sea state indicates that the upper layer is well mixed and non-stratified. The data mean values include measurements within ± 0.3 m depth range (round 80 values per depth). The modeled minimum and maximum E_d values per depth outline the range of fluctuations for two models with dx = 10 cm and 1 cm, respectively. The dark red curve marks the total diffuse downward irradiance with respect to 10 cm resolution.

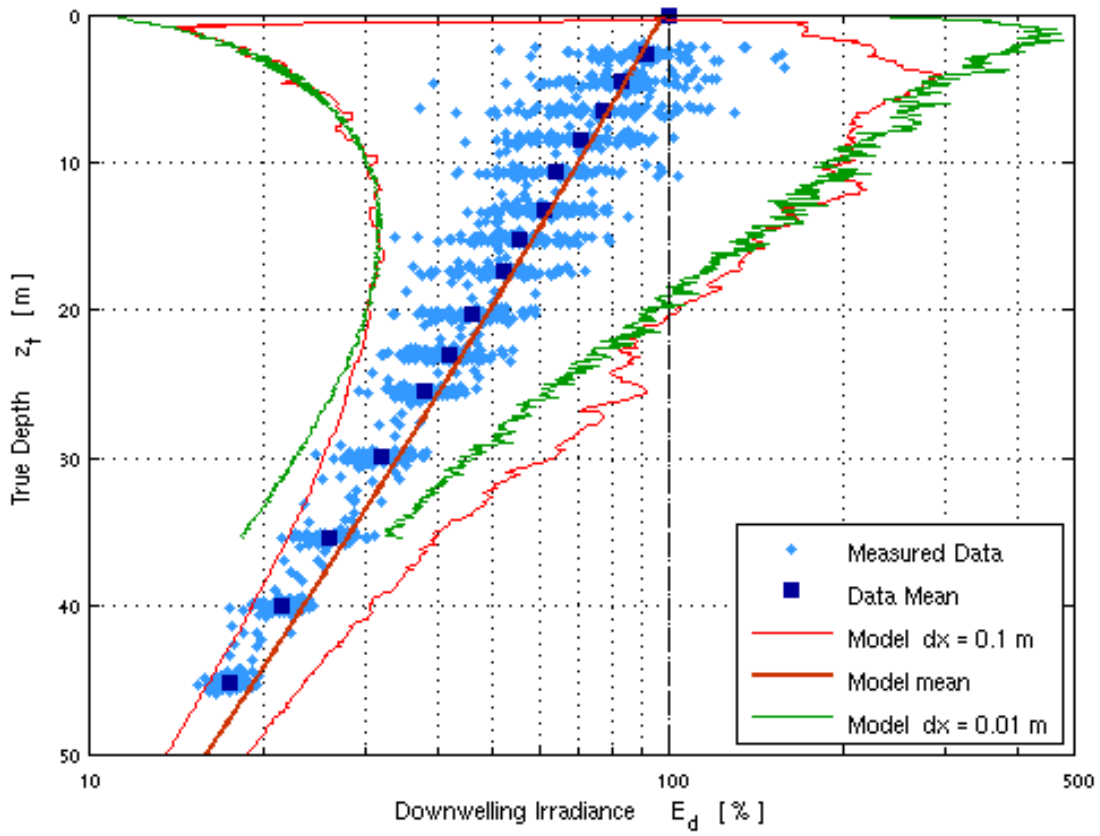

Figure 33. Comparison of downwelling irradiances E_d as calculated by the model (for λ = 490 nm) vs. offshore measurements with the spectral radiometer at 489 nm (10/30/2009). The blue points show the measured data with corresponding squares which indicate the averaged total E_d at the depth level z_t. The red lines show the model results of mean values, minimum, and maximum respectively with dx = 10 cm. The green graphs show the minimum and maximum range of modeled fluctuations with 1 cm horizontal resolution.

The measurement data show light flashes (χ = 1.5) down to 15 m depth. According to the model, light flashes could be possible town to 35 m depth. The percent relative difference ε (Eq. 17) of E_d mean values of measurement and simulation varies from + 2.7 to - 8.2 % (from the surface to 45 m depth) in case of the 10 cm resolution model. With

dx = 1 cm, the relative difference is 1.9 to 13.5 % (down to 35 m depth). The depth-integrating root mean square error *RMSE* (Eq. 18) is 4.5 % down to a depth of 35 m with *dx* = 10 cm. For the second higher resolution *RMSE* is 5.1 % at the same depth.

Concerning all uncertainties in the data acquisition, e.g. the determination of the water's inherent optical properties, synoptical imponderables, the sensor accuracy, or possible perturbation due to the vessel's hull, the overall agreement between averaged observations and the idealized modeling results appears satisfying.

In addition to the radiative measurements we took motion pictures of underwater light pattern as described in Chapter 2. Figure 34 shows a typical spatial light pattern that is taken at 1 m water depth. The pixel gray-value intensity is converted to comparable values of the normalized downwelling irradiance χ, whose distribution follows the measurements and the calculated probability density. Assuming a linear relation between pixel brightness and irradiance this picture provides a good approximation of the true χ-distribution. The white color contours the mean adapted irradiance. Red stands for enhancements beyond 3. The reference grid marks 10 cm distances. The graph below shows a sequence of the modeled χ at the same depth. The modeled graph and any linear image section agree well. From this we follow that the

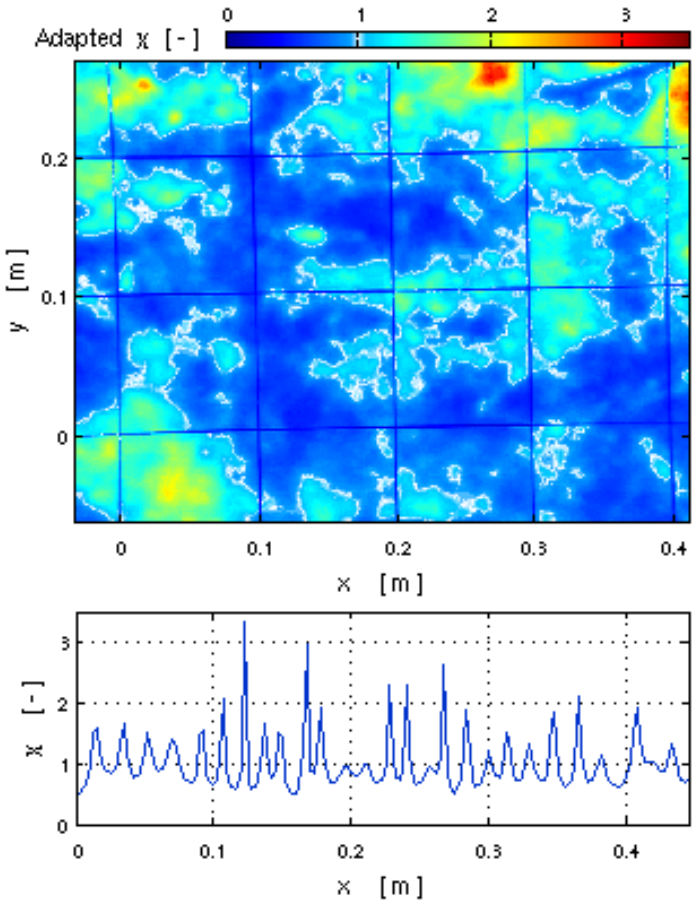

Figure 34. Spatial pattern of a real light field at 1 m depth (from 10/30/2009) with adapted radiation parameter χ; below: simulated random profile of χ at the same depth with *dx* = 2.5 mm.

extreme values are well represented and that the probability density distributions are in the same order of magnitude. The periodicity of modeled light fluctuations must be considered critical because it tends to overestimate the high-frequency part of the spectrum, which is due to the specific surface shape (discussed above and in Figure 27). The applied wave profile which accounts for capillary to swell waves is the most developed water surface representation that is previously released in the context of subsurface radiative transfer simulations [e.g. *D'Alimonte et al.*, 2010; *You et al.*, 2010]; nevertheless there is still scope for model improvements concerning this issue, e.g. the implementation of hydrodynamical nonlinearities.

4.3 Conclusions of the irradiance fluctuation simulations

We developed a hybrid radiative transfer model for simulating high-resolving E_d fluctuations along the water column that are caused by surface waves. The underwater propagation of solar radiation is calculated by means of a Monte Carlo radiative transfer procedure (as described in Chapter 3 of this thesis). The model is generally adaptive for several variables, such as the electromagnetic wavelength, inherent optical properties of sea water (in terms of chlorophyll content), the sun position, the diffuseness of the atmosphere, the depth and size resolution of interest, and for arbitrary sea surface structures. Accounting for the latter is the main advantage and purpose of the model. Elevations of complex sea surfaces can be implemented into the model. The model provides information about the fluctuating radiation field down to water depths of 100 m with very high vertical and horizontal resolutions. The model parameters are selected in such a manner that maximum light field variability can be achieved, i.e. very clear water and high sun altitude is used for the calculations.

One aim of this study is to show the potential influence of different single regular waves with emphasis on the correct hydrodynamic representation of their nonlinear shape. Different wave types have characteristic impact on underwater light fluctuations in defined depths. Capillary waves of lengths < 1.7 cm produce focal planes within the first meter near the surface with comparable small radiative enhancements. At 1 m water depth more intense light fluctuations arise from ultra-gravity waves with lengths of 10 cm to 1 m. An irradiance pulse can (theoretically) exceed the mean irradiance by a factor of 40 at that depth with respect to a 2.5 mm wide sensor. Ordinary gravity waves of lengths between 1 and 10 m cause most fluctuations at 10 m water depth. The longer the wave the deeper is its potential. Even 200 m long swell waves can develop small irradiance enhancement below 90 m of water depth.

Another objective of this work was to clarify the interference of the light field through various superposed wave types on different scales. For this purpose we implemented an irregular wave profile into the model that accounts for certain open sea conditions. Near the surface waves of around 2 cm length (transition range of capillary to ultra-gravity waves), which are closely associated with local wind, build up clear single stripes of E_d

enhancements. These single rays are further deflected by overlaying waves of 0.1 to 1 m length which leads to intensified light beam grouping at depths of 1 to 4 m and causes the most intense light fluctuations. Underwater light flashes, that exceed the mean irradiance by a factor of 1.5, occur down to depths of 35 m under the same conditions. This enhancement is due to a total wave deflection of 120 m length and 3.5 m height; this is a typical swell wave (of 9 s wave period) which is independent of local wind. Even in 100 m depth slight wave-induced light field variance was found. We conclude that local wind affects the light field variability down to roughly 10 m only, whereas fully developed ocean waves dominate the light field below this layer. Light field fluctuations adapt with increasing water depth to the sea state conditions at the surface.

The model results are in agreement with radiometric measurements that are taken under high sea conditions. Also the spatial structures of modeled light variability essentially meet the observations, for example in terms of their occurrence probability. Our model provides details about the scales of radiative fluctuations along almost the entire lit water column, which is far beyond the information content of standard in-situ measurements.

In conclusion, it is to recommend that light fluctuations in the ocean are rather characterized by three sea state parameters: peak period, significant wave height, and wind speed, than by the wind velocity alone. Local wind definitely causes the most intense radiative variations within the first ten meters, and it is a certain proxy value of fluctuations in greater depths. However high seas are often dominated by wave systems that are independent of local winds (with short fetch), but those larger waves strongly influence the deeper light field.

5 Newly raised research questions and perspectives

5.1 The significance of the sea state

In this dissertation, I examined the light field below one particular sea state only, in order to show the principle performance of the radiative transfer model (Section 4.2.2). The specific irregular wave system was selected, because comparative radiometric data with equal conditions were available. Nevertheless, there is scope of future scientific works concerning the characteristic influences of different sea states. An interesting question is raised about the validity of using wind speed as a light field determining feature only instead of regarding the development level of the sea state as well. The issue is discussed with the help of the following three examples.

We have equal local wind conditions of v_w = 5 m s^{-1}. Three situations are considered: a young sea (short fetch, comparable with the Bay of Kiel, with H_s = 0.1 m and T_0 = 1 s), a fully developed wind sea (with H_s = 0.7 m and T_0 = 4 s), and a fully developed wind sea that is superposed on an (admittedly very steep) swell with H_s = 4 m and T_0 = 8 s. The fundamental short and long wave spectra are described in *Elfouhaily et al.* [1997], applying the *Pierson-Moskowitz* spectrum for long waves with the *JONSWAP* peak enhancement as introduced by *Hasselmann et al.* [1973]. From the spectra, three in-phase wave profiles are derived by applying linear wave theory [e.g. *Kinsman*, 1965]. Figure 35 left shows a 200 m section of the profiles with horizontal resolution of 0.1 mm. The spectral sea state characteristics are well represented. If we now look at the wave slope distributions of the three sea states (right), we see clear differences. In addition, I plotted the *Cox-Munk* slope distribution (dashed) for the same wind speed of 5 m s^{-1} [*Cox and Munk*, 1956]. The *Cox-Munk* statistical distribution of sea surface slopes, fitted to a *Gram-Charlier* series, is derived from photographs of the sun-glitter on the sea surface. It is located between the young sea and the fully developed wind sea. The skewness of the *PDF* is more pronounced at stronger winds. The *PDFs* in Figure 35 right show strong distinctions. The distributions imply that the steeper and the higher the wave systems is, the more often relative large wave slopes do occur. This seems to be logical, although for instance *Heron et al.* [2006] stated that the long wave part of the spectrum (waves > 4 m) contribute very little to the mean-square slope. Obviously, there are some differences in the deduced *PDFs*. Anyway, the proposed approach of generating realistic sea surfaces should be critically reviewed by considering nonlinearities of the surface as parasitic capillary waves [e.g. *Longuet-Higgins*, 1963; *Longuet-Higgins*, 1982], or e.g. by considering wave-wave interactions of second order [*Forristall*, 2000].

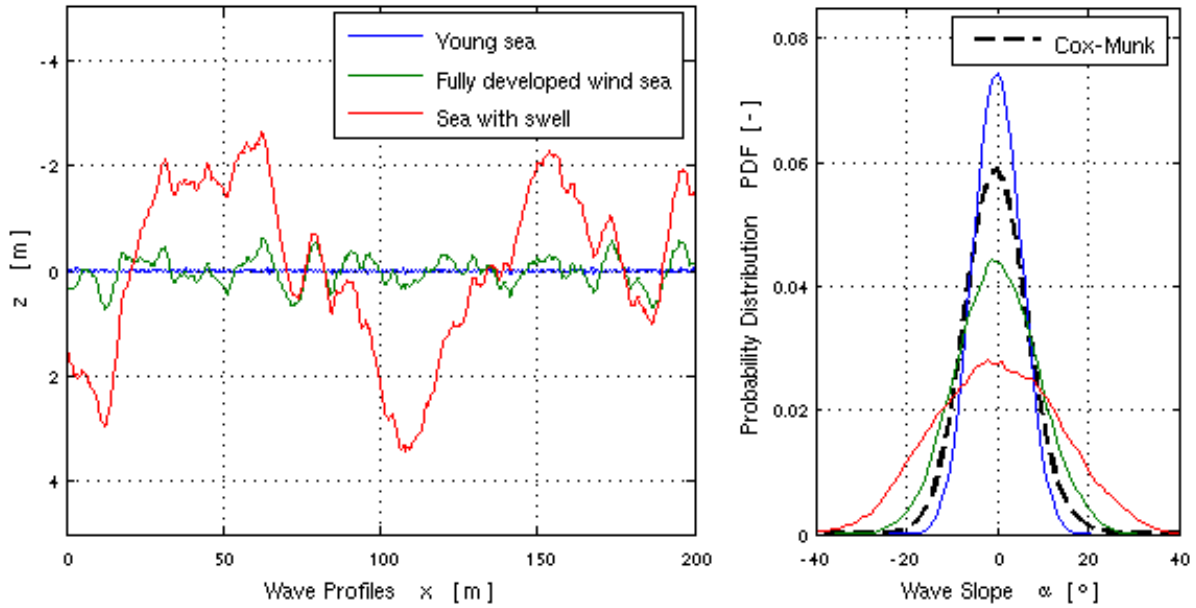

Figure 35. Left: modeled irregular sea surface profiles at different levels of sea state development, all at the same wind speed of v_w = 5 m s^{-1} (all with equal phase position); right: corresponding probability distribution *PDF* for wave slopes α, additionally inserted is the equivalent parameterized distribution as introduced by *Cox and Munk* [1956].

However, the proposed wave profiles are the most advanced in the context of oceanic radiative transfer simulations, e.g. compared to *Zaneveld et al.* [2001], *Deckert and Michael* [2006], *D'Alimonte et al.* [2010], or *You et al.* [2010], since all ocean wave types (from very small local wind waves to very long swell waves) are considered with high resolution of the wave profile. Figure 36 shows the resulting subsurface light fields below the three proposed waves from Figure 35. The subplots on the left hand side (a, c, and e) are simulated using the 10 cm resolution model down to 100 m depth, the pictures on the right (b, d, and f) correspond to the high-resolution 2.5 mm model. The external conditions are the same (Table 4).

With regards to the 10 cm model, distinct differences appear below 30 m; here, long waves and especially the swell wave develop enormous deep-water E_d variability. Figure 37 illustrates the corresponding differences of irradiance characteristics in terms of flash frequency distribution between the young sea and the swell-superposed sea state (compare to Figure 28 and 30). The green lines indicate the simulated maximum radiative enhancement per depth. Light flashes (χ = 1.5) occur down to remarkable 35 m at a young sea, whereas in case of the swell-superposed sea, light flashes arise down to 45 m depth. At 90 m water depth, χ_{max} equals 1.04 and 1.16, at young and swell sea respectively. This is up to 16 % radiative enhancement at that depth. Thereby, it is remarkable that the averaged irradiance per depth is almost identical at both surface illumination conditions (shown in Figure 38).

With regards to the high-resolution model, the major irradiance characteristics within the near-surface region are similar. This is comprehensible and documented in Chapter 4. Here, the light variability is driven by local wind (basically 2 to 10 cm long waves) which is the same in the examples. Evident ray-direction differences appear in

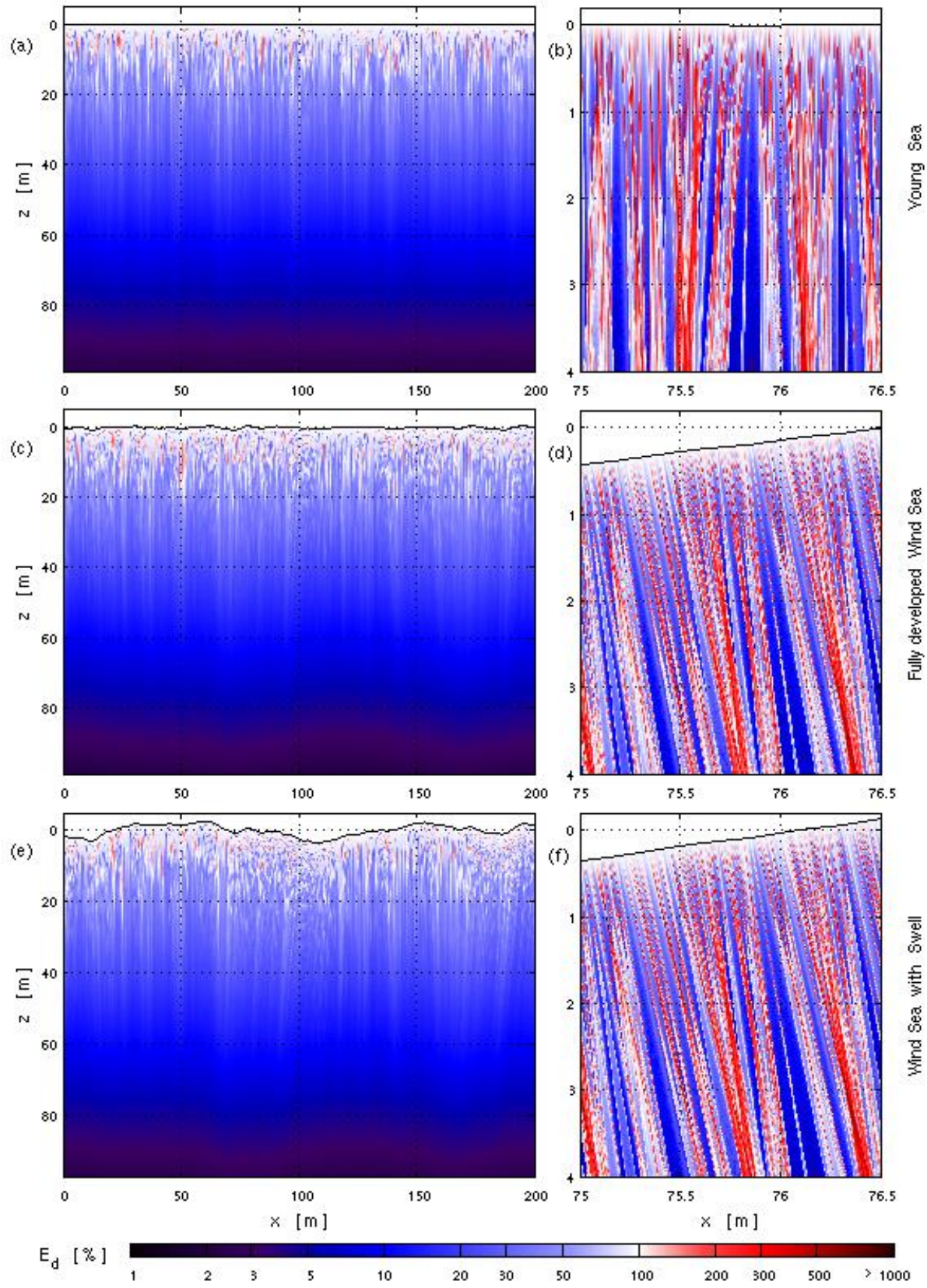

Figure 36. Spatial light fields below irregular wave trains at same wind speed of 5 m s^{-1} but with different levels of sea state development; left: model with *dx* = 10 cm resolution, and right: near-surface detail with 2.5 mm resolution.

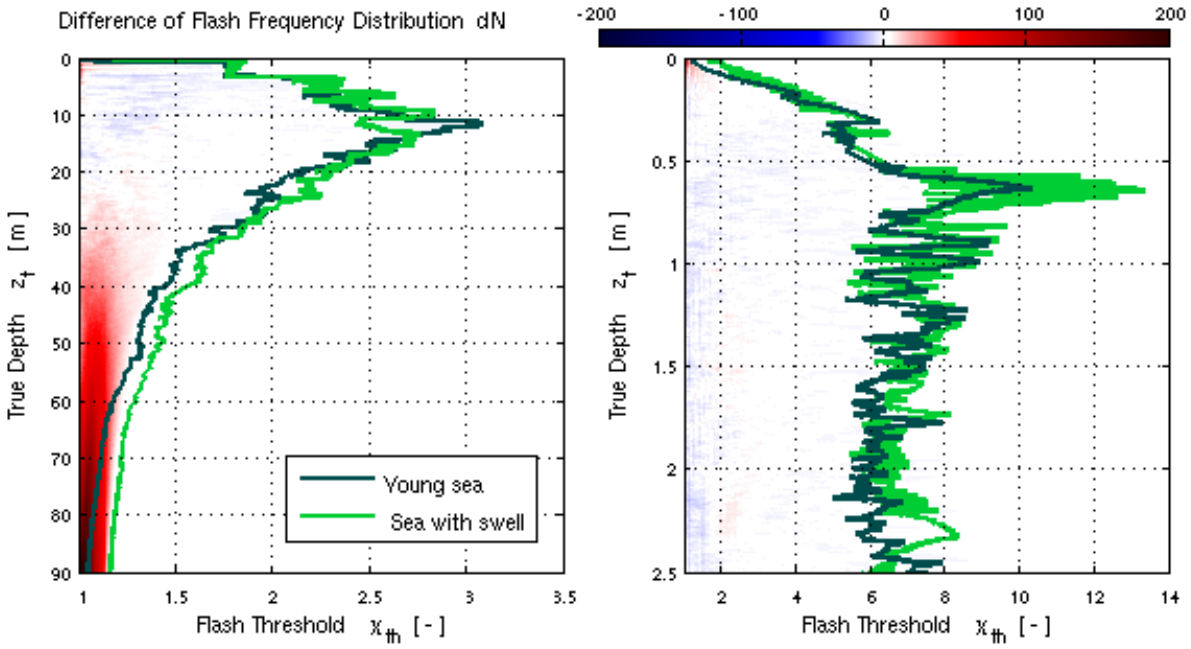

Figure 37. Difference between two stages of sea state development at same local wind conditions (sea with swell minus young sea); left: difference of flash frequencies per water depth z_t which exceed a certain flash threshold χ_{th} with the 10 cm model, right: the same for the top layer with the 2.5 mm resolution. The green curves show the equivalent maximum contours of the flash distributions (compare to Figure 28 and 30).

cases with high and steep superposed waves (Figure 36 f). This again proves the practicability of the consideration of the actual sea surface elevation (discussed in Sections 4.1.5, and 4.2.2). The *PDFs* of young sea and swell-superposed sea are almost identical, flash frequency differences are negligible within this zone (Figure 37 right). The maximum radiative enhancement χ_{max} is up to 13 at a depth of approx. 0.7 m. This is some more than at stronger wind, as shown in the Section 4 example, where χ_{max} = 7, but in the same order of measured maximum values (see Figure 24 and the associated text passage).

The given examples underline the importance of the consideration of the actual sea state. The long wave part of the sea spectrum mainly contributes to the deep-water light variability. This issue should be addressed in future works.

Another point, which is of potential importance, is the sea state influence on the total downwelling irradiance. Classical radiative transfer models as for instance *Hydrolight* use the wind speed to determine the total E_d per depth. Generally, the slope *PDF* follows the parameterization of *Cox and Munk* [1954] depending on wind speed. Let us assume the correctness of the introduced *PDFs* for different sea states (Figure 35 right). This means that, in terms of the shape of the *PDF*, a more developed sea has similar impact as increased local wind. Thus, the *PDF* of the swell-superposed sea with local wind speed of 5 m s^{-1} (red line) looks similar to the *Cox-Munk* distribution that we obtain at approx. 15 m s^{-1} (ignoring the increased *PDF* skewness). Since we know that swell and fully developed wave systems are mostly present at the open ocean (see wave climatology Figure 2), the usage of wind speed as characterizing light field parameter is put into question.

At high sun positions, this matter is irrelevant. Figure 38 shows the total downwelling irradiance as a function of water depth with respect to the different levels of sea state development. At high sun, the curves run almost identically. Most of the transmitted radiation is refracted with small angles only. The same is true in the context of irradiance reflectance at high sun positions. The surface albedo is independent of wind speed; in this case about 98 % of the radiation is transmitted into the water body [*Preisendorfer and Mobley*, 1985]. At low sun positions, there are significant variations of the albedo with changing wind speed. The reflectance is between 100 % without wind, and 25 % at 20 m s^{-1}. That transfers to the underwater light field. At lower sun positions, the total downwelling irradiance is generally decreased due to increased wind, which must be seen with respect to the probability density of single slopes. Or to get back to the development levels of seas, the more the wave system is developed (at steady wind), the smaller is the total irradiance along the water column. The root mean square error (Eq. 18) down to 90 m between *Cox-Munk* and the three given examples is always < 0.4 % at high sun (θ = 0°). But for lower sun (θ = 70°), *RMSE* equals 3.05 % for the young sea, 5.22 % for the fully developed sea, and 20.44 % with swell.

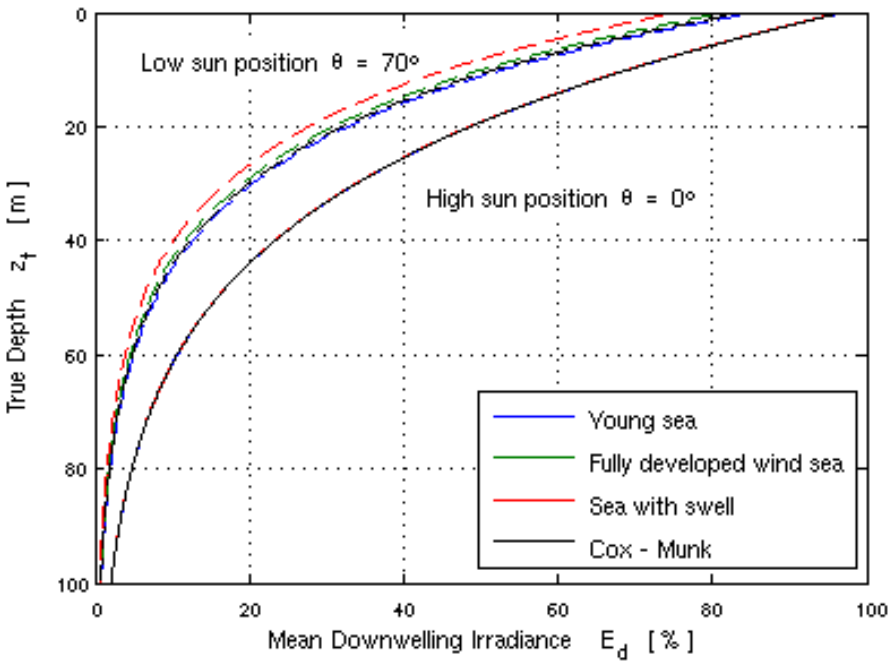

Figure 38. Total downwelling irradiance E_d against water depth z_t; the solid lines stand for sun zenith (all lines lie on top of each other), and the dashed lines represent relative low sun with $\vartheta = 70°$, each as a function of the sea state and compared to the *Cox-Munk* parameterization.

The above considerations suggest that sea states in general have important influence on light field variability and on the total downwelling irradiance per depth. The usage of local wind speed, as light field determinant factor, may result in significant misinterpretations. The potential bias can be in the order of up to 20 % *RMSE*, as shown above. Thus, there is some demand for further in-detail studies.

5.2 Surface illumination

Different spectral wave bands may be of interest concerning light field fluctuations. We have seen that for instance ultraviolet-A and -B radiation penetrates relatively deep compared to e.g. red light (Figure 11). Thus, intense radiative enhancements due to the wave lensing effect may appear near the surface, as for example shown by *Deckert and Michael* [2006]. The here introduced radiative transfer model is generally utilizable for different wavelengths. As the case may be, scattering and absorption properties must be adapted. So far, the model's ability to calculate the radiative transfer of other wavelengths than 490 nm is unproven jet.

The same is valid for changing sun positions. In principle, light fields with variable sun zenith angles (e.g. a diurnal circle) can be simulated. So far, I always used $\theta = 0°$, because with this maximum light field variability and deepest light penetration into water can be achieved. Nevertheless, sun at zenith is a rather academic case, e.g. the highest possible sun position in Kiel is approx. $\theta = 30°$.

Clouds and other different atmospheric conditions (e.g. dust, or increased daylight diffuseness) are not considered either. I showed one comparison between total overcast and clear sky conditions by means of a single wave (Section 4.2.1, Figure 22). There are great differences due to changing surface illumination. This subject can be researched with the given data base, for instance by looking on the interactions within the light field beneath an irregular sea surface.

5.3 Properties of the water body

Another point of interest is the particle distribution within the water column. Within this thesis, water properties are assumed to be homogeneous and non-stratified. This assumption may be the case for a top ocean layer where water masses are often well-mixed. Figure 39 shows observed chlorophyll and temperature profiles (*ANT-XXIV/4*). Chlorophyll can be found at depths with sufficient light and nutrients. The half of the primary production is generated at depths above 40 m [*Siegel et al.*, 1995]. But at the open sea, where in general much less bio mass exists compared to the shelf regions, phytoplankton remains much deeper (e.g. the blue line's maximum is at 140 m depth). Often very thin phytoplankton layers are present, ranging in thickness from a few centimeters to a few meters [*Dekshenieks et al.*, 2001]. They may extend horizontally for kilometers and persist for days. The thin layer's depth is closely associated with depth and strength of the pycnocline (a rapid density change in the water column that is affected by temperature and salinity changes, see Figure 39 right). Especially for those layers, the proven deeper-water irradiance enhancements due to larger waves might be of vital interest. That biological aspect should be further researched.

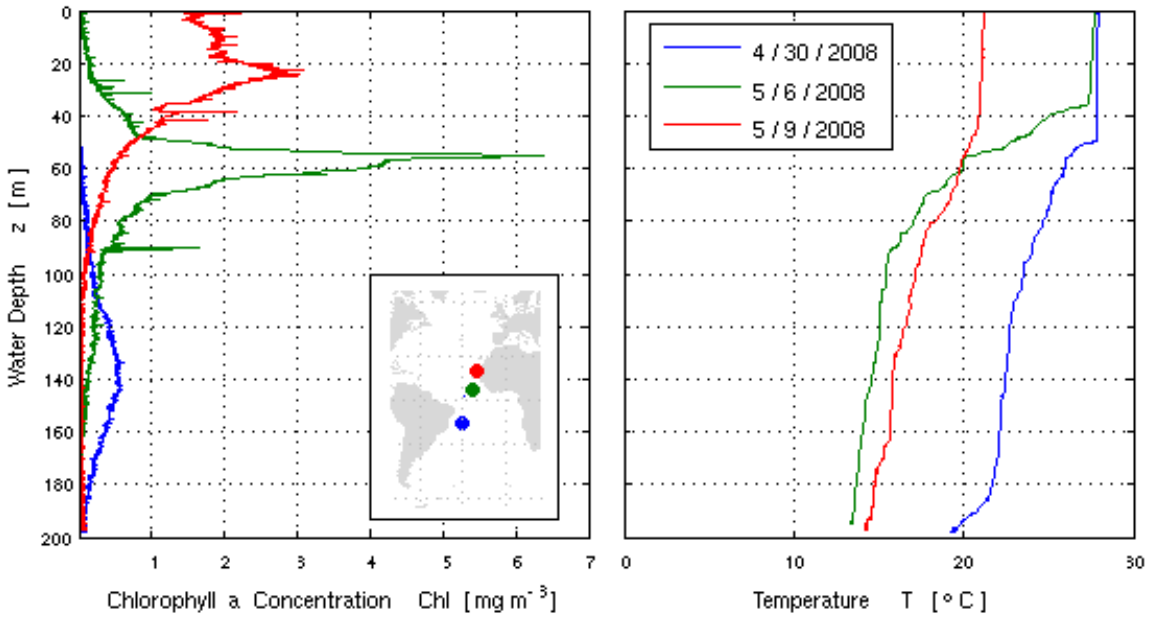

Figure 39. Left: typical chlorophyll *Chl* profiles along the water column, right: corresponding temperature profiles. The data are provided by *B. Schmitt* from *AWI* (10/22/2008), showing measurements from the RV *Polarstern ANT-XXIV/4*.

The upper ocean layer is a highly dynamic medium. Due to surface wave propagation particles within the water column move on orbital paths. The radii of the circular motions decrease with increasing water depth [e.g. *Kinsman*, 1965]. Particles, e.g. phytoplankton, and hydrosols, are affected by considerable hydrodynamic accelerations that promote preferences of the particles orientation along the orbital path. Another point is the horizontal particle orientation on larger scales. Numerous cyclonic spiral eddies with a scale of 10 km are very often observed at the ocean's surface [e.g. *Eldevik and Dysthe*, 2002]. Figure 40 illustrates these spiral eddies, where particles obviously have predominant orientations. After processing satellite true color images by means of chlorophyll retrievals, detailed structures can be observed. The image shows different densities, communities, and depth distributions of phytoplankton. Just recently, *Marcos et al.* [2011] demonstrated that the swirl patterns arise when elongated microorganisms align preferentially in the direction of the fluid flow, and thus they essentially alter the light scattering properties of seawater.

Moreover, the scattering properties of near-surface water layers are affected by air bubbles [e.g. *Stramski and Tegowski*, 2001]. In particular at stronger wind, waves break and whitecaps develop. Thereby, bubble populations enter into the mixed layer, which change the medium's volume scattering phase function. Larger bubbles contribute strongly to scattering at large angles with serious effects on remote sensing of the ocean color [*Zhang et al.*, 2002].

Specifics of particle alignment, plankton community, air bubbles, or hydrosol size distribution are not taken into account within this thesis. In this sense, the water body is treated to be well mixed. The utilized phase function by *Petzold* [1972] considers typical marine particle concentrations with both, highly scattering and highly absorbing cases. In Chapter 2, I have shown how light propagates in different aquatic media. In principle,

the model could be adapted to water stratifications with different scattering properties. But that was actually not the sense of this radiative transfer model. The motivation was to investigate the mechanisms of wave-induced light fluctuations. For this reason, clear homogeneous well-mixed water was chosen.

Figure 40. *Aqua-MODIS* picture of the Barents Sea (collected 08/31/2010). The water is turquoise brightened by blooms of coccolithophores. The color variations reflect the differences in phytoplankton community composition and depth distribution [*Signorini and McClain*, 2009]. The image section covers an area of approx. 300 km x 200 km (37°E – 43°E, 67.5°N – 69.5°N). The image is from the NASA ocean color web page[8].

5.4 Biogeochemical questions

One major finding of the radiative transfer modeling is the existence of extreme light flashes far beyond 5 times the average irradiance at a depth. Only recently, light flashes with $\chi > 10$ were observed by the group of *D. Stramski* at *Scripps* [*Gernez et al.*, 2011]. My results show theoretically possible radiative enhancements of $\chi > 40$ at 1 m water depth (with dx = 2.5 mm), and still $\chi > 1.5$ even at 30 m depth (with dx = 1 cm and 10 cm). These values are remarkable more than generally assumed regarding light fluctuations and its responses to different biogeochemical questions. At least, this is an estimate on the theoretical upper limit of underwater light intensity at 490 nm down to 100 m depth. This matter concerns e.g. photo-inhibition of photosynthesis processes [e.g. *Long et al.*, 1994]. As stated before, extreme near-surface radiative enhancements can also appear at the ultraviolent-A and -B spectral ranges. *UVA* and *UVB* irradiance peaks may cause an oversupply of usable radiation for planktonic particles, and may induce *DNA* damage or increase the plankton mortality rate within the top meters [e.g. *Davidson*,

[8] NASA ocean color web page: http://oceancolor.gsfc.nasa.gov/cgi/image_achive.cgi?c=CHLOROPHYLL

1998]. From this perspective, this could be a reason for comparable less phytoplankton within the top 5 m layer; the maximum chlorophyll concentration is normally somewhat deeper (see Figure 39).

Abbreviations

DNA	*Deoxyribonucleic acid* – contains the genetic instructions used in the development and functioning of living organisms
ERA-40	*European Centre for Medium-Range Weather Forecast re-analysis* of the global atmosphere and surface conditions for 45 years (1957-2002)
FFT	*Fast Fourier Transform*
HL	*Hydrolight* – Radiative transfer software
IOP	*Inherent Optical Properties* – scattering, absorption and beam attenuation properties of a medium
JONSWAP	*Joint North Sea Wave Observation Project*
MC	*Monte-Carlo* method – computational algorithm
MODIS	*Moderate-resolution Imaging Spectroradiometer* – is a scientific instrument on board the *Aqua* satellite
PAR	*Phytosynthetically Active Radiation* – spectral range of 400 to 700 nm
RGB	*Red*, *Green*, and *Blue* color model for representation of images
TOA	*Top of Atmosphere*
UVA	*Ultraviolet-A* spectral range of 315 to 400 nm
UVB	*Ultraviolet-B* spectral range of 280 to 315 nm
VIS	*Visible* spectral range of 390 to 750 nm

Nomenclature

Symbol	Unit	Description
a	[m^{-1}]	Total absorption coefficient
a_p	[m^{-1}]	Particle absorption coefficient
a_w	[m^{-1}]	Seawater absorption coefficient
a_y	[m^{-1}]	Absorption coefficient of dissolved organic (yellow) matter
b	[m^{-1}]	Total scattering coefficient
b_p	[m^{-1}]	Particle scattering coefficient
b_w	[m^{-1}]	Seawater scattering coefficient
c	[m^{-1}]	Total attenuation coefficient
c_p	[m^{-1}]	Particle attenuation coefficient
dx	[m]	Horizontal detector width
dz	[m]	Depth discretization
f	[Hz]	Frequency
f_s	[Hz]	Sampling frequency
g	[$m\ s^{-2}$]	Acceleration of gravity
k	[m^{-1}]	Wavenumber
$k\zeta_a$	[-]	Wave steepness
l	[m]	Free path length
l_m	[m]	Mean free path length
l_z	[m]	Distance with respect to the depth level z
m_0	[-]	0^{th} spectral moment
m_1	[s^{-1}]	1^{st} spectral moment
n	[-]	Number of data points (Eq. 18)
n	[-]	Real part of the refractive index
p	[-]	Auxiliary variable
r	[-]	Correlation coefficient
t	[s]	Time
v_w	[$m\ s^{-1}$]	Wind speed
x	[m]	Horizontal distance
y	[m]	Horizontal distance
z	[m]	Water depth
z_t	[m]	True water depth (length of water column)
Chl	[$mg\ m^{-3}$]	Chlorophyll content
CV	[%]	Coefficient of Variations
D	[-]	Cumulative scattering distribution
E	[$W\ m^{-2}$]	Irradiance
E_d	[$W\ m^{-2}$]	Downwelling irradiance
E_u	[$W\ m^{-2}$]	Upwelling irradiance
E_{MC}	[$W\ m^{-2}$]	Mean downwelling irradiance per depth (Monte Carlo)
E_{HL}	[$W\ m^{-2}$]	Mean downwelling irradiance per depth (*Hydrolight*)

G	[-]	Gray value
H	[m]	Wave height
H_s	[m]	Significant wave height
H/L	[-]	Wave steepness
I	[%]	Intensity or photon weight
I_0	[%]	Initial weight or intensity at the surface
K_d	[m^{-1}]	Diffuse attenuation coefficient
L	[m]	Wavelength
L_m	[m]	Mean fluctuation length
N	[m^{-1}]	Normalized number of flashes that exceed a threshold
N_{max}	[-]	Maximum number of scattering events
PDF	[m^{-1}]	Probability density distribution
R	[-]	Random number
$RMSE$	[%]	Root mean square error
S_G	[s]	Frequency spectrum of the gray value
S_χ	[m]	Spectral density of the normalized downwelling irradiance
T	[°C]	Temperature
T	[s]	Period
T_m	[s]	Mean fluctuation period
T_p	[s]	Peak period
T_0	[s]	Zero-upcrossing period
α	[°]	Wave slope
β	[-]	Scattering phase function
β_p	[-]	Adapted particulate scattering phase function
β_w	[-]	Scattering phase function of pure seawater
γ_1	[-]	Skewness
γ_2	[-]	Kurtosis
ε	[%]	Percent relative difference at a predefined depth
ζ	[m]	Surface wave elevation
ζ_a	[m]	Wave amplitude
θ	[°]	Sun zenith angle
λ	[nm]	Electromagnetic wavelength
μ	[-]	Mean value
μ_m	[-]	Median value
σ	[-]	Standard deviation
σ_m	[-]	Standard deviation with respect to the median
τ	[-]	Optical depth
χ	[-]	Normalized downwelling irradiance
χ_{max}	[-]	Maximum normalized downwelling irradiance
χ_{th}	[-]	Threshold normalized downwelling irradiance
ψ	[°]	Scattering angle
ω_0	[-]	Single scattering albedo

Bibliography

(1) **Cox**, C., and W. **Munk** (1954), Measurements of the roughness of the sea surface from photographs of the sun's glitter, *J. Opt. Society Am.*, 44 (11), 838-850.

(2) **Cox**, C., and W. **Munk** (1956), Slopes of the sea surface deduced from photographs of the sun glitter, Bulletin of the Scripps Inst. Oceanogr., Univ. of California Press, 6 (9), Berkley and Los Angeles, 401-487.

(3) **D'Alimonte**, D., G. **Zibordi**, T. **Kajiyama**, and J. C. **Cunha** (2010), Monte Carlo code for high spatial resolution ocean color estimation, *Appl. Opt.*, 49 (26), 4936-4950, doi: 10.1364/ AO.49.004936.

(4) **Davidson**, A. T. (1998), The impact of UVB radiation on marine plankton, *Mutat. Res.*, 422 (1), 119-129, Elsevier.

(5) **Deckert**, R., and K. J. **Michael** (2006), Lensing effect on underwater levels of UV radiation, *J. Geophys. Res.*, 111, C05014, doi: 10.1029/2005JC003332.

(6) **Dekshenieks**, M. M., P. L. **Donaghay**, J. M. **Sullivan**, J. E. B. **Rines**, T. R. **Osborn**, and M. S. **Twardowski** (2001), Temporal and spatial occurrence of thin phytoplankton layers in relation to physical processes, *Mar. Ecol. Prog. Ser.*, 223, 61-71, ISSN 0171-9630.

(7) **Dera**, J. (1992), *Marine Physics*, Elsevier Oceanogr. Ser., 53, ISBN 0-444-98716-9.

(8) **Dera**, J., and D. **Stramski** (1986), Maximum effects of sunlight focusing under a wind-disturbed sea surface, *Oceanologia*, 23, 15-42.

(9) **Dickey**, T. D., M. **Lewis**, and G. **Chang** (2006), Optical oceanography: Recent advances and future directions using global remote sensing and in situ observations, *Rev. Geophys.*, 44, RG1001, doi: 10.1029/2003RG000148.

(10) **Dickey**, T. D., G. W. **Kattawar**, and K. J. **Voss** (2011), Shedding new light on light in the ocean, *Physics Today*, 64 (4), 44-49, doi: 10.1063/1.3580492.

(11) **Eldevik**, T, and K. B. **Dysthe** (2002), Spiral Eddies, *J. Phys. Oceanogr.*, 32, 851-869, doi: 10.1175/1520-0485(2002)032.

(12) **Elfouhaily**, T., B. **Chapron**, K. **Katsaros**, and D. **Vandemark** (1997), A unified directional spectrum for long and short wind-driven waves, *J. Geophys. Res.*, 102, C7, 15781-15796, doi: 10.1029/97JC00467.

(13) **El Naggar**, S., and A. **Macke** (Ed.) (2010), The expedition of the Research Vessel "Polarstern" to the Antarctic in 2009 (*ANT-XXVI/1*), *Reports on Polar and Marine Research*, 614, 79p, hdl: 10013/epic.35280.

(14) **Fedorov**, K. N., and A. I. **Ginsburg** (1992), The near-surface layer of the ocean, *VSP BV*, Utrecht, ISBN 90-6764-136-7.

(15) **Fell**, F, and J. **Fischer** (2001), Numerical simulation of the light field in the atmosphere-ocean system using the matrix-operator method, *J. Quantitative Spectroscopy & Radiative Transfer*, 69, 351-388, doi: 10.1016/S0022-4073(00) 00089-3.

(16) **Forristall**, G. Z. (2000), Wave crest distributions: Observations and second-order theory, *J. Phys. Oceanogr.*, 30 (8), 1931-1943, doi: 10.1175/1520-0485 (2000)030.

(17) **Fraser**, A. B., **Walker** R. E, and F. C. **Jurgens** (1980), Spatial and temporal correlation of underwater sunlight fluctuations in the Sea, *IEEE J. Oceanic Engineering*, OE 5 (3), 195-198, doi: 10.1109/JOE.1980.1145467.

(18) **Gernez**, P., and D. **Antoine** (2009), Field characterization of wave-induced underwater light field fluctuations, *J. Geophys. Res.*, 114, C06025, doi: 10.1029/ 2008JC005059.

(19) **Gernez**, P., D. **Stramski**, and M. **Darecki** (2010), Vertical changes in the probability distribution of downwelling irradiance within the near-surface ocean layer under clear sky conditions, *Talk at the XX Ocean Optics Conference*, Anchorage, Alaska (09/27/2010).

(20) **Gernez**, P., D. **Stramski**, and M. **Darecki** (2011), Vertical changes in the probability distribution of downwelling irradiance within the near-surface ocean under clear sky conditions, submitted to J. Geophys. Res., manuscript of 03/31/2011.

(21) **Gordon**, H. R. (1985), Ship perturbation of irradiance measurements at sea. 1: Monte Carlo simulations, *Appl. Opt.*, 24 (23), 4172-4182, doi: 10.1364/AO. 24.004172.

(22) **Gordon**, H. R., and O. B. **Brown** (1973), Irradiance reflectivity of a flat ocean as a function of its optical properties, *Appl. Opt.*, 12 (7), 1549-1551, doi: 10.1364/ AO.12.001549.

(23) **Gordon**, H. R. (1994), Modeling and simulating radiative transfer in the ocean, in: R. W. Spinrad, K. L. Carder, and M. J. Perry: Ocean optics, *Oxford Monographs on Geology and Geophysics*, 25, 1-39, ISBN 0-19-506843-2.

(24) **Greene**, R. M., and V. A. **Gerard** (1990), Effects of high-frequency light fluctuations on growth and photoacclimation of the red alga *Chondrus crispus*, Marine Biology 105, 337-344, doi: 10.1007/BF01344304.

(25) **Hanlon**, R. T., and J. B. **Messenger** (1996), *Cephalopod behaviour*, Cambridge University Press, ISBN 0-521-42083-0.

(26) **Hasselmann**, K., T. P. **Barnett**, E. **Bouws**, H. **Carlson**, D. E. **Cartwright**, K. **Enke**, J. A. **Ewing**, H. **Gienapp**, D. E. **Hasselmann**, P. **Kruseman**, A. **Meerburg**, P. **Müller**, D. J. **Olbers**, K. **Richter**, W. **Sell**, and H. **Walden** (1973), Measurements of wind-wave growth and swell decay during the Joint North Sea Wave Project (JONSWAP), *Dtsch. Hydrogr. Zeit.*, 12, 95 pp.

(27) **Heron**, M. L., W. J. **Skirving**, and K. J. **Michael** (2006), Short-wave ocean wave slope model for use in remote sensing data analysis, IEEE Transaction Geosci. Remote Sense., 44 (7), 1962-1973, doi: 10.1109/TGRS.2006.870493.

(28) **Hieronymi**, M. (2008), Hydroelastische Analyse vertikal schwingender Offshore-Tauchsysteme für die Tiefsee, *Jahrbuch der STG*, 101, Springer, Berlin, 237-247.

(29) **Hieronymi**, M., and A. **Macke** (2010), Spatiotemporal underwater light field fluctuations in the open ocean, *J. Europ. Opt. Soc. Rap. Public.*, 5, 10019S, 1-8, doi: 10.2971/JEOS. 2010.10019S.

(30) **Hogben**, N., and F. E. **Lumb** (1967), *Ocean wave statistics*, HMSO, London.

(31) **Jerlov**, N. G. (1968), *Optical Oceanography*, Elsevier Oceanography Series, 5, Amsterdam.

(32) **Jerlov**, N. G., and E. **Steemann Nielsen** (1974), *Optical aspects of oceanography*, Academic Press, London, ISBN 0-12-384950-0.

(33) **Johnsen**, S. and H. **Sosik** (2004), Shedding light on light in the ocean, *Oceanus Magazine*, 43 (2), 1-5, WHOI.

(34) **Kattner**, G., and B. **Koch** (Ed.) (2009), The expedition of the Research Vessel "Polarstern" to the Antarctic in 2008 (*ANT-XXV/1*), *Reports on Polar and Marine Research*, 594, 72p, hdl: 10013/epic.32943.

(35) **Kinsman**, B. (1965), *Wind Waves: their generation and propagation on the ocean surface*, Englewood Cliffs, N.J., Prentice-Hall.

(36) **Kirk**, J. T. O. (1981), Monte Carlo study of the nature of the underwater light field in, and the relationship between optical properties of, turbid yellow water, *Aust. J. Mar. Freshwater Res.*, 32, 517-532, doi: 10.1071/MF9810517.

(37) **Krauss**, J., and H. **Meldau** (1983), *Wetter- und Meereskunde für Seefahrer*, first published 1931, 7th edition by W. Stein, and R. Höhn, Springer, Berlin, ISBN 3-540-11763-6.

(38) **Long**, S. P., S. **Humphries**, and P. G. **Falkowski** (1994), Photoinhibition of photosynthesis in nature, *Annu. Rev. Plant Physiol. Plant Mol. Biol.*, 45, 633-662, doi: 10.1146/annurev.pp.45.060194.003221.

(39) **Longhurst**, A., S. **Sathyendranath**, T. **Platt**, and C. **Caverhill** (1995), An estimate of global primary production in the ocean from satellite radiometer data, *J. Plankton Res.*, 17 (6), 1245-1271, doi: 10.1093/PLANKT/17.6.1245.

(40) **Longuet-Higgins**, M. S. (1963), The effect of non-linearities on statistical distributions in the theory of sea waves, *J. Fluid Mechanics*, 17, 459-480, doi: 10.1017/S0022112 063001452.

(41) **Longuet-Higgins**, M. S. (1982), On the skewness of sea-surface slopes, *J. Phys. Oceanogr.*, 12, 1283-1291, doi: 10.1175/1520-0485(1982)012.

(42) **Macke**, A. (2000), Monte Carlo calculations of light scattering by large particles with multiple internal inclusions, Light scattering by nonspherical particles: Theory, measurements, and applications, San Diego: *Academic Press*, 309-322.

(43) **Macke**, A. (Ed.) (2009), The expedition of the Research Vessel "Polarstern" to the Antarctic in 2008 (*ANT-XXIV/4*), *Reports on Polar and Marine Research*, 591, 64p, hdl: 10013/epic.32648.

(44) **Marcos**, M., J. R. **Seymour**, M. **Luhar**, W. M. **Durham**, J. G. **Mitchell**, A. **Macke**, and R. **Stocker** (2011), Microbial alignment in flow changes ocean light climate, *PNAS*, doi: 10.1073/PNAS.1014576108.

(45) **Mobley**, C. D., B. **Gentili**, H. R. **Gordon**, Z. **Jin**, G. W. **Kattawar**, A. **Morel**, P. **Reinersman**, K. **Stamnes**, and R. H. **Stavn** (1993), Comparison of numerical models for computing underwater light fields, *Appl. Opt.*, 32 (36), 7484-7504, doi: 10.1364/AO.32.007484.

(46) **Mobley**, C. D. (1994), *Light and water: Radiative transfer in natural waters*, San Diego: Academic Press, 592 pp.

(47) **Morel**, A. (2009), Are the empirical relationships describing the bio-optical properties of case 1 waters consistent and internally compatible?, *J. Geophys. Res.*, 114, C01016, doi: 10.1029/2008JC004803.

(48) **Morel**, A., D. **Antoine**, and B. **Gentili** (2002), Bidirectional reflectance of oceanic waters: accounting for Raman emission and varying particle scattering phase function, *Appl. Opt.*, 41 (30), 6289-6306, doi: 10.1364/AO.41.006289.

(49) **Morel**, A., and B. **Gentili** (1991), Diffuse reflectance of oceanic waters: its dependence on Sun angle as influenced by the molecular scattering contribution, *Appl. Opt.*, 30 (30), 4427-4438, doi: 10.1364/AO.30.004427.

(50) **Morel**, A., B. **Gentili**, H., M. **Chami**, and J. **Ras** (2006), Bio-optical properties of high chlorophyll Case 1 waters and of yellow-substance-dominated Case 2 waters, Deep-Sea Res. I, 53, 1439-1459, doi: 10.1016/J.DSR.2006.07.007.

(51) **Morel**, A., B. **Gentili**, H. **Claustre**, M. **Babin**, A. **Bricaud**, J. **Ras**, and F. **Tieche** (2007), Optical properties of the "clearest" natural waters, *Limnol. Oceanogr.*, 52 (1), 217-229, doi: 10.4319/LO.2007.52.1.0217.

(52) **Morel**, A., and L. **Prieur** (1977), Analysis of variations in ocean color, *Limnol. Oceanogr.*, 22 (4), 709-722.

(53) **Nikolayev**, V. P., and M. S. **Khulapov** (1976), Use of a nonstatistical model to explain the mechanism of underwater illumination fluctuations, *Izv. Atmospheric and Oceanic Physics*, 12 (9), 993-997.

(54) **Nikolayev**, V. P., O. I. **Prokopov**, G. V. **Rozenberg**, and V. I. **Shevernev** (1972), Statistical properties of the underwater illumination, *Izv. Atmospheric and Oceanic Physics*, 8 (9), 936-944.

(55) **Ochi**, M. K., and E. N. **Hubble** (1976), Six-parameter wave spectra, *Proc. 15th Coastal Engineering Conf.*, 301-328.

(56) **Ohlmann**, J. C., D. A. **Siegel**, and C. **Gautier** (1996), Ocean mixed layer radiant heating and solar penetration: A global analysis, *J. Climate*, 9 (10), 2265-2280, doi: 10.1175/ 1520-0442(1996)009.

(57) **Pan**, X, and R. C. **Zimmerman** (2010), Modeling the vertical distribution of downwelling plane irradiance and diffuse attenuation coefficient in optically deep water, *J. Geophys. Res.*, 115, C08016, doi: 10.1029/2009JC006039.

(58) **Petzold**, T. J. (1972), Volume scattering functions for selected ocean waters, Scripps Institution of Oceanography, San Diego, Ref. 72-78.

(59) **Plass**, G. N., and G. W. **Kattawar** (1972), Monte Carlo calculations of radiative transfer in the Earth's atmosphere-ocean system: 1. Flux in the atmosphere and ocean, *J. Phys. Oceanogr*., 2, 139-145, doi: 10.1175/1520-0485(1972)002.

(60) **Plass**, G. N., G. W. **Kattawar**, and J. A. **Guinn** Jr. (1975), Radiative transfer in the earth's atmosphere and ocean: influence of ocean waves, *Appl. Opt.*, 14 (8), 1924-1936, doi: 10.1364/AO.14.001924.

(61) **Preisendorfer**, R. W. (1976), *Hydrologic Optics*, US Dept. Com., Nat. Oceanic and Atmospheric Administration.

(62) **Preisendorfer**, R. W., and C. D. **Mobley** (1985), Unpolarized irradiance reflectance and glitter patterns of random capillary waves on lakes and seas, by Monte Carlo simulations, NOAA Tech. Memo. ERL PMEL, 36, Pacific Mar. Environ. Lab., Seattle, WA, 141 pp.

(63) **Preisendorfer**, R. W., and C. D. **Mobley** (1986), Albedos and glitter patterns of a wind-roughened sea surface, *J. Phys. Oceanogr.*, 16 (7), 1293-1316, doi: 10.1175/1520-0485 (1986)016.

(64) **Rodriguez**, G. R., and C. **Guedes Soares** (2001), Correlation between successive wave heights and periods in mixed sea states, *Ocean Engineering*, 28, 1009-1030, doi: 10.1016/S0029- 8018(00)00038-X.

(65) **Schenck**, H. (1957), On the focusing of sunlight by ocean waves, *J. Opt. Soc. Am.*, 47 (7), 653-657, doi: 10.1364/JOAS.47.000653.

(66) **Segelstein**, D. J. (1981), The complex refractive index of water, MS Thesis, *University of Missouri*, Kansas City.

(67) **Shifrin**, K. S. (1983), *Physical optics of ocean water*, AIP Translation Ser., ISBN 0-88318-529-6.

(68) **Siegel**, D. A., A. F. **Michaels**, J. C. **Sorensen**, M. C. **O'Brien**, and M. A. **Hammer** (1995), Seasonal variability of light availability and utilization in the Sargasso Sea, *J. Geophys. Res.*, 100, 8695-8713, doi: 10.1029/95JC00447.

(69) **Signorini**, S. R., and C. R. **McClain** (2009), Environmental factors controlling the Barents Sea spring-summer phytoplankton blooms, *Geophys. Res. Let.*, 36, L10604, doi: 10.1029 /2009GL037695.

(70) **Smith**, R. C. (1974), Structure of solar radiation in the upper layers of the sea, *Optical Aspects of Oceanography*, Ed. N. G. Jerlov and E. Steemann Nielsen, 95-119.

(71) **Snyder**, R. L., and J. **Dera** (1970), Wave-induced light field fluctuations in the Sea, *J. Opt. Soc. Am.*, 60 (8), 1072-1079, doi: 10.1364/JOSA.60.001072.

(72) **SORCE** (2002), *Brochure of the Solar Radiation and Climate Experiment*, NP-2002-9-482-GSFC, http://lasp.colorado.edu/sorce (06/10/2008).

(73) **Stavn**, R. H. (1993), Effects of Raman scattering across the visible spectrum in clear ocean water: a Monte Carlo study, *Appl. Opt.*, 32 (33), 6853-6863, doi: 10.1364/ AO.32.006853.

(74) **Sterl**, A., and S. **Caires** (2005), Climatology, variability and extrema of ocean waves: The web-based NKMI/ERA-40 wave atlas, *Int. J. Climatol.*, 25, 963-977, doi: 10.1002/ JOC.1175.

(75) **Stewart**, R. R. (2005), *Oceanography in the 21th century – An online textbook*, Department of Oceanography, Texas A&M Univ., web page (03/02/2011): http://oceanworld.tamu.edu/resources/oceanography-book/phytoplankton-distribution.htm

(76) **Stramska**, M., and T. D. **Dickey** (1998), Short-term variability of the underwater light field in the oligotrophic ocean in response to surface waves and clouds, *Deep-Sea Res. I*, 45, 1393-1410, doi: 10.1016/S0967-0637(98)00020-X.

(77) **Stramski**, D. (1986), The effect of daylight diffuseness on the focusing of sunlight by sea surface waves, *Oceanologia*, 24, 11-27.

(78) **Stramski**, D., and J. **Dera** (1988), On the mechanism for producing flashing light under a wind-disturbed water surface, *Oceanologia*, 25, 5-21.

(79) **Stramski**, D., and J. **Tegowski** (2001) Effects of intermittent entrainment of air bubbles by breaking wind waves on ocean reflectance and underwater light field, *J. Geophys. Res.*, 106 (C12), 31345-31360, doi: 10.1029/2000JC000461.

(80) **Trenberth**, K. E., J. T. **Fasullo**, and J. **Kiehl** (2009), Earth's global energy budget, *Bull. Am. Meteorol. Soc.*, 90 (3), 311-323, doi: 10.1175/2008BAMS2634.1.

(81) **Wahl**, M. (2009), *Marine hard bottom communities – Patterns, dynamics, diversity and change*, Springer Series: Ecolog. Ser., 206, 420 pp, ISBN 978-3-540-92703-7.

(82) **Weber**, V. L. (2010), Coefficient of variation of underwater irradiance fluctuations, *Radiophysics and Quantum Electronics*, 53 (1), 13-27.

(83) **Wernand**, M. R., and H. J. **van der Woerd** (2010), Ocean color changes in the North Pacific since 1930, *J. Europ. Opt. Soc. Rap. Public.*, 5, 10015s, doi: 10.2971 /JEOS.2010. 10015S.

(84) **Wozniak**, B., J. **Dera**, D. **Ficek**, R. **Majchrowski**, M. **Ostrowska**, and S. **Kaczmarek** (2003), Modelling light and photosynthesis in the marine environment, *Oceanologia*, 45 (2), 171-245.

(85) **You**, Y., D. **Stramski**, M. **Darecki**, and G. W. **Kattawar** (2010), Modeling of wave-induced irradiance fluctuations at the near-surface depths in the ocean: a comparison with measurements, *Appl. Opt.*, 49 (6), 1041-1053, doi: 10.1364/AO. 49.001041.

(86) **Zafiriou**, O. C., J. **Joussot-Dubien**, R. G. **Zepp**, and R. G. **Zika** (1984), Photochemistry of natural waters, *Environ. Sci. Technol.*, 18 (12), 358A-371A.

(87) **Zaneveld**, J. R. V., E. **Boss**, and A. **Barnard** (2001), Influence of surface waves on measured and modeled irradiance profiles, *Appl. Opt.*, 40 (9), 1442-1449, doi: 10.1364/AO.40. 001442.

(88) **Zenk**, W., and S. **El Naggar** (Ed.) (2010), The expedition of the Research Vessel "Polarstern" to the Antarctic in 2009 (*ANT-XXV/5*), *Reports on Polar and Marine Research*, 603, 62p, hdl: 10013/epic.34023.d001.

(89) **Zhang**, X., M. **Lewis**, M. **Lee**, B. **Johnson**, and G. **Korotaev** (2002), The volume scattering function of natural bubble populations, *Limnol. Oceanog.*, 47 (5), 1273-1282.

Danksagung

Vielen Dank an alle, die mich in meiner wissenschaftlichen Arbeit und bei meinen Messkampagnen auf See unterstützt haben. Mein größter Dank gilt dabei insbesondere meinem Doktorvater Andreas Macke. Auch bei Oliver Zielinski, Martin Wahl und Martin Frank, sowie bei meiner Familie Ullrich Hieronymi, Stefanie Hieronymi und Janine Hieronymi möchte ich mich ausdrücklich bedanken.

Erklärung

Hiermit bestätige ich, dass ich die vorliegende Dissertation selbstständig verfasst und keine anderen als die angegebenen Quellen und Hilfsmittel verwendet habe. Ich versichere, dass diese Arbeit noch nicht zur Erlangung eines Doktorgrades an anderer Stelle vorgelegen hat. Ich erkläre, dass die vorliegende Arbeit gemäß der Grundsätze zur Sicherung guter wissenschaftlicher Praxis der Deutschen Forschungsgemeinschaft erstellt wurde.

Kiel, März 2011 Martin Hieronymi